


November 2017

Aliovalent Dopants in ZnO Nanocrystals: Synthesis to Electronic Structure

Dongming Zhou

Follow this and additional works at: https://scholarworks.umass.edu/dissertations_2

 Part of the [Inorganic Chemistry Commons](#), [Materials Chemistry Commons](#), and the [Nanoscience and Nanotechnology Commons](#)

Recommended Citation

Zhou, Dongming, "Aliovalent Dopants in ZnO Nanocrystals: Synthesis to Electronic Structure" (2017). *Doctoral Dissertations*. 1144.
https://scholarworks.umass.edu/dissertations_2/1144

This Open Access Dissertation is brought to you for free and open access by the Dissertations and Theses at ScholarWorks@UMass Amherst. It has been accepted for inclusion in Doctoral Dissertations by an authorized administrator of ScholarWorks@UMass Amherst. For more information, please contact scholarworks@library.umass.edu.

**ALIOVALENT DOPANTS IN ZNO NANOCRYSTALS: SYNTHESIS TO
ELECTRONIC STRUCTURE**

A Dissertation Presented

by
DONGMING ZHOU

Submitted to the Graduate School of the
University of Massachusetts Amherst in partial fulfillment
of the requirements for the degree of

DOCTOR OF PHILOSOPHY

September 2017

Chemistry

© Copyright by Dongming Zhou 2017

All Rights Reserved

**ALIOVALENT DOPANTS IN ZNO NANOCRYSTALS: SYNTHESIS TO
ELECTRONIC STRUCTURE**

A Dissertation Presented

by

DONGMING ZHOU

Approved as to style and content by:

Kevin R. Kittilstved, Chair

Michael D. Barnes, Member

Bret Jackson, Member

Anthony D. Dinsmore, Member

Richard W. Vachet, Department Head
Department of Chemistry

ACKNOWLEDGMENTS

My journey through graduate school has been truly rewarding. I would first like to thank Kevin for always being supportive and giving me the freedom to explore different projects, for sharing his knowledge, experience, and scientific passion. I would also like to thank Kevin for bringing us home every semester. The way he treats family and his sacrifice for his family is a very good lesson to me.

Besides, I would like to thank my thesis committee members, Professor Mike Barnes, Professor Bret Jackson and Professor Anthony Dinsmore for their insightful suggestions and continuous support.

The research group in Kevin's lab is a very lovely group. Through setting up the new lab, conducting MCD experiments overnight, or even sharing and helping each other for the prospectus, original research proposal, we have built a tight bounding. I would like to especially thank former group members: Kim-Ngan Hua, Swamy Pittala, Keith Lehuta, for the long-time help. I would also appreciate current group members William Harrigan and Fumitoshi Kato, who continue making this lab full of laugh and happiness.

I also had several excellent collaborators and I enjoyed the wonderful experience working with Professor Thai group, Professor DV group and Professor Russell group and Professor Barnes group. This including Longyu Li, Sashi Debnath, Yao Liu, and Peijian Wang. Each of you is an expert in your field and I was motived and enjoyed during the collaborations. Thanks to Professor Elizabeth Young in Amherst College for your always patient explaining electrochemistry and ultrafast spectroscopy.

Finally, I want to give thanks to the NSF funding (CHE-1454930) support and Dr Dr. Marram for giving me the Ragle Fellowship during my last summer at Umass.

Besides research, my graduate journey was fulfilled because of a group of people sharing the same interest, ballroom dancing. Thanks to Yanqin Xu who brought me into this exciting area during my second year. Our members also including Tao Sun, Jing Liu, Shengkai Li. I would not forget back in the days we spent lots of time after work training and discussion the techniques for the dancing. Another group, Umass ballroom dance team, is also a very united team. Thank everyone on the team, and especially thanks to our coach Evgueni and Sara, a world-class professional dance couple. You two really make my day every time watching and training with you.

Dancing also brings me the chance to meet my girlfriend, Jiayue Ni. Without your love, support and sacrifice for the last three years, I could not imagine how life is going to be.

Lastly, I would like to thank my parents. Words cannot explain how much I love you two and how much you love and support me. I am so glad to be your son.

ABSTRACT

ALIOVALENT DOPANTS IN ZNO NANOCRYSTALS: SYNTHESIS TO ELECTRONIC STRUCTURE

September 2017

DONGMING ZHOU, B.A., ZHEJIANG UNIVERSITY

Ph.D., UNIVERSITY OF MASSACHUSETTS AMHERST

Directed by: Professor Kevin. R. Kittilstved

Semiconductor nanocrystal doping has stimulated broad interest for many applications including solar energy conversion, nanospintronics, and phosphors or optical labels. The study of the chemistry and physics of doped colloidal semiconductor nanocrystals has been dominated in the literature by isovalent dopants such as Mn^{2+} and Co^{2+} ions in II-VI semiconductors, in which the dopant oxidation state is the same as the cation ions. Until recently, aliovalent dopants has received much attention due to the plasmonic properties. Aliovalent is when the oxidation states of the dopant in the lattice differs from the cation ions. In the plasmonic semiconductor nanocrystals, the dopants are noted as shallow donor and can donate electrons to the conduction band, resulting in the collectively resonate of the delocalized electrons under certain electromagnetic radiation, i.e. localized surface plasmon resonances (LSPR). However, only small amount of the dopants can donate delocalized electrons. The amount of ‘activated’ dopant is restricted by the synthetic methods and the defect chemistry related to the plasmonic property is still under debate. In this report, we are using Al^{3+} doped ZnO nanocrystals as an example. We have established a synthesis method to bring more dopant incorporation and less charge compensation defect, so higher electronically activated dopant is achieved. These results

provide a synthetic strategy as well as the electronic structure understanding for the aliovalent dopants in semiconductor nanocrystals.

On the other hand, less attention has been focused on the deep donor dopant such as Fe^{3+} in II-VI semiconductors. Deep donor, due to the oxidation redox potential lower than the conduction band potential (deep), instead of donating electrons in conduction bands, will donate electrons in trap states or defect states. For deep donor, less is known for the driving force to determine the oxidation state of the n-type dopant. Here, we have developed a dopant-specific spectroscopy for estimation the deep donor Fe^{3+} speciation, i.e. substitutional, interstitial, or surface Fe^{3+} in ZnO nanocrystals and conducted photo-charging experiment to study the redox potential of the deep donor dopant. These studies could help to identify the dopant speciation and understand the interactions between the conduction band electrons and the deep dopants.

TABLE OF CONTENTS

	Page
ACKNOWLEDGMENTS	iv
ABSTRACT	vi
LIST OF TABLES	x
LIST OF FIGURES	xi
CHAPTER	
1. INTRODUCTION	1
1.1. Deep Donor in Dilute Magnetic Semiconductor.....	9
1.2. Shallow Donor in Plasmonic Doped Metal Oxide Nanocrystals.....	13
2. CONTROL OVER FE ³⁺ SPECIATION IN COLLOIDAL ZNO NANOCRYSTALS.....	23
2.1. Introduction.....	23
2.2. Experimental Section.....	25
2.3. Result and Discussion.....	28
2.4. Conclusions.....	40
3. ELECTRON TRAPPING ON FE ³⁺ SITE IN PHOTODOPED ZNO COLLOIDAL NANOCRYSTALS.....	45
3.1. Introduction.....	45
3.2. Experimental Section.....	47
3.3. Result and Discussion.....	48
3.4. Conclusions.....	59
4. ETCHING AND REGROWTH STRATEGY FOR AL DOPED ZNO NANOCRYSTALS LEADING TO LESS DEFECT AND HIGHER ACTIVATION	62
4.1. Introduction.....	62
4.2. Experimental Section.....	62
4.2. Result and discussion.....	64

5. CONCLUSION AND OUTLOOK.....	82
BIBLIOGRAPHY.....	87

LIST OF TABLES

Table	Page
4-1. The detailed parameters from Rietveld analysis fitting for Al doped ZnO nanocrystals.....	75

LIST OF FIGURES

Figure	Page
1.1. Band diagram for doping in bulk semiconductor.	1
1.2. Band structure for quantum dot	4
1.3. Illustration of estimation of dopant redox potential within the ZnO	11
1.4. Localized surface plasmon resonance frequency dependence on free carrier density and doping constraints.	15
1.5. Schematic representation of the common n-type doping mechanisms in the metal oxide.....	17
2.1. Electronic absorption spectra of ZnO and 0.78% Fe-doped ZnO	28
2.2. Powder X-ray diffraction patterns of 0.15% and 2.0% Fe:ZnO..	29
2.3. Room temperature X-band EPR spectra of colloidal Fe:ZnO QDs.....	30
2.4. Comparison between the experimental EPR spectrum of 0.15% Fe:ZnO.....	31
2.5. Effect of varying the magnitude of <i>E</i> -strain on the simulated EPR spectrum	32
2.6. Room-temperature X-band EPR spectra.....	34
2.7. Histograms from TEM particle analysis as a function of Fe ³⁺ :ZnO growth times	36
2.8. Absorption spectra of 0.5% Fe:ZnO before and after TMAOH addition.	38
2.9. Schematic representation for the proposed mechanism of Fe ³⁺ incorporation into colloidal ZnO nanocrystals during nanocrystal growth.	39
2.10. Zero-field-cooled and field-cooled magnetic susceptibility.	40
3.1. Evolution of the EPR and UV-Vis and FTIR spectra..	49
3.2. Electronic absorption spectra of the band gap transition.	51
3.3. Summary of spectroscopic changes EPR intensities and LSPR intensity	52
3.4. Room temperature electronic absorption spectra.....	53

3.5. Room temperature Mössbauer spectra of 5% Fe-doped ZnO QD.....	55
3.6. Absorption spectra of the LMCT transition.....	55
3.7. Schematic orbital/band diagram for medium and large (no quantum- confinement) Fe-doped ZnO QDs.	57
4.1. Illustration of the molecular mechanism for etching and regrowth.	65
4.2. Evolution of the FTIR and absorption spectra for Al doped ZnO colloidal	66
4.3. TEM image of Al doped ZnO nanocrystals.	68
4.4. Band gap absorption and plasmonic resonance for 1.3% Al doped ZnO nanocrystals	70
4.5. The band gap absorption for Al doped ZnO with different amount of OA been added during the synthesis.	71
4.6. Band gap absorption and plasmonic resonance for three different synthetic method.	72
4.7. XRD patterns of pure ZnO and Al doped ZnO nanocrystals.	74
4.8. Rietveld analysis using Maud.	75
4.9. TEM for Al doped ZnO nanocrystals with 2 mmol of OA during the nucleation.....	77
4.10. Band gap absorption, plasmonic resonance, and picture for Al doped and In doped ZnO nanocrystals.	79
5.1. Band diagram for the different Sn ⁴⁺ concentration in Sn ⁴⁺ doped In ₂ O ₃	83
5.2. Schematic diagram for the aliovalent doping in semiconductor NCs.....	84

CHAPTER 1

INTRODUCTION

Doping in bulk semiconductor has a long history and was first patented since the 1950s. The purpose of doping in bulk semiconductor by introducing impurities is to modulate its electrical properties, and in most cases, increase the carrier concentration and conductivity. The undoped material is called intrinsic semiconductor and the doped material is called extrinsic semiconductor. The concentration of both electron and hole can be tuned by either n-type dopant (Donor) and p-type dopant (Acceptor). Using well-known silicon as an example. The oxidation state of silicon is +4 when doped with a group V impurity (e.g. Antimony, Phosphorous, Arsenic etc.), an extra electron is donated to the semiconductor, known as n-type doping. When doped with a group III impurity (e.g. Boron, Gallium, Indium etc.), an extra hole is donated, or an electron is accepted, known as p-type doping.

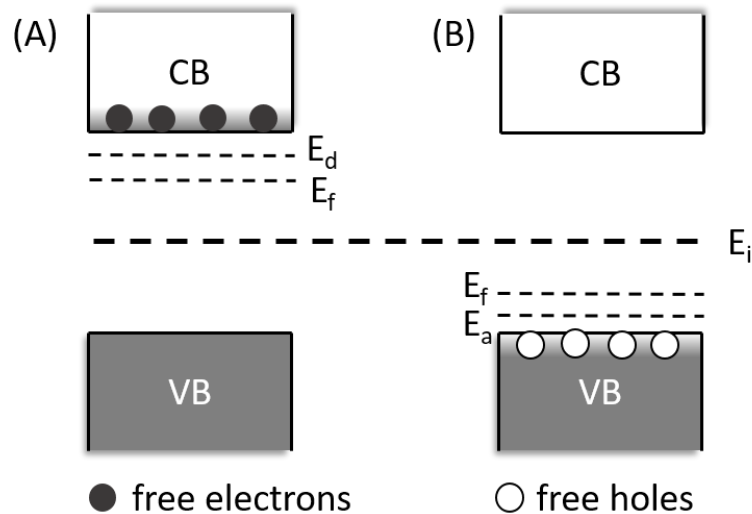


Figure 1.1. Band diagram for doping in bulk semiconductor.

The extra carrier donated by the dopant is loosely bounded to the impurity atom. While the doping also introduces energy states within the band gap. Electron donor impurities create states near the conduction band while electron acceptor impurities create states near the valence band. The energy distance between the donor level (acceptor level) to the conduction band (valence band) is called binding energy, E_d (E_a). The donor energy level (E_d) for Antimony, Phosphorous, Arsenic are 43, 45, and 54 meV respectively. The acceptor energy level (E_a) for Boron, Gallium, Indium are 45, 74, and 157 meV respectively. They are all close to kT at room temperature (25 meV), so the electron or hole will be thermally populated to the conduction band and valence band. Doping also will alter the Fermi level. The Fermi level of the intrinsic semiconductor (E_i) lies approximately halfway in between conduction and valence bands. For n-type semiconductor, Fermi level can be expressed as

$$E_F - E_i \cong kT \ln\left(\frac{n_D}{n_i}\right)$$

(Eq 1.1.1)

And for p-type semiconductor, Fermi level can be expressed as

$$E_i - E_F \cong kT \ln\left(\frac{n_A}{n_i}\right)$$

(Eq 1.1.2)

n_D and n_A are the concentration of donor electrons and acceptor holes, n_i is the intrinsic carrier concentration. This suggests that the Fermi level in the n-type semiconductor is higher than the intrinsic E_i , while the Fermi level for p-type semiconductor is lower than E_i .

When an n-type and p-type semiconductors are connected. The Fermi level must remain constant for both sides in a system in thermodynamic equilibrium, the electrons from the n-type flow into p-type and compensate the holes, or the holes from the p-type flows into n-type compensate the electrons. This creates a depletion region of charge carriers with a built-in potential V_{bi} . Such junction is called p-n junction. Changing the bias connected to junction can tune the current flow. When a forward bias is applied to compensate the built-in potential, current can flow from p site to n site. When a reverse bias is applied, the depletion region increases, thus no current will flow. The tunability of current flow in one direction but not opposite direction makes p-n junction a perfect candidate for diodes. Currently, p-n junction already become elementary ‘building block’ of most semiconductor electronic devices such as diodes, transistors, solar cells, LEDs and integrated circuits. These further constitute the electronic devices of our daily use, such as cellphones, computers.

After doping has been extensively applied to semiconductor industry, scientist and engineer tried to make to the semiconductor smaller and smaller. Until the late 1980s and early 1990s, when the semiconductor is made with only couple nanometers, scientist observed that the band gap of semiconductor increases as the size decrease and the band become dispersed, as seen in Figure 1.2a. This property is called quantum confinement. Imagine an electron confined in a box with length L. The possible energy can be written as

$$E = E_C + \frac{h^2}{8m_e^*} \left(\frac{n_1^2}{L_x^2} + \frac{n_2^2}{L_y^2} + \frac{n_3^2}{L_z^2} \right) \quad n_{1,2,3} = 1, 2, \dots$$

(Eq 1.1.3)

When the size is smaller enough, the second term becomes distinct and dispersed. When the semiconductor is excited with a photon, an electron was excited to the conduction

band left with a hole in the valence band. Before the electron and hole recombine and emit a new photon, the electron is cooled to the bottom of the conduction band and hole is cooled to the top of the valence band, so the emitted photon is the exact band gap energy. As in the case of CdSe, the 2.0 nm CdSe will emit a blue light while 4 nm will emit a red light. Extensive methods on controlling the shape and size distribution of quantum dots have been established¹⁻⁴ and currently, the emission bandwidth can be achieved much smaller than the conventional LED, thus much sharper color can be obtained. This technique has already commercialized in Quantum dot LED TV (QLED)

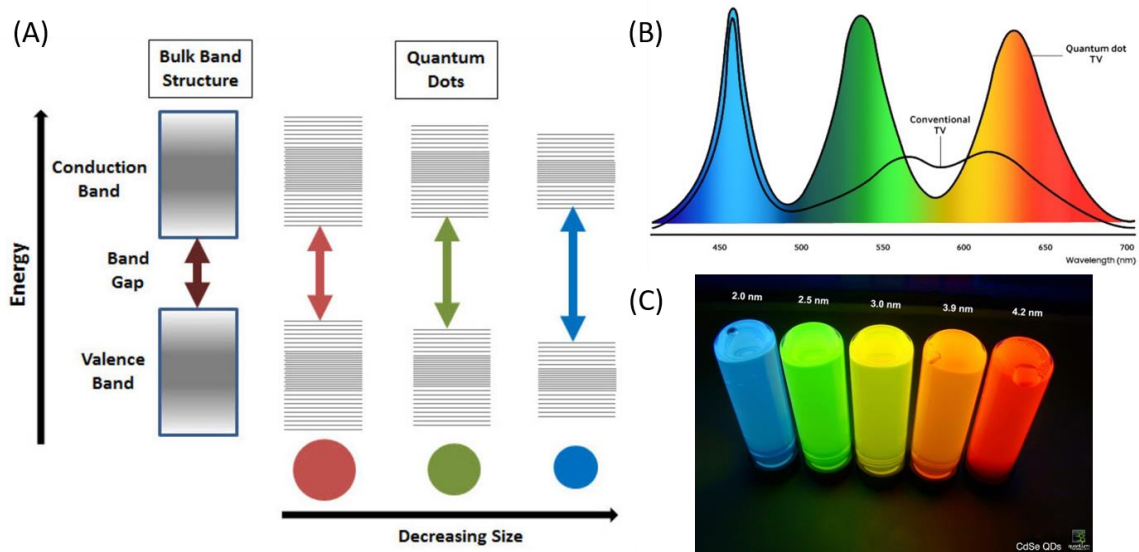


Figure 1.2. (a) Band structure for quantum dot shows the band gap increase and become dispersed as the size decrease. (Adapted from www.sigmaaldrich.com). (b) Bandwidth of photoluminescence for both conventional LED and quantum dot LED. (c) Size-dependent emission for CdSe quantum dots. (Adapted from www.samsung.com).

Doping in semiconductor nanocrystals or quantum dots can also extensively expand the applications of these nanostructures. Unlike the bulk semiconductors in which the dopants increase the carrier concentration for the current flow, doping in semiconductor

nanocrystals introduce new properties as individual nanostructures. Each nanocrystal holds the property from the dopant, and the application can be achieved either in ensemble or superlattice.

Doping into semiconductor nanocrystals has stimulated broad interest in applications including solar energy conversion,⁵⁻⁷ nanospintronics,⁸ and phosphors or optical labels.⁹⁻¹² Most of the applications for doping in semiconductor nanocrystals can be divided into two categories depending on the dopant properties. Some transition metals dopant can be treated as introducing spins into the semiconductor nanocrystal, this is targeting spintronic applications. Such semiconductor is called Dilute Magnetic Semiconductors (DMSs). In the design of spintronic architecture, the dopants act as the quantum bits (qubits). The spin state can be prepared and manipulated both electrically^{13,14} and optically^{15,16} through injection of spin-polarized carriers. The spin state needs to stay long enough before reads out so there are enough correction and manipulation time window. This requires the dopant spin relaxation to be very slow. The factors that affect the spin relaxation time will be discussed in detail later in this Chapter.

The other part of applications utilizes dopant to introducing new electronic states. These electronic states can further act as intermediate states for electron/hole transfer, or energy transfer, targeting solar energy conversion or optical label applications. For example, Mn^{2+} doped CdS quantum dot has been applied in Quantum Dot Sensitized Solar Cells. Mn^{2+} creates electronic states in the mid-gap region of QD and alters the charge separation and recombination dynamics. What's more important is, after the electrons being transferred to Mn^{2+} , the long-lived excited state could be utilized for charge separation and boosts the power conversion efficiency up to 5%.¹⁶ Another example is

lanthanide-doped upconversion nanoparticles.¹⁷⁻²⁰ In upconversion nanoparticles, the absorption and emission spectra of lanthanide dopants Er^{3+} , Tm^{3+} , and Ho^{3+} contribute from the intra-configurational $4f^n$ electron transitions, these dopants work as the activators. To enhance the upconversion efficiency, larger absorption cross-section dopant Yb^{3+} utilized as the sensitizer for absorbing low energy photon. Once two or more sensitizers been excited, the energy transfers to the activator to excite higher energy transition, so the emission can have higher energy. The low energy photon allows the transition into biological tissue, thus the upconversion nanoparticles are most applied in biological labeling, imaging, and therapy.

The study of the chemistry and physics of doped colloidal semiconductor nanocrystals has been dominated in the literature by isovalent dopants such as Mn^{2+} and Co^{2+} ions in II-VI semiconductors, in which the dopant oxidation state is the same as the cation ions. When the oxidation state of the dopants is different from the cation ions, the dopants are called aliovalent dopant. As mentioned in the bulk semiconductor doping, aliovalent doping will introduce either an extra electron (n-type) or extra hole (p-type) in the semiconductor. Aliovalent doping in nanocrystals, even though been less studied, also holds interesting properties targeting various applications. One of the properties comes from the free carriers donating from the aliovalent dopants. Like bulk semiconductor doping, some of the aliovalent dopants could also donate delocalized carriers either in the conduction band or in the valence band, such as Al^{3+} doped ZnO NCs, Sn^{4+} doped in In_2O_3 NCs, and the vacancy doped in Cu_{2-x}E ; E=S, Se, and Te NCs. These dopants are noted as shallow donor/acceptor. When the band carriers accumulated to a certain level, a plasmonic response occurs, noted as localized surface plasmon resonances (LSPR). These materials could be used in chemical sensing²¹, imaging^{22,23}, surface-enhanced Raman spectroscopy²⁴

²⁶, and enhanced optoelectronic²⁷ using near-field enhancement. This part will be discussed in detail in 1.2. Some other aliovalent dopants, however, due to their high binding energy, will not thermally activate electrons/holes into conduction band/valence band. These dopants are called deep donor/acceptor. The electron or holes could be compensated by the surface dangling bond or the defects such as cation/anion vacancy or interstitial. The oxidation state of the heterovalent dopants in the semiconductor nanocrystals can be tuned through the charge transfer from band carriers, so the aliovalent dopants could act as carrier transfer intermediate state. In the case of Fe³⁺ doped TiO₂ NCs, the electron excited to internally doped Fe³⁺ could transfer to surface Fe^{2+/3+} as co-catalysts. The electrons in the surface Fe³⁺ could efficiently cause multielectron reduction of absorbed oxygen molecules.²⁸

Besides the promising properties of doping in semiconductor NCs, challenges remain in the synthetic approach and analytical methods, especially for the aliovalent dopants. Effective dopant incorporation requires the dopant substitute the host atoms in the NC core. However, NCs undergo self-purification due to the higher formation energy of dopants incorporation compared to bulk materials.^{29,30} Under thermodynamic equilibrium, the dopant tends to be annealed out to minimize the overall free energy. Luckily, kinetic control the growth at the commonly used experimental temperature (< 400 °C). Balancing the dopant precursor activity and host cation precursor activity opens the opportunities for the dopant incorporation. Aliovalent dopants usually have larger crystal radius difference with the host ions compared to the isovalent dopant. For example, considering doping in ZnO NCs, Zn²⁺ has 0.74 Å crystal radius in tetrahedral symmetry. The crystal radius of Mn²⁺, Fe³⁺, Al³⁺ are 0.8 Å, 0.63 Å, and 0.53 Å respectively. A larger difference in crystal

radius results in higher formation energy for dopant incorporation and requires more effort to balance the kinetics during synthesis.

Another challenge is the dopant characterization. As mentioned before, the desired dopant incorporation is substitution the host ions in the core. After dopants been incorporated, there are four different dopant speciation, i.e. substitutional dopant, interstitial dopant, dopant stays on the surface, and dopant forms secondary phase. Differentiate the dopant speciation typically requires the information of dopant local coordination. Basic characterizations include elemental analysis by inductively coupled plasma atomic emission spectroscopy (ICP-AES), X-ray photoelectron spectroscopy (XPS), X-ray diffraction (XRD), and optical absorption or photoluminescence spectroscopy. These measurements cannot give the local information of dopant sites. For example, XRD can detect the secondary phase, however, when the secondary phase includes clusters forming by few atoms, the signal is broadened out. The absorption will show the dopant-induced ligand to metal charge transfer (LMCT) or metal to ligand charge transfer (MLCT), but all the speciation will show the LMCT/MLCT, and some of them may overlap, so based on the new absorption feature induced by the dopant, dopant speciation is still not clear.

In this report, we will approach both challenges, including a new synthetic strategy to bring more substituted aliovalent dopant in ZnO NCs and establish a method to differentiate different dopant speciation for Fe^{3+} in ZnO NCs. The report is divided into two main parts: deep donor in ZnO NCs and shallow donor in ZnO NCs. Each part has its own interest and approaches, in this chapter, a more detailed introduction is presented into two parts.

1.1. Deep Donor in Dilute Magnetic Semiconductor

Transition metal doping into semiconductor nanocrystals known as diluted magnetic semiconductor (DMSs) has attracted intense focus for the potential applications in spin-based information-processing technologies.³¹⁻³⁴ As mentioned previously, The spin state needs to stay long enough for storage and correction before reads out, thus long enough spin relaxation time is required. The spin relaxation is affected by the effective magnetic field in the NCs, since any effective magnetic field can interact with the magnetic moment of the electron's spin thus alter the electron's spin state. Once a spin encounters a new effective magnetic field, if the spin polarizations are not parallel or anti-parallel to the new magnetic field, the spin will precess about the field direction, known as Larmor precession. If the effective magnetic field originated from the spins of other electrons or holes in the NCs, from the nuclear spin, or from spin-orbit interactions, the relaxation mechanism is called spin-spin relaxation, known as T_2 . Among those, spin-orbit interaction is one of the major mechanisms that determine the spin relaxation time. Spin-orbit interaction can be treated simply as electrons orbiting around the nucleus. Imagine an observer sitting on the electron, the proton will appear to rotate around the observer and creating a magnetic flux density on the electron. This magnetic flux density is proportional to the orbital angular momentum. Another source of effective magnetic field can come from the phonon scattering in the NCs. This is called spin-lattice relaxation, known as T_1 . The phonon scattering will randomly change the electron's velocity or wavevector k , thus changes the magnetic flux density from the spin-orbit interaction. This further affects the spin precession direction, hence, the spin polarization changes randomly in time resulting in relaxation.

ZnO is a common matrix used for DMSs due to both the superior optical properties that allow optically spin preparation, manipulation, readout as well as the abundant nuclear spin-free isotopes of Zn (96%) which could help to reduce the spin-relaxation.³⁵ The study of DMSs has been dominated by the isovalent dopant such as Mn²⁺.^{32,33} Mn²⁺ has a half-filled d-shell (d⁵), when doped into tetrahedral coordination lattice, the ground state ⁶A₁ has no orbital momentum, this could help to reduce the spin-orbit interaction, thus lengthen the spin relaxation time further.

Fe³⁺ is predicted to be even more suitable for DMSs targeting spintronics application. Fe³⁺ has the same d⁵ configuration, however, Fe has no nuclear spin and this could stabilize more compared to Mn²⁺. Indeed, 1.4 ms spin coherence time (T₂) has been observed in Fe³⁺ doped ZnO³⁵ compared to 0.9 μs for Mn²⁺ doped ZnO nanocrystals.³³

Fe³⁺, if doped into ZnO nanocrystals, act as a deep donor. However, Most of the experimental studies of Fe dopants in ZnO nanostructures or bulk powders exhibit the mixture of both 2+/3+ oxidation states.³⁶⁻³⁹ Kataoka *et al.* have shown the presence of multiple Fe geometries and oxidation states in ZnO nanocrystals using XAS and X-ray magnetic circular dichroism spectroscopy: octahedral Fe³⁺ (~65%), tetrahedral Fe³⁺ (~15%), and tetrahedral Fe²⁺ (~20%).³⁸ Karmakar *et al.* proposed the core-shell structure in which Fe³⁺ is on or near the ZnO surface and Fe²⁺ ions are located mostly in the ZnO core.³⁶ By using various X-ray spectroscopic techniques, McLeod *et al.* presented similar evidence for Fe²⁺ substitution in bulk ZnO with Fe³⁺ dopants near the surface.³⁹

The dopant oxidation state can be roughly estimated by the redox potential of each dopant relatively to the band potential. Ligand to metal charge transfer (LMCT) combined

with metal to ligand charge transfer (MLCT) describe the position of dopant redox potential, as seen in Figure 1.3(a).

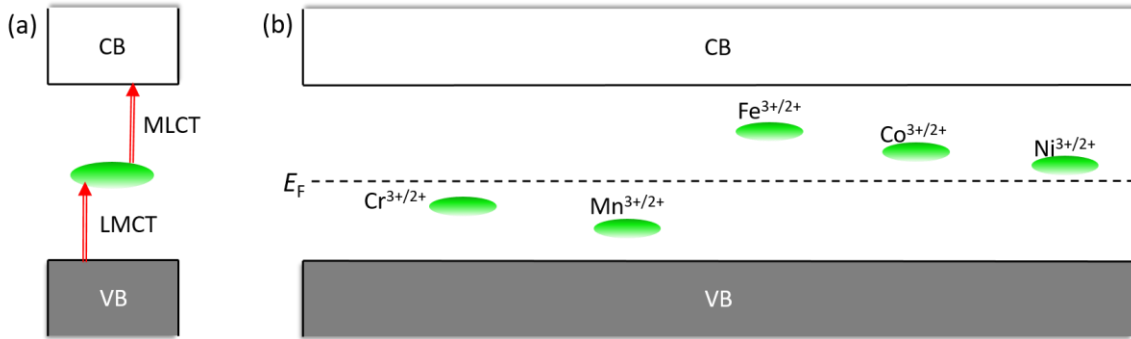


Figure 1.3. (a) Illustration of estimation of dopant redox potential within the ZnO band potential using ligand to metal charge transfer (LMCT) and the metal to ligand charge transfer (MLCT). (b) Calculated redox potential of first-row transition metals. The data is based on the calculation in reference ³¹. The Fermi level is set in the middle as an ideal case.

Charge transfer transition energies can be predicted using Jørgensen's optical electronegativity model⁴⁰ following the eq 1.1.4, in which the energy of $L_{VB}MCT$ are related to the difference between the optical electronegativity (χ) of the donor (D, here is valence band) and acceptor (A, here is dopant center).

$$E_{CT} = 30,000cm^{-1} \left(\chi_{opt}(D) - \chi_{opt}(A) \right) + \Delta SPE \pm 10Dq$$

(Eq 1.1.4)

ΔSPR refers to the difference in spin pair energy for before and after the transition.

$10Dq$ refers to the ligand field correction.

Figure 1.3b shows the calculated redox potentials for first-row transition metals. $Fe^{2+/3+}$ shows the highest redox potential, way higher than mid of the gap where the idealized Fermi level expected to be. So Fe^{2+} can donate an electron into the lattice. Since

the redox potential is still lower than the conduction band potential, Fe^{3+} can only act as a deep donor.

However, the coexistence of the $2+/3+$ in the experimental results indicates much more complicated situations in the nanocrystal. Part of the reason is due to the ambiguous of Fermi level. ZnO is usually n-type by its nature due to the possible existence of oxygen vacancies. N-type nature will raise the Fermi level, and it is also dependent on the preparation methods. When the Fermi level is higher than the dopant redox level, the deep donor could become isovalent dopant. Another reason for the coexistence results comes from the lack of clear analytical probes for the dopant speciation. The incorporation of the dopants can stay at the substitutional site, interstitial site, surface site or even forming segregated clusters. Each analytical probe has its own strengths and limitations; thus, the identification of the dopant speciation remains a challenge.

In this thesis, Chapter 2 will establish a dopant-specific method to identify the Fe^{3+} speciation in ZnO nanocrystals using electron paramagnetic resonance (EPR) and EPR simulation. Only $3+$ of the Fe is observed occupying both pseudo-tetrahedral (substitutional at the Zn-site) and pseudo-octahedral (surface and interstitial) coordination environment. The growth study shows the dopant distribution across the nanocrystals.

Chapter 3 studies the effects of photo-charging on the electronic structure of Fe^{3+} doped ZnO colloidal nanocrystals. Stepwise photodoping slowly increases the Fermi level of the system. We observe the disappearance of the spectroscopic signatures attributed to both substitutional Fe^{3+} and interstitial Fe^{3+} in the ZnO host as a function of photodoping time, which precedes the appearance of the well-known localized surface plasmon

resonance from conduction band electrons in ZnO nanocrystals. These results suggest that the oxidation state of Fe³⁺ defects can be reversibly switched in ZnO nanocrystals.

1.2. Shallow Donor in Plasmonic Doped Metal Oxide Nanocrystals

When the dopant redox potential is close enough or higher than the conduction band potential, the n-type aliovalent dopants will donate degenerate electrons to the conduction band and resulting metallic behavior. These dopants are called shallow donor. When the carrier concentration in a material reaches high enough, a plasmonic response occurs. Metal is the most common plasmonic material. Since the electrons in the material are delocalized, when exposed to an external electromagnetic radiation, the delocalized charge carriers will collectively resonate within a material. The oscillations of the carriers causing displacement of the carriers relative to the core (the positive nuclei), and further leads to net charges at the nanoparticle surface. Such surface plasmon resonances (SPR) will propagate along a metal-dielectric interface. For a nanoparticle containing a high electron density, this resonance is confined as localized surface plasmon resonances (LSPR).

The most notable properties of LSPR materials is the so-called near-field enhancement (NFE). This is caused by the displacement of the charges in the nanocrystals creating an oscillating dipole, and itself creates an oscillating field upon absorbing a photon at the resonance frequency. This oscillating field will extend to the surrounding of the nanoparticle and is orders of magnitude enhanced compared to the incoming electric field and decay exponentially with distance.⁴¹ The NFE can be utilized for chemical sensing²¹, imaging^{22,23}, surface-enhanced Raman spectroscopy²⁴⁻²⁶, and enhanced optoelectronic²⁷. On the other hand, after absorbing the photon at the resonance frequency, part of the energy is released upon scattering with electrons and phonons. This results in an efficient local

heating of the nanoparticle within only several hundreds of femtoseconds.⁴² The heat is then transferred to the surrounding medium around the nanoparticles. This property has been utilized for photothermal therapy in cells.^{22,43}

The LSPR resonances create an absorption with large extinction cross sections when the resonance condition is matched:

$$\omega_{LSPR} = \sqrt{\frac{\omega_p^2}{1 + 2\varepsilon_m} - \gamma^2}$$

(Eq 1.1.5)

This is so called Drude-Lorentz model. Here, ε_m is the dielectric constant of the surrounding medium and γ is the damping constant. ω_p is the plasma frequency, which is a function of carrier concentration (n) and effective mass (m^*), as illustrated in Equation 1.1.6.

$$\omega_p = \sqrt{\frac{ne^2}{\varepsilon_0 m^*}}$$

(Eq 1.1.6)

Where e is the unit of elementary charge and ε_0 is the permittivity of free space.

The Drude-Lorentz model points out that the peak energy of LSPR is largely impacted by the carrier concentration in the nanoparticles (see Figure 1.4a). As for metals, such as Au and Ag, the carrier densities can reach up to 10^{23} cm^{-3} , this in return determines the LSPR for Au and Ag nanoparticles at the visible spectrum. The LSPR energy tuning can be achieved by adjusting the size and morphology of the metal nanostructures.⁴⁴⁻⁴⁶ However, the rigid of carrier densities for Au and Ag nanoparticles limits the tuning ability.

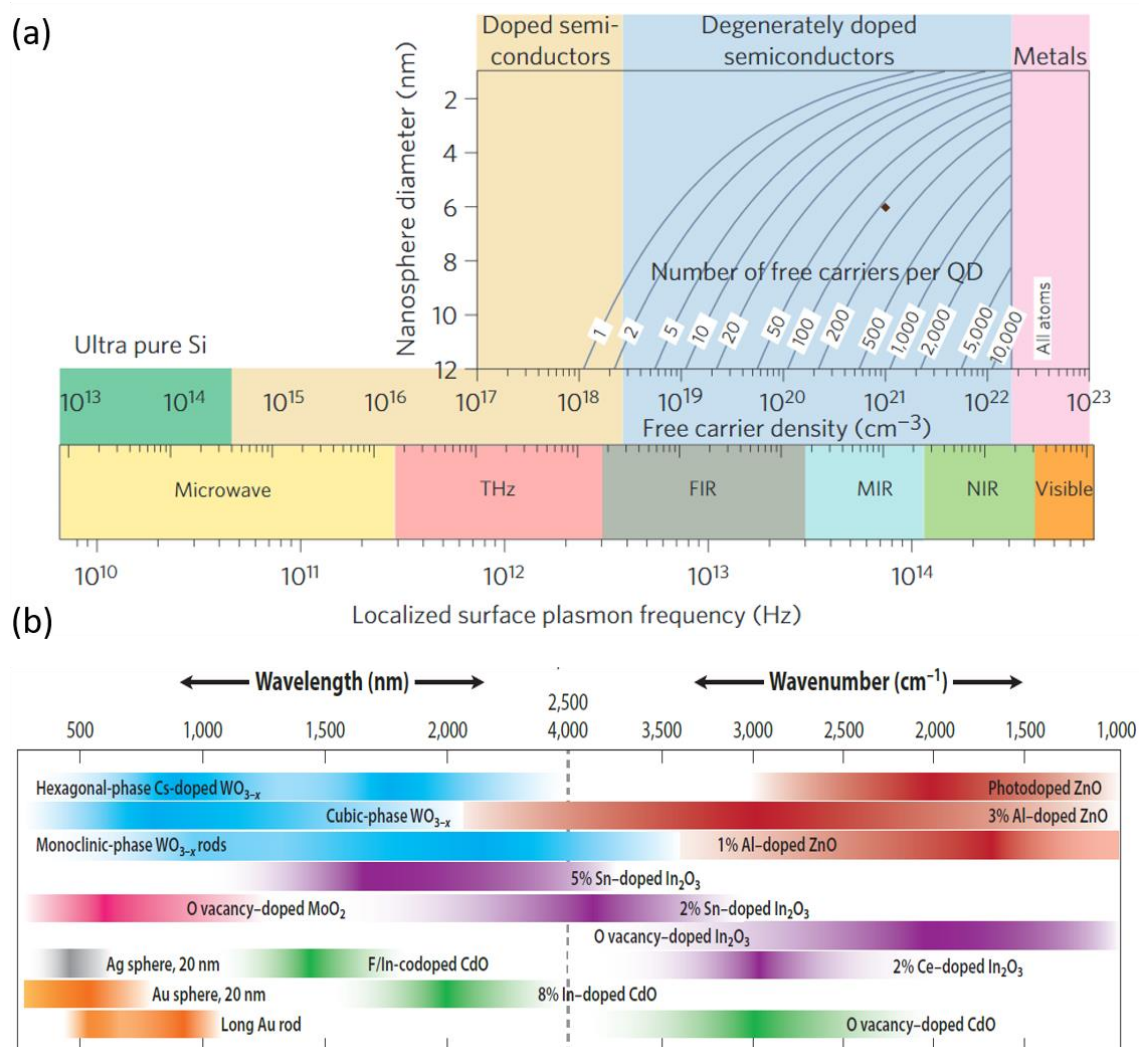


Figure 1.4. (a) Localized surface plasmon resonance (LSPR) frequency dependence on free carrier density and doping constraints. (Adapted from reference 47) (b) LSPR extinction spectra color map (gradients express LSPR spectra, with the maximum darkness corresponding to peak position) of doped metal oxide and metal nanocrystals spanning from the visible spectrum to the mid-IR spectrum. (Adapted from reference 48)

For aliovalent doped metal oxide nanoparticles, the conduction band electrons come from the donation of each dopant. Changing the chemical composition can easily tuning the LSPR energy.

As shown in Figure 1.4b, the carrier densities can be adjusted from 10^{18} - 10^{22} cm^{-3} by changing the elementary composition and dopant concentration. The LSPR energy can be reached from NIR to MIR.⁴⁹⁻⁵⁶ More importantly, tuning the LSPR energy through adjusting the chemical composition can maintain the optimized physical dimension for the target applications. Milliron group fabricated a smart window using the doped metal oxide nanocrystals.^{57,58} This window can tailor the plasmonic resonance through applied voltage. When light is needed, the window can filter the heat through absorbing the NIR photons with transparent in the visible spectrum or let the heat go through while blocking the visible light.

Tuning the LSPR energy by modifying the chemical composition requires a specifically synthetic method for each dopant-matrix composition. Doping in nanocrystals is a long-standing challenge and has stimulated intensive research.⁵⁹ The lattice strain introduced by the dopant limits the dopant incorporation. This is the case especially when dopant's ionic radius has a large mismatch with the cation ions, such as Al^{3+} in ZnO nanocrystals. On the other hand, even when the aliovalent dopant been substituted into the lattice, not every dopant will contribute electron to the conduction band. In fact, only 5% of Al^{3+} will donate electrons to conduction band when doped into ZnO nanocrystals has been reported.⁶⁰ The amount of electronically activated dopant varies drastically across the different synthetic methods for Sn^{4+} doped In_2O_3 nanocrystals.⁶¹ The author attributed the variation of the dopant activation to the dopant distribution difference across the several synthetic methods.

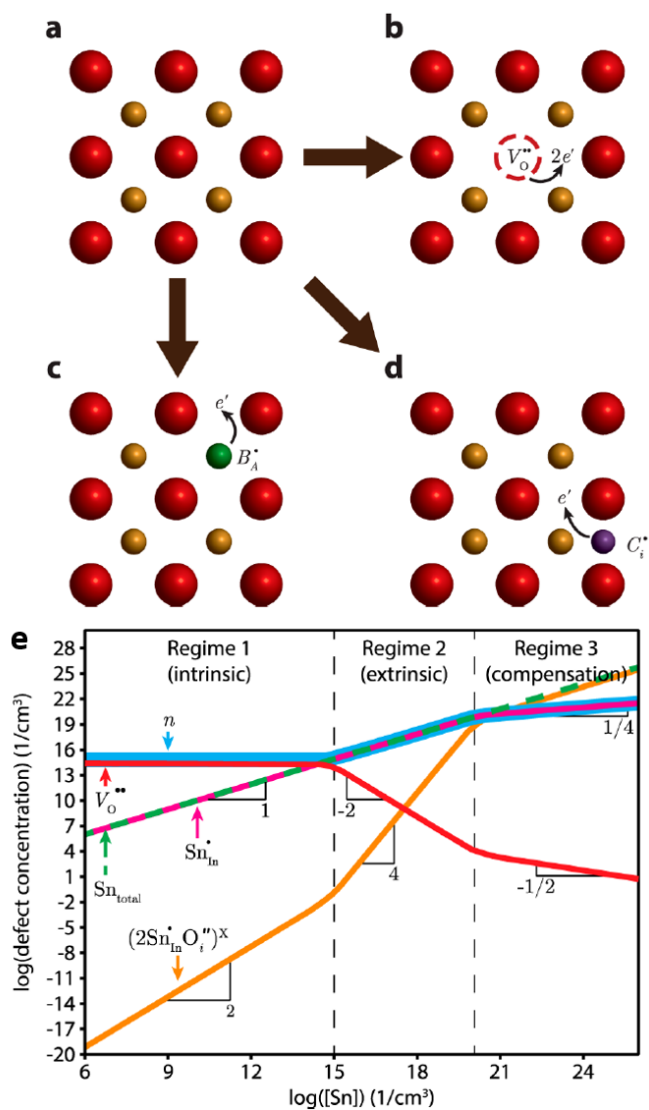


Figure 1.5. (a)-(d) Schematic representation of the common n-type doping mechanisms in the metal oxide. Orange sphere refers to metal cations, red sphere refers to oxygen anion, green sphere refers to the substitutional dopant, and purple sphere refers to interstitial dopant. (e) Brouwer defect equilibrium diagram for $[\text{Sn}]$ and oxygen vacancies in In_2O_3 at fixed partial O_2 pressure. (Adapted from reference ⁵⁰)

Figure 1.5 (a)-(d) shows the three common n-type doping mechanisms in metal oxide: oxygen vacancies, aliovalent substitutional dopants, and interstitial dopants. The opposite direction is the p-type doping mechanisms: interstitial oxygen and cation

vacancies. When the aliovalent substitutional dopant and interstitial oxygen or cation vacancies coexist, charge compensation will deactivate the dopant.

Agoston et al.⁶² and Hwang et al.⁶³ studied the defect chemistry in Sn⁴⁺ doped In₂O₃ to investigate the point defects effects on the carrier concentration and the Sn⁴⁺ compensation. (see Figure 1.5 e). The defect complexes ($2\text{Sn}_{\text{In}}^{\cdot} - \text{O}_i^{\ddot{\cdot}}$) is the main source for Sn⁴⁺ compensation. At low Sn⁴⁺ concentration, the free electrons are contributed by the intrinsic oxygen vacancies. Increase the Sn⁴⁺ concentration to the extrinsic region, the concentration of defect complexes ($2\text{Sn}_{\text{In}}^{\cdot} - \text{O}_i^{\ddot{\cdot}}$) is still negligible compared to the dopant concentration, thus most of the Sn⁴⁺ will donate electrons to the conduction band. At the compensation region, the compensation complex is more than the substituted Sn⁴⁺, thus increasing the dopant concentration lead to a saturation effect.

Up to now, we can conclude that the defect chemistry determines the aliovalent dopant activation, and it is also highly dependent on the synthetic conditions. However, synthetic strategies addressing both dopant incorporation issue together with the ability to tuning the defect chemistry remains challenging. The Chapter 4 of this thesis provides an etching and regrowth method for easily bringing Al³⁺ into ZnO nanoparticles. Further structure studies also confirm that the highly electronically activated Al³⁺ is originated from the less defect been created during synthesis.

Notes to Chapter 1:

- (1) Peng, X.; Wickham, J.; Alivisatos, A. P. *Journal of the American Chemical Society* **1998**, *120*, 5343.
- (2) Peng, Z. A.; Peng, X. *Journal of the American Chemical Society* **2001**, *123*, 183.
- (3) Peng, X.; Manna, L.; Yang, W.; Wickham, J.; Scher, E.; Kadavanich, A.; Alivisatos, A. P. *Nature* **2000**, *404*, 59.
- (4) Peng, Z. A.; Peng, X. *Journal of the American Chemical Society* **2002**, *124*, 3343.
- (5) Jaramillo, T. F.; Baeck, S. H.; Kleiman-Shwarsstein, A.; Choi, K. S.; Stucky, G. D.; McFarland, E. W. *J Comb Chem* **2005**, *7*, 264.
- (6) Osterloh, F. E. *Chemistry of Materials* **2008**, *20*, 35.
- (7) Santra, P. K.; Kamat, P. V. *Journal of the American Chemical Society* **2012**, *134*, 2508.
- (8) Beaulac, R.; Archer, P. I.; Ochsenein, S. T.; Gamelin, D. R. *Adv Funct Mater* **2008**, *18*, 3873.
- (9) Pradhan, N.; Peng, X. G. *Journal of the American Chemical Society* **2007**, *129*, 3339.
- (10) Norris, D. J.; Efros, A. L.; Erwin, S. C. *Science* **2008**, *319*, 1776.
- (11) Wang, S. Z.; Jarrett, B. R.; Kauzlarich, S. M.; Louie, A. Y. *Journal of the American Chemical Society* **2007**, *129*, 7702.
- (12) Pradhan, N.; Battaglia, D. M.; Liu, Y. C.; Peng, X. G. *Nano Lett* **2007**, *7*, 312.
- (13) Leger, Y.; Besombes, L.; Fernandez-Rossier, J.; Maingault, L.; Mariette, H. *Physical review letters* **2006**, *97*, 107401.
- (14) Fernandez-Rossier, J.; Aguado, R. *Physical review letters* **2007**, *98*, 106805.
- (15) Goryca, M.; Kazimierzuk, T.; Nawrocki, M.; Golnik, A.; Gaj, J. A.; Kossacki, P.; Wojnar, P.; Karczewski, G. *Physical review letters* **2009**, *103*, 087401.
- (16) Baudin, E.; Benjamin, E.; Lemaitre, A.; Krebs, O. *Physical review letters* **2011**, *107*, 197402.
- (17) Wang, F.; Banerjee, D.; Liu, Y.; Chen, X.; Liu, X. *The Analyst* **2010**, *135*, 1839.
- (18) Idris, N. M.; Gnanasammandhan, M. K.; Zhang, J.; Ho, P. C.; Mahendran, R.; Zhang, Y. *Nature medicine* **2012**, *18*, 1580.

- (19) Chen, G.; Qiu, H.; Prasad, P. N.; Chen, X. *Chemical reviews* **2014**, *114*, 5161.
- (20) Yang, Y.; Shao, Q.; Deng, R.; Wang, C.; Teng, X.; Cheng, K.; Cheng, Z.; Huang, L.; Liu, Z.; Liu, X.; Xing, B. *Angewandte Chemie* **2012**, *51*, 3125.
- (21) Anker, J. N.; Hall, W. P.; Lyandres, O.; Shah, N. C.; Zhao, J.; Van Duyne, R. P. *Nat Mater* **2008**, *7*, 442.
- (22) Zhou, Z. G.; Kong, B.; Yu, C.; Shi, X. Y.; Wang, M. W.; Liu, W.; Sun, Y. A.; Zhang, Y. J.; Yang, H.; Yang, S. P. *Sci Rep-Uk* **2014**, *4*.
- (23) Li, W. W.; Chen, X. Y. *Nanomedicine-Uk* **2015**, *10*, 299.
- (24) Abb, M.; Wang, Y. D.; Papasimakis, N.; de Groot, C. H.; Muskens, O. L. *Nano Lett* **2014**, *14*, 346.
- (25) Ghosh, S.; Saha, M.; Ashok, V. D.; Dalal, B.; De, S. K. *J Phys Chem C* **2015**, *119*, 1180.
- (26) Yockell-Lelievre, H.; Lussier, F.; Masson, J. F. *J Phys Chem C* **2015**, *119*, 28577.
- (27) Babicheva, V. E.; Boltasseva, A.; Lavrinenko, A. V. *Nanophotonics-Berlin* **2015**, *4*, 165.
- (28) Liu, M.; Qiu, X.; Miyauchi, M.; Hashimoto, K. *Journal of the American Chemical Society* **2013**, *135*, 10064.
- (29) Dalpian, G. M.; Chelikowsky, J. R. *Physical review letters* **2006**, *96*, 226802.
- (30) Erwin, S. C.; Zu, L.; Haftel, M. I.; Efros, A. L.; Kennedy, T. A.; Norris, D. J. *Nature* **2005**, *436*, 91.
- (31) Kittilstved, K. R.; Liu, W. K.; Gamelin, D. R. *Nat Mater* **2006**, *5*, 291.
- (32) Ochsenein, S. T.; Feng, Y.; Whitaker, K. M.; Badaeva, E.; Liu, W. K.; Li, X.; Gamelin, D. R. *Nature nanotechnology* **2009**, *4*, 681.
- (33) Ochsenein, S. T.; Gamelin, D. R. *Nature nanotechnology* **2011**, *6*, 112.
- (34) Kobak, J.; Smolenski, T.; Goryca, M.; Papaj, M.; Gietka, K.; Bogucki, A.; Koperski, M.; Rousset, J. G.; Suffczynski, J.; Janik, E.; Nawrocki, M.; Golnik, A.; Kossacki, P.; Pacuski, W. *Nature communications* **2014**, *5*, 3191.
- (35) Tribollet, J.; Behrends, J.; Lips, K. *Epl-Europhys Lett* **2008**, *84*.
- (36) Karmakar, D.; Mandal, S. K.; Kadam, R. M.; Paulose, P. L.; Rajarajan, A. K.; Nath, T. K.; Das, A. K.; Dasgupta, I.; Das, G. P. *Phys Rev B* **2007**, *75*.

- (37) Baum, L.; Meyer, M.; Richard, D.; Damonte, L. C.; Mendoza-Zelis, L. *Hyperfine Interact* **2007**, *176*, 87.
- (38) Kataoka, T.; Kobayashi, M.; Sakamoto, Y.; Song, G. S.; Fujimori, A.; Chang, F. H.; Lin, H. J.; Huang, D. J.; Chen, C. T.; Ohkochi, T.; Takeda, Y.; Okane, T.; Saitoh, Y.; Yamagami, H.; Tanaka, A.; Mandal, S. K.; Nath, T. K.; Karmakar, D.; Dasgupta, I. *J Appl Phys* **2010**, *107*.
- (39) McLeod, J. A.; Boukhvalov, D. W.; Zatsepin, D. A.; Green, R. J.; Leedahl, B.; Cui, L.; Kurmaev, E. Z.; Zhidkov, I. S.; Finkelstein, L. D.; Gavrilov, N. V.; Cholakh, S. O.; Moewes, A. *J Phys Chem C* **2014**, *118*, 5336.
- (40) Jorgensen, C. K. *Mol Phys* **1963**, *6*, 43.
- (41) Kelly, K. L.; Coronado, E.; Zhao, L. L.; Schatz, G. C. *J Phys Chem B* **2003**, *107*, 668.
- (42) Link, S.; El-Sayed, M. A. *Annual review of physical chemistry* **2003**, *54*, 331.
- (43) Liu, Q.; Sun, C.; He, Q.; Liu, D.; Khalil, A.; Xiang, T.; Wu, Z.; Wang, J.; Song, L. *Chemical communications* **2015**, *51*, 10054.
- (44) Chen, H.; Kou, X.; Yang, Z.; Ni, W.; Wang, J. *Langmuir : the ACS journal of surfaces and colloids* **2008**, *24*, 5233.
- (45) Nehl, C. L.; Liao, H.; Hafner, J. H. *Nano Lett* **2006**, *6*, 683.
- (46) Wiley, B. J.; Chen, Y.; McLellan, J. M.; Xiong, Y.; Li, Z. Y.; Ginger, D.; Xia, Y. *Nano Lett* **2007**, *7*, 1032.
- (47) Luther, J. M.; Jain, P. K.; Ewers, T.; Alivisatos, A. P. *Nat Mater* **2011**, *10*, 361.
- (48) Agrawal, A. J., R. Milliron, D. *Annu. Rev. Mater. Res* **2017**, *47*.
- (49) Runnerstrom, E. L.; Bergerud, A.; Agrawal, A.; Johns, R. W.; Dahlman, C. J.; Singh, A.; Selbach, S. M.; Milliron, D. J. *Nano Lett* **2016**, *16*, 3390.
- (50) Lounis, S. D.; Runnerstrom, E. L.; Llordes, A.; Milliron, D. J. *The journal of physical chemistry letters* **2014**, *5*, 1564.
- (51) Gordon, T. R.; Paik, T.; Klein, D. R.; Naik, G. V.; Caglayan, H.; Boltasseva, A.; Murray, C. B. *Nano Lett* **2013**, *13*, 2857.
- (52) Greenberg, B. L.; Ganguly, S.; Held, J. T.; Kramer, N. J.; Mkhoyan, K. A.; Aydil, E. S.; Kortshagen, U. R. *Nano Lett* **2015**, *15*, 8162.
- (53) Schimpf, A. M.; Gunthardt, C. E.; Rinehart, J. D.; Mayer, J. M.; Gamelin, D. R. *Journal of the American Chemical Society* **2013**, *135*, 16569.

- (54) Buonsanti, R.; Llordes, A.; Aloni, S.; Helms, B. A.; Milliron, D. J. *Nano Lett* **2011**, *11*, 4706.
- (55) Garcia, G.; Buonsanti, R.; Runnerstrom, E. L.; Mendelsberg, R. J.; Llordes, A.; Anders, A.; Richardson, T. J.; Milliron, D. J. *Nano Lett* **2011**, *11*, 4415.
- (56) Kim, J.; Agrawal, A.; Krieg, F.; Bergerud, A.; Milliron, D. J. *Nano Lett* **2016**, *16*, 3879.
- (57) Runnerstrom, E. L.; Llordes, A.; Lounis, S. D.; Milliron, D. J. *Chemical communications* **2014**, *50*, 10555.
- (58) Llordes, A.; Garcia, G.; Gazquez, J.; Milliron, D. J. *Nature* **2013**, *500*, 323.
- (59) Buonsanti, R.; Milliron, D. J. *Chemistry of Materials* **2013**, *25*, 1305.
- (60) Schimpf, A. M.; Ochsenbein, S. T.; Buonsanti, R.; Milliron, D. J.; Gamelin, D. R. *Chemical communications* **2012**, *48*, 9352.
- (61) Lounis, S. D.; Runnerstrom, E. L.; Bergerud, A.; Nordlund, D.; Milliron, D. J. *Journal of the American Chemical Society* **2014**, *136*, 7110.
- (62) Agoston, P.; Erhart, P.; Klein, A.; Albe, K. *Journal of physics. Condensed matter : an Institute of Physics journal* **2009**, *21*, 455801.
- (63) Hwang, J. *Solid State Ionics* **2000**, *129*, 135.

CHAPTER 2

CONTROL OVER Fe^{3+} SPECIATION IN COLLOIDAL ZNO NANOCRYSTALS

2.1. Introduction

The incorporation of transition metals ions into nanoscale II-VI semiconductors has led to the discovery of many interesting magnetic and photophysical phenomena.¹⁻⁵ The study of the chemistry and physics of doped colloidal semiconductor nanocrystals has been dominated in the literature by isovalent dopants such as Mn^{2+} ions.⁶⁻⁸ Recent advances in the synthetic methods of nanocrystals have enabled studies involving aliovalent dopants such as Al^{3+} in ZnO ($\text{Al}^{3+}:\text{ZnO}$) and $\text{In}^{3+}:\text{SnO}_2$ that display interesting plasmonic properties.⁹⁻¹¹ The stability of some transition metal ions such as Fe^{2+} and the early 3d ions has limited their incorporation into ZnO due to their tendency to oxidize. However, there are numerous reports of substitutional $\text{Fe}^{3+}:\text{ZnO}$ (bulk and nanocrystals) exhibiting interesting physical properties.¹²⁻¹⁶ It was also demonstrated that Fe^{3+} in single crystal ZnO possesses a long spin coherence lifetime that is largely limited by the isotopic purity of the ZnO.¹⁴ Therefore, a rational design element exists for exploring Fe-based diluted magnetic semiconductors (DMSs) for spin-based quantum computing applications compared to Mn^{2+} -based DMSs² that cannot avoid the inherent fast nuclear spin diffusion due to the $I = 5/2$ nuclear spin of ^{55}Mn . In addition, the possibility of combining paramagnetic and aliovalent dopant ions in a quantum-confined semiconductor nanocrystal could be achieved simultaneously with Fe^{3+} in ZnO.

Significant interest in transition-metal doping of wide gap semiconductors began after theoretical predictions of high temperature ferromagnetism in $\text{Mn}^{2+}:\text{ZnO}$.^{17,18} Ferromagnetic ordering mediated by shallow electron donors was also predicted based on

analysis of the charge transfer electronic structure of Fe²⁺:ZnO.¹⁹ Recently, Fe doped ZnO has received increased attention following the experimental reports of room temperature ferromagnetism in both thin films²⁰ and nanocrystals.²¹ However, antiferromagnetism was observed in polycrystalline samples synthesized by both solid-state and sol-gel processing.^{22,23} These contradicting results, combined with the possible formation of magnetic phases in the Fe-Zn-O phase diagram, have been major hurdles in formulating a detailed understanding of these materials in the bulk or with nanoscale dimensions.

The majority of experimental studies of Fe dopants in ZnO nanostructures or bulk powders report the oxidation state as a mixture of both 2+/3+ based either on Mössbauer,²⁴ EPR, or x-ray photoelectron (XPS) or absorption spectroscopy (XAS).^{21,25,26} Kataoka *et al.* have shown the presence of multiple Fe geometries and oxidation states in ZnO nanocrystals using XAS and x-ray magnetic circular dichroism spectroscopy: octahedral Fe³⁺ (~65%), tetrahedral Fe³⁺ (~15%), and tetrahedral Fe²⁺ (~20%).²⁵ Karmakar *et al.* proposed the core/shell structure in which Fe³⁺ is on or near the ZnO surface (shell) and Fe²⁺ ions are located mostly in the ZnO core.²¹ By using various X-ray spectroscopic techniques, McLeod *et al.* presented similar evidence for Fe²⁺ substitution in bulk ZnO with Fe³⁺ dopants near the surface.²⁶ For nanostructured materials with dimensions >30 nm the presence of mixed-valent Fe dopants appears to be a consensus, however, the speciation of Fe dopants in free-standing colloidal ZnO nanocrystals remains poorly understood. Colloidal forms of nanostructured inorganic materials have many advantages over powders including compatibility with existing solution processing technologies and by transmission-based spectroscopies. Of particular relevance to the study of DMS nanomaterials, colloidal suspensions allow for electronic structural investigations without

the presence of interfacial defects between aggregates that are not well understood and difficult to control.²⁷

We report the room-temperature solution synthesis and characterization of phase-pure, colloidal Fe³⁺ doped ZnO nanocrystals up to 2% cation mol fraction of Fe. Using EPR spectroscopy, we identify three unique sites for paramagnetic Fe³⁺ in the ZnO lattice: (1) substitutional at the Zn-site, (2) at a rhombically-distorted octahedral site attributed to interstitial Fe³⁺, and (3) directly-bound to the nanocrystal surface. The EPR spectrum of 0.15% Fe:ZnO closely matches the simulated spectrum using of Fe³⁺:ZnO single crystal after introducing only axial and rhombic strain induced by Fe³⁺ substitution and nanoscale dimensions. The electronic absorption and EPR spectra are consistent with the absence of Fe²⁺ ions in the ZnO lattice. Furthermore, we correlated growth kinetics with EPR spectroscopy to confirm previous results that doped ZnO nanocrystals prepared by this synthetic route result in nucleation of a pure ZnO core followed by incorporation of dopants only during growth.

2.2. Experimental Section

Materials: All chemicals were used without additional purification. Zn(OAc)₂ • 2H₂O (OAc = acetate, 98.0 – 101.0%, [Fe] = 5 ppm) was purchased from Ricca Chemical. Fe(OAc)₂ (94.4%), tetramethylammonium hydroxide pentahydrate (TMAOH, 99%), dodecylamine (DDA, 98%) were purchased from Acros Organics. Dimethylsulfoxide (DMSO, 99.9%), ethyl acetate (99.9%), heptane (99.3%), and toluene (99.96%) were purchased from Fisher. Ethanol (200 proof) was purchased from Pharmco-Aaper.

Synthesis of Fe:ZnO Colloidal Nanocrystals: The wet-chemical route used to prepare colloidal Fe:ZnO nanocrystals was modified slightly from an existing literature method.^{6,7}

Briefly, $\text{Zn}(\text{OAc})_2 \cdot 2\text{H}_2\text{O}$ (0.55 mg, 2.5 mmol) was dissolved in 25 mL DMSO. For Fe-doping, an amount equiv to 0.002 – 0.05 cation mol fraction of $\text{Fe}(\text{OAc})_2$ was added to the Zn^{2+} solution. The Fe^{2+} ion oxidizes readily Fe^{3+} under basic conditions. To initiate ZnO nucleation and growth, 1.7 equiv of TMAOH (0.77 g, 4.25 mmol) dissolved in 7.7 mL of ethanol was slowly added dropwise over 90 s to the Zn/Fe solution under vigorous magnetic stirring. Nanocrystal sizes were controlled by the reaction time or amount of added hydroxide solution.

The colloids were precipitated from the DMSO reaction solution by addition of ethyl acetate and centrifuged. The resulting pellet was suspended in ethanol followed by precipitation with heptane and centrifugation. Finally, the surfaces ligands were exchanged by heating the nanocrystal powder in neat DDA at 180 °C for various times. All synthetic procedures were performed under ambient conditions in a chemical fume hood.

Physical Methods: Electronic absorption spectra were collected using either a Czerny-Turner style dual-beam spectrophotometer (Varian Cary 50) or a fiber-optic based USB spectrophotometer (Ocean Optics UV-Vis 2000) equipped with a non-ozone producing 75 W Xe lamp (Oriel) and appropriate bandpass filters. Fourier transform IR spectroscopy was collected on a Varian 670 FT spectrometer equipped with a KBr beam splitter and DLaTGS detector for mid-IR spectra or with a near-IR quartz beam splitter and InGaAs detector for near-IR absorption measurements.

Room-temperature EPR spectra were collected with the TE102 mode of a dual-mode resonator operating at a frequency of 9.805 GHz (X-band, Bruker Elexsys E-500). Transmission electron microscopy images were collected on carbon coated (3 nm) Cu TEM

grids (JEOL JEM 2000FX). Fe concentrations were determined by inductively coupled plasma optical emission spectroscopy (ICP-OES, PerkinElmer 4300 DV).

The Spin-Hamiltonian and Simulation of EPR Parameters: Fe^{3+} ($3d^5$) with T_d symmetry has a 6A_1 ground term. The EPR spectra were simulated using the $S = 5/2$ spin Hamiltonian²⁸ given by Eq 2.2.1, including both axial and rhombic components to the zero-field splitting (D and E , respectively). Where \mathbf{g} is the Lande g -tensor, β is the Bohr magneton and H is the external magnetic field. The axial distortion of the wurtzite crystal field (C_{3v}) and 2nd order spin-orbit coupling from the 4T_1 excited state splits the 6A_1 ground term into three Kramers doublets separated by $2D$ and $6D$. The 4th order components a and F are cubic-field splitting parameters. For a thorough review and application of the spin Hamiltonian see refs. ²⁹ and ²⁸. EPR spectra were simulated with the spin-Hamiltonian parameters given in Table A1 (see Appendix A) using *EasySpin*.³⁰

$$\begin{aligned} \hat{H} = & \mathbf{g}\beta\vec{H} \cdot \hat{S} + D\left(\hat{S}_z^2 - \frac{35}{12}\right) + E(\hat{S}_x^2 - \hat{S}_y^2) \\ & + \frac{a}{6}\left(\hat{S}_\xi^4 + \hat{S}_\eta^4 + \hat{S}_\zeta^4 - \frac{707}{16}\right) \\ & + \frac{7F}{36}\left(\hat{S}_z^4 - \frac{95}{14}\hat{S}_z^2 + \frac{81}{16}\right) \end{aligned}$$

(Eq 2.2.1)

2.3. Result and Discussion

The electronic absorption spectra of colloidal ZnO and 0.78% Fe-doped ZnO QDs are shown in Figure 2.1. The ZnO band gap absorption dominates the spectra of both samples at 3.5 eV corresponding to a nanoparticle size of ~ 3.7 nm.³¹ The absorption spectrum of the Fe-doped ZnO sample also displays a weak and broad tail that extends down to ~ 2.2 eV that is responsible for its yellowish color. This visible transition has been observed previously¹⁵ in the excitation spectrum monitoring the ${}^4T_1(G) \rightarrow {}^6A_1$ emission of substitutional Fe^{3+} . Those authors attribute the transition to the excitation of an electron from the valence band to Fe^{3+} . The electronic configuration of this excited state is analogous to a ligand-to-metal charge transfer (LMCT) transition resulting in a localized Fe^{2+} center with a Coulombically bound valence band hole.¹⁹

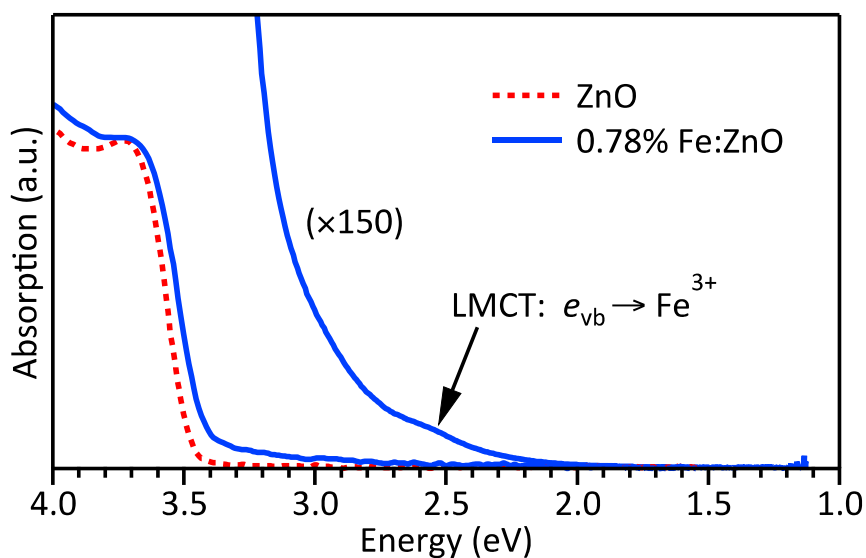


Figure 2.1. Electronic absorption spectra of ZnO (dotted line) and 0.78% Fe-doped ZnO (solid line) suspended in toluene at room temperature. The Fe:ZnO absorption spectrum is also displayed on an expanded y-scale ($\times 150$).

The broad ${}^5E \rightarrow {}^5T_2$ ligand field transition³² of substitutional $\text{Fe}^{2+}:\text{ZnO}$ at ~ 0.5 eV was not detected even in concentrated colloidal suspensions (not shown). However, based on the intense solvent overtones in the same region, we are unable to rule out the presence of substitutional Fe^{2+} in ZnO by absorption spectroscopy. However, indirect evidence that is consistent with the absence of Fe^{2+} in the dilute doping regime is discussed below.

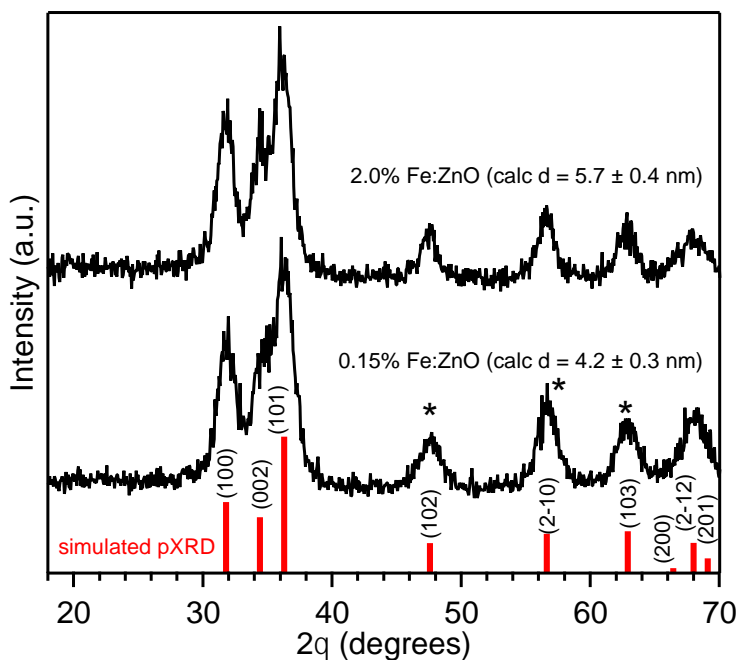


Figure 2.2. Powder X-ray diffraction patterns of 0.15% (bottom) and 2.0% (top) Fe:ZnO. The vertical lines with varying intensity are the reflections from bulk wurtzite ZnO (ICSD #82028). The asterisk (*) above the (102), (2-10) and (103) reflections denote that these peaks were fit to a Gaussian function and used in the Scherrer equation to determine the average grain size and deviation for the two samples. EPR spectra of these two samples were shown in Figure 2 of the text. Powder X-ray diffraction is less sensitive than EPR spectroscopy to minute secondary phases considering the nominal concentration of $\text{Fe}(\text{OAc})_2$ added to the $\text{Zn}(\text{OAc})_2$.

The XRD spectra of Fe-Doped ZnO are shown in Figure 2.2. No other secondary phase such as Iron oxide or Zinc ferrite are observed. However, XRD cannot give the information of dopant local structure, instead, we are using EPR to solve the problem.

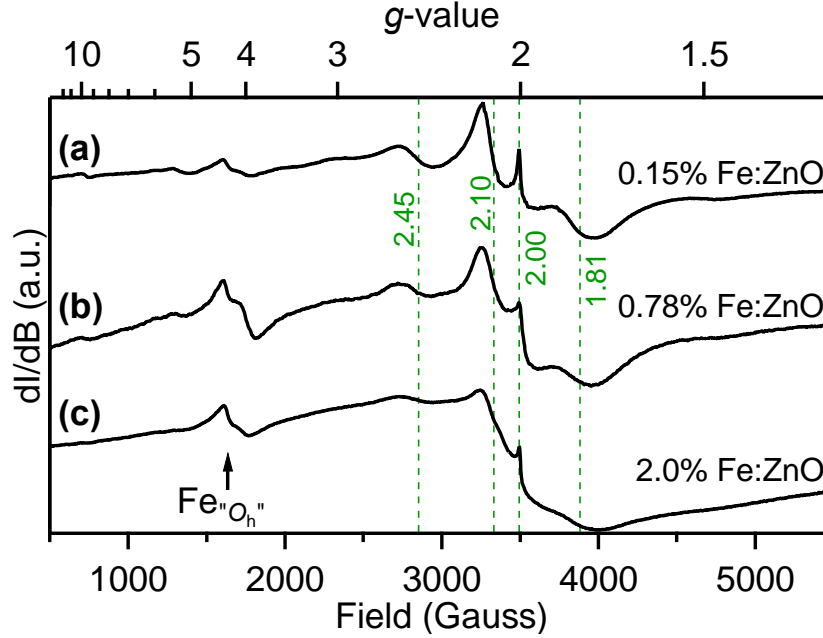


Figure 2.3. Room temperature X-band EPR spectra of colloidal Fe:ZnO QDs as a function of Fe concentration: (a) 0.15% Fe³⁺, (b) 0.78% Fe³⁺, and (c) 2.0% Fe³⁺. The dashed, vertical lines denote major resonances and associated effective g -values.

The EPR spectra of Fe³⁺-doped ZnO with Fe concentrations from 0.15% - 2.0% are shown in Figure 2.3. All Fe³⁺:ZnO QDs in Figure 2.3 were heated in dodecylamine (DDA) at 180 °C for 30 min to enable dispersion of the QDs in toluene and remove surface Fe³⁺ species. With increasing Fe content, the intense resonances spanning g -values from 1.5 to 3 broaden significantly and the weaker resonances above $g > 5$ disappear from increased dipole-dipole coupling and inhomogeneous broadening. In addition, there is an asymmetric resonance at $g' = 4.2$ that is present in all of the spectra.

To confirm the identity of the Fe³⁺ species we compared the experimental spectra for the 0.15% Fe³⁺:ZnO nanocrystals with the simulated EPR spectrum of Fe³⁺:ZnO single crystal using the spin-Hamiltonian parameters determined by Walsh and Rupp²⁹ ($D = -593.7 \times 10^{-4} \text{ cm}^{-1}$, $E = 0$, $a = 39 \times 10^{-4} \text{ cm}^{-1}$, $F = 4 \times 10^{-4} \text{ cm}^{-1}$ and $g_{\text{iso}} = 2.0062$). Figure

2.4 shows the different simulations using the single-crystal EPR parameters of $\text{Fe}^{3+}:\text{ZnO}$. Figure 2.4a shows the single crystal parameters with only the addition of 30 G peak-to-peak linewidth (isotropic broadening). The agreement between this simulated spectrum and the 0.15% $\text{Fe}^{3+}:\text{ZnO}$ nanocrystals shown in Figure 2.4d is poor. Although increasing the isotropic broadening of the lines does result in better agreement of some of the broader resonances, the sharp fine structure disappears entirely (especially at $g' = 2.00$). There is a dramatic improvement between the simulated spectrum and experiment with the introduction of D -strain (ΔD) as shown in Figure 2.4b. Additional improvement of the simulated spectrum is obtained with the addition of E -strain (ΔE) as seen in Figure 2.4c.

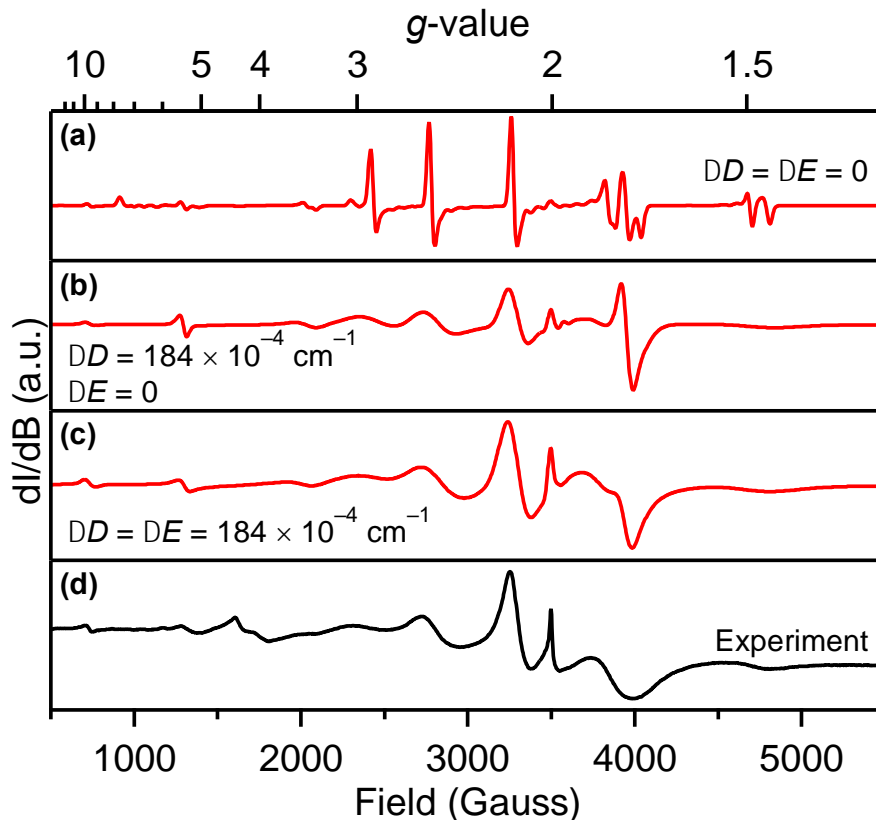


Figure 2.4. Comparison between the (d) experimental EPR spectrum of 0.15% Fe:ZnO colloidal nanocrystals and the simulated spectra with varying strain on the bulk EPR parameters: (a) $\Delta D = \Delta E = 0$, (b) $\Delta D = 184 \times 10^{-4} \text{ cm}^{-1}$ and $\Delta E = 0$ and (c) $\Delta D = \Delta E = 184 \times 10^{-4} \text{ cm}^{-1}$.

The lattice strain caused by the large surface-to-volume ratio of the ZnO nanocrystal increases the inhomogeneous line widths of the EPR transitions and creates a distribution in the ZFS parameters. This effect has been observed previously in colloidal $\text{Mn}^{2+}:\text{ZnO}$ nanocrystals⁷ and is accounted for in the EPR simulations by adding D -strain, which is estimated to be $\Delta D = 184 \times 10^{-4} \text{ cm}^{-1}$ ($\Delta D/|D| = \sim 28\%$) for 0.15% Fe:ZnO. In comparison, $\Delta D/|D|$ ratios as large as $\sim 26\%$ have recently been reported in heteroepitaxial films of $\text{Mn}^{2+}:\text{ZnO}$.²⁸ We suspect that the main contribution to the lattice strain is a combination of increased surface-to-volume ratio in the nanocrystalline hosts and the large mismatch in effective ionic radii between Fe^{3+} (0.49 Å) and Zn^{2+} (0.60 Å). This difference in ionic radii is larger than Zn^{2+} substitution by Mn^{2+} (0.66 Å).³³

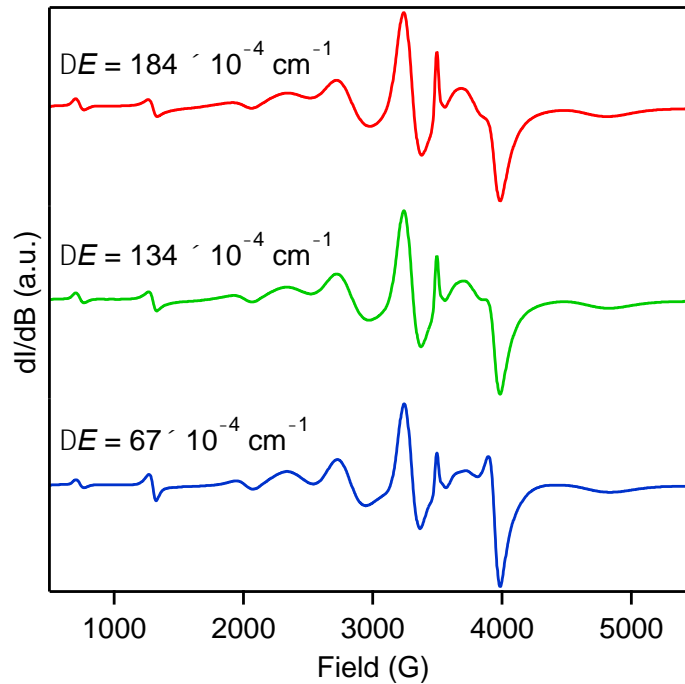


Figure 2.5. Effect of varying the magnitude of E -strain on the simulated EPR spectrum ($\Delta D = 184 \times 10^{-4} \text{ cm}^{-1}$).

In the hexagonal ZnO single crystal there is no static rhombic distortion to the crystal field. However, the lattice strain could lead to E -strain while $E = 0$. By introducing an equivalent E strain ($\Delta E = \Delta D$), the agreement between the simulated spectrum shown in Figure 2.4c and the experimental spectrum is greatly improved. The sharp feature at $g' = 2.00$ actually becomes more resolved with increasing E -strain in the simulations as expected since this feature is assigned to transitions between the $m_S = \pm 1/2$ Kramers doublet (see Figure 2.5). The introduction of ΔE in $\text{Mn}^{2+}:\text{ZnO}$ was also required to fit the EPR spectrum only when grown on sapphire substrates, but not when grown on lattice-matched ZnO.²⁸ Surface strain due to shape anisotropy and Fe^{3+} substitution could provide a similar E -strain effect in the colloidal $\text{Fe}^{3+}:\text{ZnO}$ nanocrystals presented here.

In contrast to previous reports on bulk or nanocrystalline powders,^{13,29} we also observe an additional resonance in the EPR spectra at $g' = 4.2$. This asymmetric resonance does not shift nor broaden with increasing Fe mol fraction in contrast to substitutional Fe^{3+} shown in Figure 2.3. To further investigate the origin of transition and the overall evolution of the Fe^{3+} speciation we monitored the EPR spectra at separate times during nanocrystal growth.

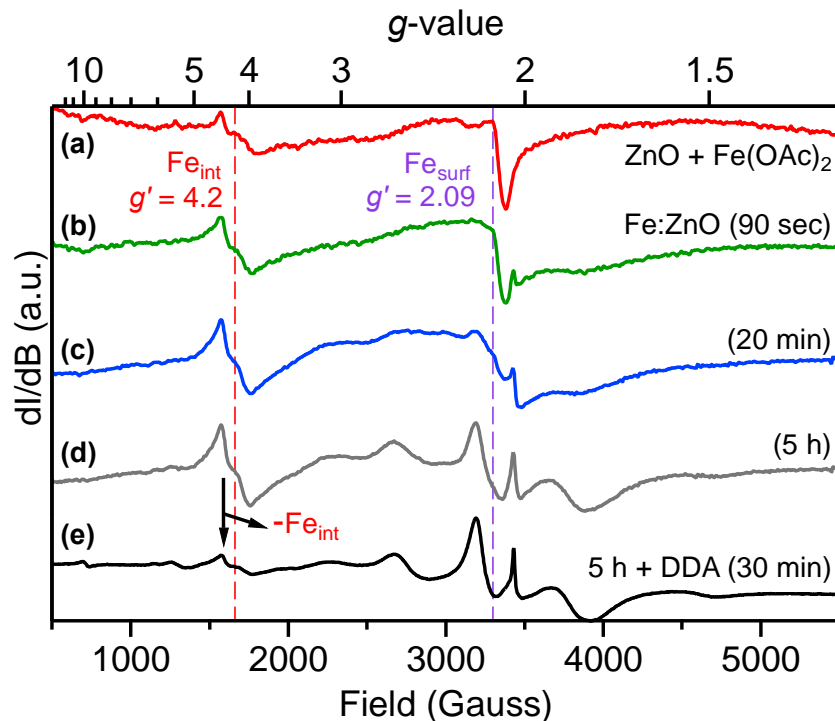


Figure 2.6. Room-temperature X-band EPR spectra of: (a) Fe directly bound to the surface of ZnO QDs (~ 4 nm); Fe^{3+} :ZnO (0.5% nominal Fe mol fraction) as a function of growth time without heating in DDA after (b) 90 s, (c) 20 min, and (d) 5 h; and (e) after extended ligand exchange of sample (d) with DDA at 180 °C for 30 minutes under N_2 flow. The vertical dashed lines at $g' = 4.2$ and 2.09 denotes the position of the additional interstitial and surface-related Fe^{3+} resonances, respectively.

The EPR spectra of Fe^{3+} :ZnO QDs after addition of 1.7 equivalents of TMAOH at various growth times are shown in Figure 2.6. As a control, we prepared “surface-only” Fe^{3+} :ZnO by adding 0.5% $\text{Fe}(\text{OAc})_2$ to undoped colloidal ZnO nanocrystals that were allowed to grow for 30 minutes after addition of the TMAOH (see Figure 2.6a). The EPR spectrum of these surface-bound Fe^{3+} species displays a sharp negative feature with a maximum at $g' = 2.09$ and a much weaker asymmetric peak at $g' = 4.2$ similar to the feature observed in Figure 2.3 for the DDA-treated Fe^{3+} :ZnO nanocrystals in toluene. Figures 2.6b-d show the EPR spectra of Fe :ZnO nanocrystals collected with increasing growth

times from 90 s to 5 h. These spectra display clear evolution of the Fe^{3+} speciation during the Ostwald ripening process of $\text{Fe}^{3+}:\text{ZnO}$ nanocrystals. Only 90 s after addition of TMAOH, the spectrum resembles some of the features of the surface-bound spectrum in Figure 2.6a with the exceptions that now the $g' = 4.2$ peak dominates the spectrum and there is the appearance of a weak, but sharp resonance at $g' = 2.00$ that is consistent with substitutional Fe^{3+} in ZnO (see experimental and simulated spectra in Figures 2.3 and 2.4). With increasing growth time to 20 min, the relative amount of substitutional Fe^{3+} in the region between $g = 1.5$ and 3.0 increase compared to the $g' = 4.2$ resonance. In addition, the sharper resonance at $g' = 2.09$ becomes a shoulder that is largely occluded by the increasing presence of substitutional Fe^{3+} . Even after 5 h of $\text{Fe}^{3+}:\text{ZnO}$ growth, the $g' = 4.2$ resonance still contributes significantly to the EPR spectrum, but the relative intensity of the substitutional Fe^{3+} signal has clearly increased compared to the 20 min spectrum.

It is known that surface impurities can be removed from ZnO QDs by heating in neat DDA at 180 °C for 30 min under N_2 flow.^{6,7,34} When we perform the same surface ligand exchange procedure on the $\text{Fe}:\text{ZnO}$ QDs we observe a significant decrease in the intensity of the $g' = 4.2$ peak and total disappearance of the $g' = 2.09$ (Figure 2.6e). The $g \sim 4.2$ feature is prevalent in Fe^{3+} -metalloproteins such as transferrin³⁵ and is typically associated with rhombically-distorted octahedral coordination environments. In strongly rhombic systems, the three pairs of Kramers doublets effectively mix and as a consequence the $\Delta S = \pm 1$ selection rule for EPR-allowed transitions is relaxed.³⁶ We therefore assign the $g' = 4.2$ to pseudo-octahedral Fe^{3+} presiding near the ZnO surface at an interstitial site with a large rhombic component to the ZFS ($E/D \sim 1/3$).³⁷

Based on the position and shape of the resonances, and the evolution of the spectra shown in Figure 2.6, we conclude that the $g' = 2.09$ and 4.2 resonances in Figure 2.6a are not correlated and therefore must originate from two unique surface-related Fe^{3+} sites. If these two signals were truly correlated, then the two signals would have the same relative intensities between Figure 2.6a and 2.6b. We thus attribute the $g' = 2.09$ resonance to surface-bound Fe^{3+} based on the fact that it dominates the spectrum in Figure 2.6a, but decreases in the $\text{Fe}^{3+}:\text{ZnO}$ spectrum after only 90 s of growth while the surface-related interstitial $g' = 4.2$ signal increases significantly (see Figure 2.6b).

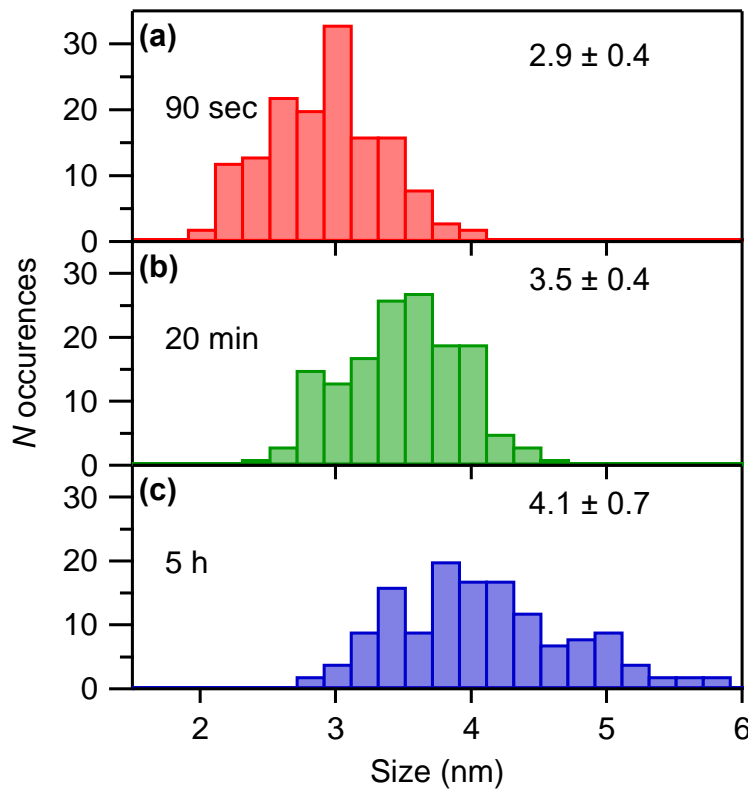


Figure 2.7. Histograms from TEM particle analysis as a function of $\text{Fe}^{3+}:\text{ZnO}$ growth times for samples shown in Figure 4: (a) 1 min 30 sec (b) 20 min (c) 5h.

The spectra presented in Figure 2.6 are consistent with previous reports that have established that substitutional transition metal dopants are excluded from the critical nucleus during the synthesis of doped ZnO QDs.^{6,7,38} In addition to EPR spectroscopy as a function of growth time, we also measured the average sizes and size distribution of the Fe:ZnO QDs by transmission electron microscopy (TEM, see figure 2.7). The average particle size once all TMAOH has been added is $\sim 2.9 \pm 0.4$ nm ($t = 90$ s) by TEM analysis. This size is much larger than the critical nucleus estimated to comprise 25 Zn^{2+} ions (~ 1.1 nm) for ZnO ³⁸ and form after only ~ 0.4 equivalents of TMAOH have been added.⁶ The appearance of substitutional Fe^{3+} in the larger ZnO nanocrystals after 90 s of growth is evident by the sharp feature at $g' = 2.00$ in Figure 2.6b. In addition, the increased surface-to-volume ratio in smaller particles results in a high ratio of surface-related Fe^{3+} signals at $g' = 2.09$ and 4.2. After 5 h, the particle size is $\sim 4.1 \pm 0.7$ nm and the Fe^{3+} ions are distributed among substitutional and the two surface-related sites. The proposed mechanism for dopant incorporation is summarized in Figure 2.8. Previously, Schwartz *et al.* observed a surface-bound Co^{2+} intermediate by electronic absorption spectroscopy during the growth of $\text{Co}^{2+}:\text{ZnO}$ using a similar synthetic procedure.⁶ By utilizing EPR spectroscopy, we are able to elucidate much more detail, including the number of Fe^{3+} sites. The additional pseudo-octahedral rhombic site near the ZnO surface is likely indistinguishable from the pseudo-octahedral surface site when studied by electronic absorption spectroscopy of $\text{Co}^{2+}:\text{ZnO}$.

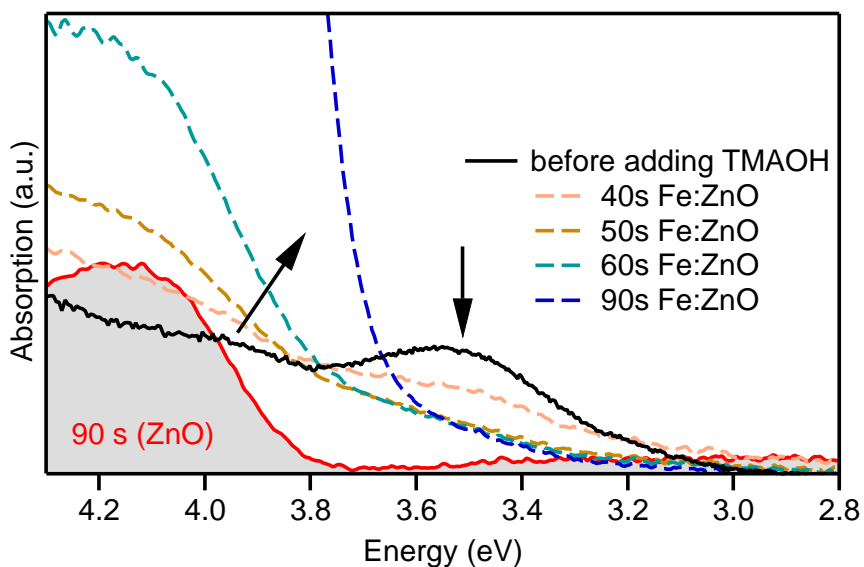


Figure 2.8. Absorption spectra of 0.5% Fe:ZnO before (black solid line) and after TMAOH addition at various reaction times (dashed lines), and ZnO after 90 s of TMAOH addition (red solid line, shaded under curve).

The absorption spectrum of Fe:ZnO QDs in the band gap region was also monitored³⁹ *in situ* as a function of growth time after ZnO nucleation was initiated by the addition of 1.7 equiv of TMAOH. Figure 2.8 shows a broad feature at 3.5 eV in the absorption spectrum of Fe(OAc)₂ and Zn(ac)₂ in DMSO prior to adding TMAOH. This absorption band is tentatively assigned to the LMCT transition of pseudo-octahedral Fe²⁺, Fe³⁺, or basic Fe(III) acetate, [Fe₃O(OAc)₆(H₂O)₃]OAc in solution. After addition of TMAOH the 3.5 eV band decreases in intensity with increasing growth time and disappears after 90 s. Concomitantly, the ZnO first exciton gains intensity and redshifts in energy with increasing growth time. The growth dependence is consistent with nucleation and growth of a pure ZnO core followed by adsorption and incorporation of Fe³⁺.

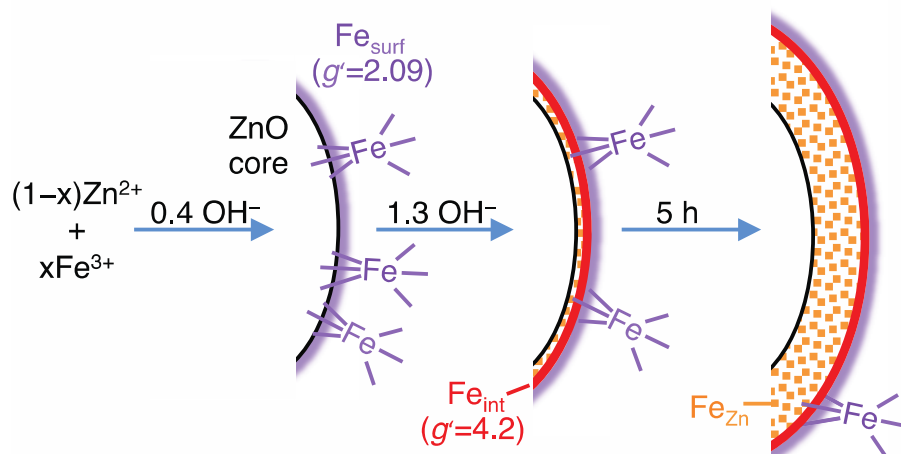


Figure 2.9. Schematic representation for the proposed mechanism of Fe^{3+} incorporation into colloidal ZnO nanocrystals during nanocrystal growth.

Despite the typical EPR silence of non-Kramers ground states, the presence of Fe^{2+} and Fe^{3+} in ZnO results in a very broad signal in the EPR spectrum at $g' = 2$. Even at our highest doping level of 2% Fe, we do not observe any blocking temperature in the zero-field-cooled and field-cooled magnetic susceptibility (see figure 2.10). In addition, we can also rule out its origin to secondary nanoscale phases of zinc ferrite or Fe_2O_3 that display very broad ferromagnetic resonances.^{40,41} Therefore, Fe^{2+} is likely absent in these Fe-doped ZnO nanocrystals. The Mössbauer spectroscopy confirming Fe^{3+} is the only oxidation state for dopant Fe will be discussed in Chapter 3.

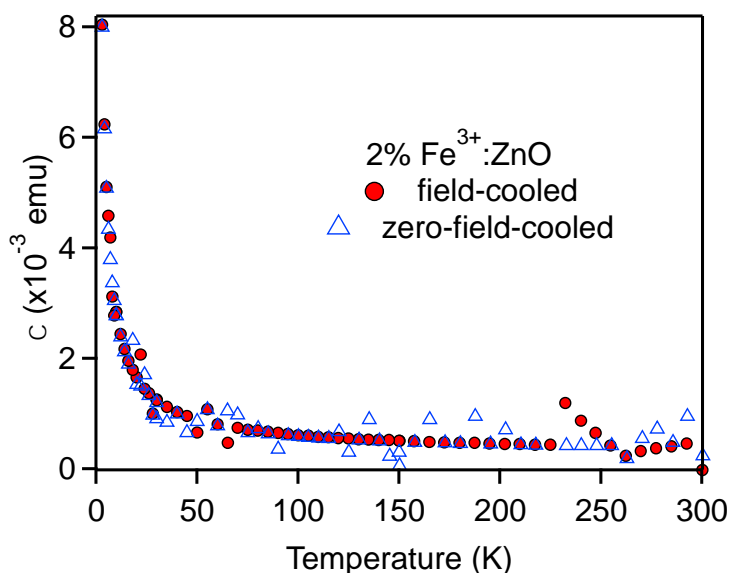


Figure 2.10. Zero-field-cooled (ZFC) and field-cooled (FC) magnetic susceptibility of 2% $\text{Fe}^{3+}:\text{ZnO}$ nanocrystals. The magnetic field strength for the FC curve and susceptibility measurement was 5000 Oe. Although somewhat noisy as higher temperatures, the ZFC and FC susceptibility curves are superimposable, especially at lower temperatures.

2.4. Conclusions

In conclusion, we have successfully prepared Fe^{3+} -doped ZnO as nanocrystalline colloids that are readily dispersed in non-polar organic solvents. We utilized EPR spectroscopy to confirm three unique and isolated Fe^{3+} sites: (1) substitutional doping of Fe^{3+} at the Zn^{2+} sites and (2) rhombically-distorted Fe^{3+} octahedra located near the ZnO nanocrystal surface at an interstitial site and (3) directly bound to the ZnO surface. The large mismatch in effective ionic radii between the Fe^{3+} and Zn^{2+} and large surface-to-volume ratios contribute to inhomogeneous broadening of the EPR spectrum and to the axial *and* rhombic strain as demonstrated by the comparison of simulated and experimental EPR spectra. The lack of a broad ferromagnetic resonance in the EPR spectrum is consistent with an absence of mixed-valency (i.e., Fe^{2+}) or magnetic FeO_x phases in the

dilute doping limit. The successful preparation of $\text{Fe}^{3+}:\text{ZnO}$ nanocrystals in the quantum confinement regime opens the door to transmission-based spectroscopic investigations of the electronic structure that until now have been limited in this material to single crystals or thin films. In addition, we are actively pursuing strategies to exploit the rich redox activity of Fe^{3+} for a variety of potential energy-based technologies.

Notes to Chapter 2:

- (1) Beaulac, R.; Schneider, L.; Archer, P. I.; Bacher, G.; Gamelin, D. R. *Science* **2009**, 325, 973.
- (2) Ochsenbein, S. T.; Gamelin, D. R. *Nat Nanotechnol* **2011**, 6, 111.
- (3) Ochsenbein, S. T.; Feng, Y.; Whitaker, K. M.; Badaeva, E.; Liu, W. K.; Li, X. S.; Gamelin, D. R. *Nat Nanotechnol* **2009**, 4, 681.
- (4) Beaulac, R.; Archer, P. I.; van Rijssel, J.; Meijerink, A.; Gamelin, D. R. *Nano Lett.* **2008**, 8, 2949.
- (5) Santra, P. K.; Kamat, P. V. *J. Am. Chem. Soc.* **2012**, 134, 2508.
- (6) Schwartz, D. A.; Norberg, N. S.; Nguyen, Q. P.; Parker, J. M.; Gamelin, D. R. *J. Am. Chem. Soc.* **2003**, 125, 13205.
- (7) Norberg, N. S.; Kittilstved, K. R.; Amonette, J. E.; Kukkadapu, R. K.; Schwartz, D. A.; Gamelin, D. R. *J. Am. Chem. Soc.* **2004**, 126, 9387.
- (8) Radovanovic, P. V.; Norberg, N. S.; McNally, K. E.; Gamelin, D. R. *J. Am. Chem. Soc.* **2002**, 124, 15192.
- (9) Schimpf, A. M.; Ochsenbein, S. T.; Buonsanti, R.; Milliron, D. J.; Gamelin, D. R. *Chemical communications* **2012**, 48, 9352.
- (10) Llordes, A.; Garcia, G.; Gazquez, J.; Milliron, D. J. *Nature* **2013**, 500, 323.
- (11) Schimpf, A. M.; Lounis, S. D.; Runnerstrom, E. L.; Milliron, D. J.; Gamelin, D. R. *J. Am. Chem. Soc.* **2015**, 137, 518.
- (12) Singhal, A.; Achary, S. N.; Tyagi, A. K.; Manna, P. K.; Yusuf, S. M. *Mater. Sci. Engin. B* **2008**, 153, 47.
- (13) Acikgoz, M.; Drahus, M. D.; Ozarowski, A.; van Tol, J.; Weber, S.; Erdem, E. *J. Phys. Condens. Matter* **2014**, 26, 155803.
- (14) Tribollet, J.; Behrends, J.; Lips, K. *EPL (Europhys. Lett.)* **2008**, 84, 20009.
- (15) Heitz, R.; Hoffmann, A.; Broser, I. *Phys. Rev. B* **1992**, 45, 8977.
- (16) George, S.; Pokhrel, S.; Xia, T.; Gilbert, B.; Ji, Z.; Schowalter, M.; Rosenauer, A.; Damoiseaux, R.; Bradley, K. A.; Madler, L.; Nel, A. E. *ACS nano* **2010**, 4, 15.
- (17) Dietl, T.; Ohno, H.; Matsukura, F.; Cibert, J.; Ferrand, D. *Science* **2000**, 287, 1019.
- (18) Sato, K.; Katayama-Yoshida, H. *Jpn J Appl Phys 2* **2001**, 40, L334.

- (19) Kittilstved, K. R.; Liu, W. K.; Gamelin, D. R. *Nature Mater.* **2006**, *5*, 291.
- (20) Wei, X. X.; Song, C.; Geng, K. W.; Zeng, F.; He, B.; Pan, F. *J Phys-Condens Mat* **2006**, *18*, 7471.
- (21) Karmakar, D.; Mandal, S. K.; Kadam, R. M.; Paulose, P. L.; Rajarajan, A. K.; Nath, T. K.; Das, A. K.; Dasgupta, I.; Das, G. P. *Phys. Rev. B* **2007**, *75*, 144404.
- (22) Kolesnik, S.; Dabrowski, B.; Mais, J. *J. Appl. Phys.* **2004**, *95*, 2582.
- (23) Yoon, S. W.; Cho, S. B.; We, S. C.; Yoon, S.; Suh, B. J.; Song, H. K.; Shin, Y. J. *J. Appl. Phys.* **2003**, *93*, 7879.
- (24) Baum, L.; Meyer, M.; Richard, D.; Damonte, L. C.; Mendoza-Zéllis, L. *Hyperfine Interact.* **2008**, *176*, 87.
- (25) Kataoka, T.; Kobayashi, M.; Sakamoto, Y.; Song, G. S.; Fujimori, A.; Chang, F. H.; Lin, H. J.; Huang, D. J.; Chen, C. T.; Ohkochi, T.; Takeda, Y.; Okane, T.; Saitoh, Y.; Yamagami, H.; Tanaka, A.; Mandal, S. K.; Nath, T. K.; Karmakar, D.; Dasgupta, I. *J. Appl. Phys.* **2010**, *107*, 033718.
- (26) McLeod, J. A.; Boukhvalov, D. W.; Zatsopin, D. A.; Green, R. J.; Leedahl, B.; Cui, L.; Kurmaev, E. Z.; Zhidkov, I. S.; Finkelstein, L. D.; Gavrilov, N. V.; Cholakh, S. O.; Moewes, A. *J. Phys. Chem. C* **2014**, *118*, 5336.
- (27) Radovanovic, P.; Gamelin, D. *Phys. Rev. Lett.* **2003**, *91*, 157202.
- (28) Lorenz, M.; Böttcher, R.; Friedländer, S.; Pöppel, A.; Spemann, D.; Grundmann, M. *J. Mater. Chem. C* **2014**, *2*, 4947.
- (29) Walsh, W. M.; Rupp, L. W. *Phys Rev* **1962**, *126*, 952.
- (30) Stoll, S.; Schweiger, A. *Journal of magnetic resonance* **2006**, *178*, 42.
- (31) Meulenkamp, E. A. *J. Phys. Chem. B* **1998**, *102*, 5566.
- (32) Bates, C. H.; White, W. B.; Roy, R. *J. Inorg. Nucl. Chem.* **1968**, *28*, 397.
- (33) Shannon, R. D. *Acta Cryst.* **1976**, *A32*, 751.
- (34) Norberg, N. S.; Gamelin, D. R. *J. Phys. Chem. B* **2005**, *109*, 20810.
- (35) Aasa, R.; Malmstrom, B. G.; Saltman, P.; Vanngard, T. *Biochim Biophys Acta* **1963**, *75*, 203.
- (36) Bou-Abdallah, F.; Chasteen, N. D. *J. Biol. Inorg. Chem.* **2008**, *13*, 15.
- (37) Aasa, R. *J. Chem. Phys.* **1970**, *52*, 3919.

- (38) Bryan, J. D.; Schwartz, D. A.; Gamelin, D. R. *J. Nanosci. Nanotech.* **2005**, *5*, 1472.
- (39) Dagtepe, P.; Chikan, V.; Jasinski, J.; Leppert, V. J. *J. Phys. Chem. C* **2007**, *111*, 14977.
- (40) Sibera, D.; Narkiewicz, U.; Guskos, N.; Zolnierkiewicz, G. *J Phys Conf Ser* **2009**, *146*, 012014.
- (41) Guskos, N.; Glenis, S.; Zolnierkiewicz, G.; Typek, J.; Berczynski, P.; Guskos, A.; Sibera, D.; Narkiewicz, U. *Appl. Phys. Lett.* **2012**, *100*, 122403.

CHAPTER 3

ELECTRON TRAPPING ON Fe^{3+} SITE IN PHOTODOPED ZNO COLLOIDAL NANOCRYSTALS

3.1. Introduction

The introduction of excess charge carriers by either anaerobic band gap excitation in the presence of a hole quencher (photodoping) or chemical reductants has been demonstrated in numerous colloidal semiconductor quantum dots (QDs).^{1,2} The most studied system is *n*-type ZnO QDs.¹⁻⁶ In ZnO, excess electrons can accumulate in the conduction band, which results in the appearance of new spectroscopic features assigned to conduction band electrons (e_{cb}^-) including: **(1)** bleaching of the excitonic transition and photoluminescence, **(2)** a size-tunable intra-band transition in the mid-IR region that is assigned to a localized surface plasmon resonance (LSPR), and **(3)** a signal at $g \sim 1.96$ in the electron paramagnetic resonance (EPR) spectrum.^{3,7,8} All of these spectroscopic features are sensitive to the nanocrystal volume.³ Through careful selection of the hole quencher, photodoping lead to excess electrons in the conduction band of ZnO QDs up to mean values of $>400 e_{cb}^-$ per nanocrystal.⁴

The study of photodoped ZnO QDs has been extended to impurity-doped ZnO QDs^{7,9,10} with the general formula $Zn_{1-x}M_xO$ where $M = Mg^{2+}, Mn^{2+},$ and Co^{2+} . Ochsenbein and co-workers demonstrated in free-standing $Zn_{1-x}Mn_xO$ QDs that the introduction of e_{cb}^- turns on magnetic exchange pathways between isolated Mn^{2+} ions and antiferromagnetically-coupled Mn^{2+} - Mn^{2+} dimers and results in spin-alignment of *all* substitutional Mn^{2+} ions in an external magnetic field.^{10,11} Recent attention has also focused on introducing carriers into oxide-based QDs through aliovalent doping of shallow donors

such as Al³⁺-doped ZnO QDs.¹² Exploiting the spins of e_{cb}^- using both aliovalent *and* magnetic dopants either in a single dopant or multiple dopants has received less attention in ZnO-based QDs, but has been reported recently in (Fe³⁺,Sn⁴⁺) co-doped In₂O₃-based QDs.¹³ Dopants that introduce carriers and magnetic moments into semiconductors has been proven successful for the archetypical ferromagnetic diluted magnetic semiconductor, Mn²⁺-doped GaAs.¹⁴

One promising candidate as an aliovalent and magnetic dopant in ZnO is Fe³⁺. This dopant possesses five unpaired spins, however, the Fe³⁺ donor level is deep in ZnO and therefore does not possess a LSPR in contrast to Al³⁺-doped ZnO.^{12,15} Single crystal Fe³⁺-doped ZnO has been previously demonstrated to have very long spin coherence lifetimes due to very low abundance of nuclear spins making it an attractive material for spin-based electronics and quantum computing.¹⁶ Recently, we reported the synthesis of colloidal Fe-doped ZnO QDs where the Fe-speciation was investigated by EPR spectroscopy.¹⁷ The EPR spectra of the Fe-doped ZnO QDs demonstrated Fe³⁺ occupying multiple sites in ZnO nanocrystals that we identified as substitutional Fe³⁺ at a Zn²⁺ site (Fe_{Zn}³⁺), Fe³⁺ in a pseudo-octahedral interstitial site of the ZnO lattice (Fe_{int}³⁺), and a surface Fe³⁺ site. Herein, we present a systematic spectroscopic study of Fe doped ZnO colloidal nanocrystals as a function of photodoping time at two varied sizes. Using EPR spectroscopy we observe a sequential decrease of the EPR intensities of Fe_{Zn}³⁺ first, followed by Fe_{int}³⁺ in the ZnO nanocrystals with increasing photodoping time. These changes the Fe-speciation are correlated with UV-Vis and mid IR spectroscopy, which provide critical information regarding the presence of conduction band electrons. Our results are consistent with a gradual raising of the Fermi level with increased photodoping time and the Fe_{Zn}^{3+/2+} level

situated deeper than the $\text{Fe}_{\text{int}}^{3+/2+}$ level. The spectroscopic changes with different Fe-doped ZnO nanocrystal size also allows us to estimate the relative positions of the conduction band and the $\text{Fe}_{\text{Zn}}^{3+/2+}$ level.

2.2. Experimental Section

1% of colloidal Fe doped ZnO nanocrystals were prepared using previous method.¹⁷ Briefly, 0.01 cation mol fraction of $\text{Fe}(\text{OAc})_2$ was added to 2.5 mmol of $\text{Zn}(\text{OAc})_2 \cdot 2\text{H}_2\text{O}$ dissolved in 25 mL DMSO. 1.7 equivalents of tetramethylammonium hydroxide was dissolved in 7.7 mL of ethanol was added dropwise into Zn precursor under vigorous magnetic stirring to initiate nucleation and growth. After 5 h of growth, the nanocrystals were precipitated with ethyl acetate, resuspended in heptane and washed with ethanol. The final particle size was controlled by heating the nanocrystal in dodecylamine at 180 °C for different time. For medium size, quantum-confined Fe doped ZnO QDs the heating time was 15min and for larger Fe doped ZnO NCs the heating time was 2h. After reaching the final size, nanocrystals were precipitated and washed with ethanol. The particles were dried under vacuum for 2 h, transferred to the glove box and suspended in degassed hexanes with 5% ethanol as the hole quencher.

Photodoping was performed by placing the sample in an air-tight vial and irradiating with the light from either a 75 W or 1000 W Xe lamp for different times. The particle concentration is controlled to provide appropriate optical densities for both the band gap (pathlength = 0.05 mm) and ligand to metal charge transfer (pathlength = 1 cm). For each charging, the vial was took out from glove box with air tight cap and charged for different time. After each charging, the vial was put back in the glove box and the sample was transferred to the air-tight 1-cm cuvette (1.5 mL), demountable KBr cell with 0.05-

mm pathlength, and air-tight EPR tube (0.4 mL). The band gap absorption, localized surface plasmon resonance (LSPR), LMCT transition and room-temperature EPR were collected within 10 minutes after sample transfer. Electronic absorption spectra were collected using a Varian Cary 50. MIR spectra were collected on a Varian 670 FT spectrometer equipped with a KBr beam splitter and DLaTGS detector. EPR spectra were collected on a Bruker Elexsys E-500 at X-band. Mössbauer spectra were collected in the Mineral Spectroscopy Laboratory at Mount Holyoke College using a WEB Research Co. model WT302 spectrometer and a source of ~ 60 mCi ^{57}Co on 5% Fe-doped ZnO powders dispersed in matrix of sugar.

2.3. Result and Discussion

Figure 3.1A shows room temperature EPR spectra of nominally 1% Fe-doped ZnO nanocrystals dispersed in hexanes before ($t = 0$) and after ($t \leq 1000$ min) irradiation with a 75 W Xe lamp under anaerobic conditions. The sample was made by methods reported previously (see ESI for full experimental details).¹⁷ Based on the band edge absorption at $t = 0$ shown in Figure 3.1B, we estimate the mean particle radius of $\bar{r} = 2.8$ nm (“medium”).¹⁸ The hole quencher used in all photodoping measurements was ethanol, which is expected to yield only 1-10 e_{cb}^- per Fe-doped ZnO QD.⁴ The EPR spectrum at $t = 0$ clearly shows Fe^{3+} occupying two different sites in the ZnO nanocrystals that we have previously identified.¹⁷ With increased photodoping time the $\text{Fe}_{\text{Zn}}^{3+}$ signal decreases in intensity and eventually disappears at $t \approx 380$ min. Over the same charging time, however, the EPR intensity from the $\text{Fe}_{\text{int}}^{3+}$ undergoes minimal change. At $t = 1000$ min, the EPR signals from

both Fe^{3+} species has disappeared. Upon opening the sample to air, the EPR signals from both Fe^{3+} sites recover, but not to the intensities before photodoping (*vide infra*).

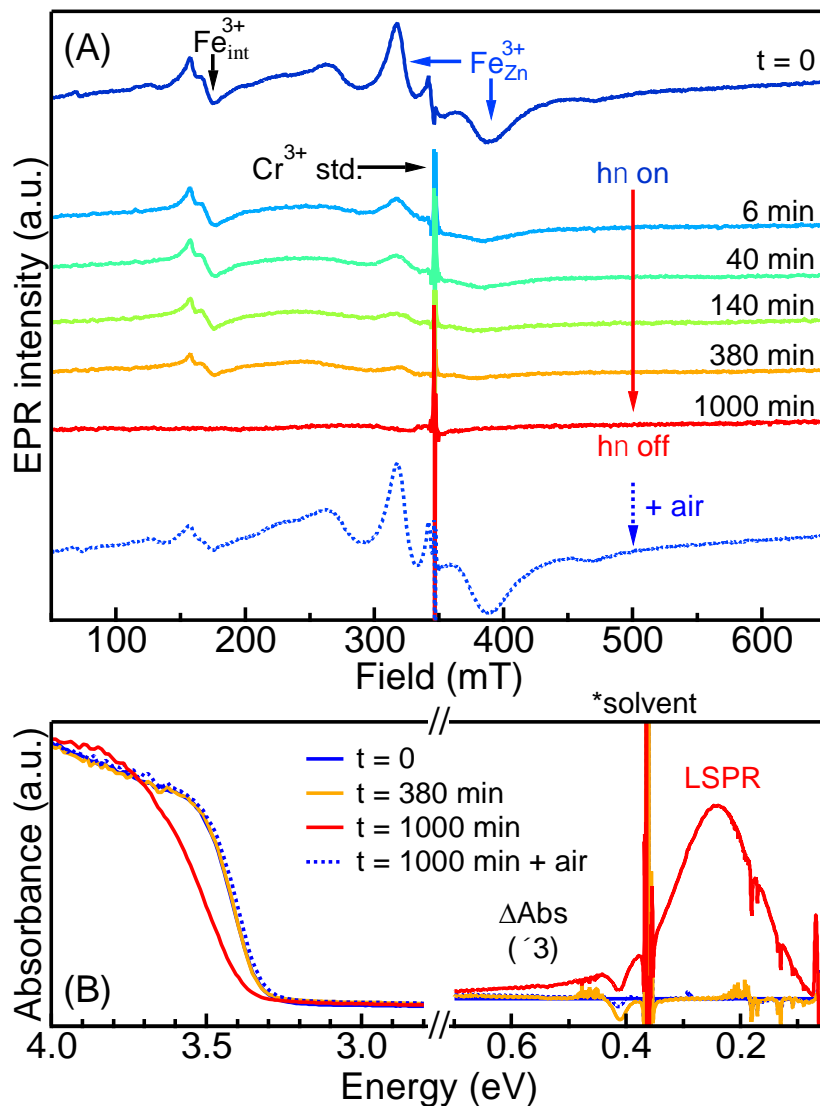


Figure 3.1. Evolution of the (A) EPR and (B) UV-Vis and FTIR spectra of 1% Fe-doped ZnO nanocrystals (medium, $\bar{r} = 2.8$ nm) collected at various photodoping times with a 75 W Xe lamp. The sharp transition in (A) at ~ 350 mT is from Cr^{3+} -doped SrTiO_3 as a frequency standard ($g=1.978$).¹⁹ The FTIR absorption spectra in (B) is presented as the differential absorbance after subtracting the $t = 0$ spectrum (ΔAbs). The ΔAbs values for the IR spectra have been multiplied by a factor of 3 for clarity. Spectra in B were collected in a demountable IR cell with KBr windows with a pathlength of 0.15 mm.

Figure 3.1B shows the absorption spectra of the same samples shown in Figure 3.1A in the UV and IR regions where the ZnO band gap transition and LSPR from n -type

ZnO colloidal nanocrystals are observed, respectively.^{7,12} At $t = 0$, the Fe-doped ZnO QDs do not display any LSPR absorption in the mid-IR as reported previously.¹⁷ In contrast to the gradual changes observed in the $\text{Fe}_{\text{Zn}}^{3+}$ signal by EPR spectroscopy with increasing photodoping time, there are no detectable changes to the ZnO electronic structure such as a blue-shift in the band gap energy or appearance of the LSPR in the mid-IR below $t = 380$ min. At $t = 1000$ min, there is a significant bleach in the ZnO band gap absorption and appearance of the LSPR, which correlates with the disappearance of both Fe^{3+} sites by EPR spectroscopy. While similar to the partial reversibility of the Fe^{3+} EPR signals, the changes to the ZnO electronic structure are fully reversible upon oxidation of the sample by air. There is also a small redshift of the ZnO band-gap transition thus indicating some degree of particle growth during the photodoping experiment. These results indicate that the initial photodoped electrons in ZnO interact strongly with paramagnetic Fe^{3+} sites, but do not possess the spectral signatures expected for e_{cb}^- that are only observed at longer times ($t = 1000$ min). Notably, we do not observe any EPR signal from e_{cb}^- in undoped ZnO, which we attribute to strong coupling between the e_{cb}^- and Fe dopants that likely broadens the signal significantly, similar to previous observations on Co^{2+} - and Mn^{2+} -doped ZnO nanocrystals.⁷ The lack of EPR from e_{cb}^- in pure ZnO also confirms that each nanocrystal in the ensemble has at least one Fe dopant at the 1% nominal doping concentration.

We also performed similar photodoping measurements on larger, non-quantum confined ($\bar{r} \geq 3.2$ nm, “large”) 1% Fe-doped ZnO and observed similar behavior with respect to the disappearance of the Fe^{3+} EPR signals with increasing irradiation time (see Figure 3.2). In contrast to the smaller Fe-doped ZnO data shown in Figure 3.1, an increase in the LSPR transition is observed in the larger nanocrystals before all the Fe^{3+} EPR

intensity disappears. We attribute this result to a decrease in the conduction band potential with increasing size, which results in a smaller driving force for electron transfer from the conduction band to either Fe^{3+} site in the ZnO nanocrystal.

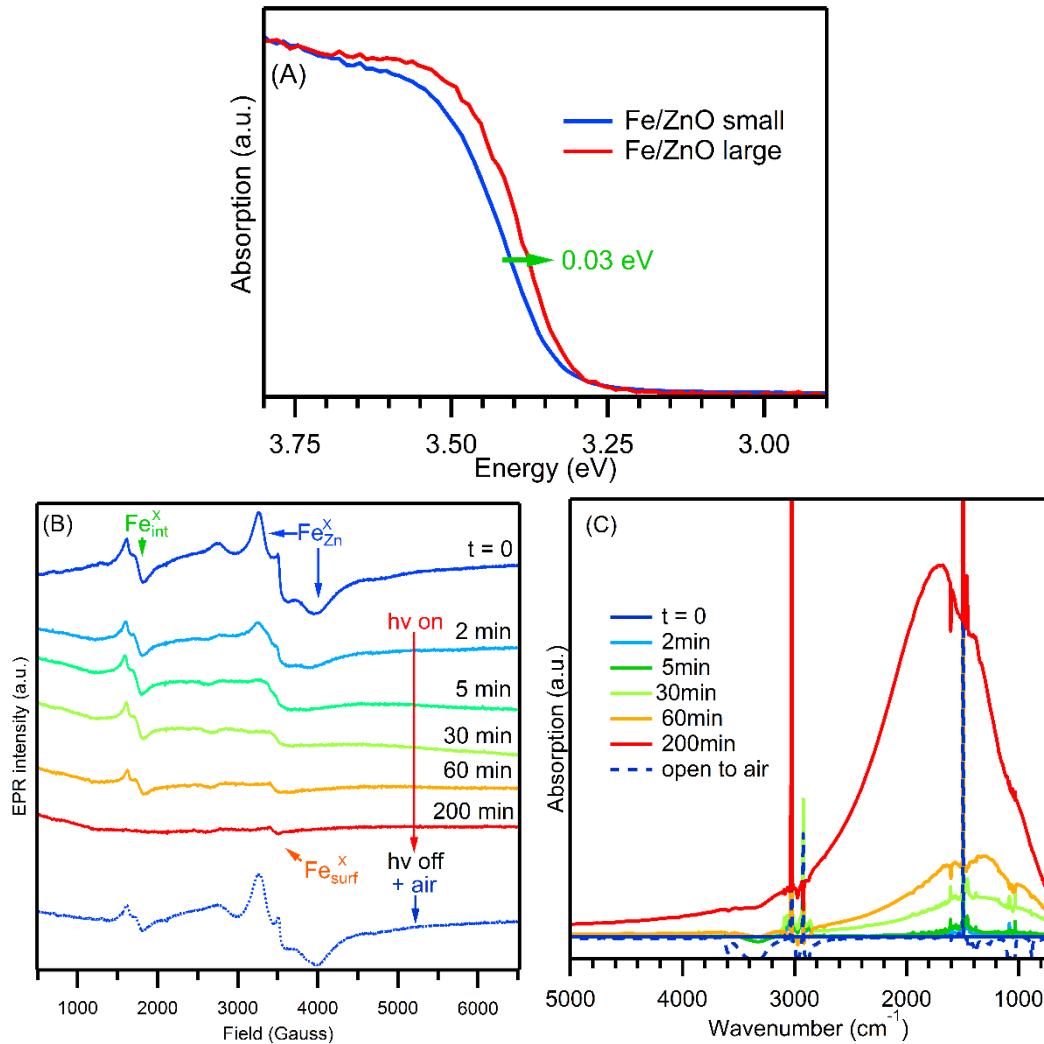


Figure 3.2. (A). Electronic absorption spectra of the band gap transition of nominally 1% Fe-doped ZnO medium (blue) and large (red) colloidal nanocrystals. The energy at half-height is 0.03 eV redshifted in the larger nanocrystals. (B) EPR and (C) MIR spectra of nominally 1% Fe-doped ZnO QDs ($\bar{r} \geq 3.2$ nm) as a function of photodoping with a 1000 W Xe lamp instead of the 75 W Xe lamp used for the smaller QDs shown in Figure 1 of the main text. The appearance of the LSPR in the MIR occurs before all the Fe^{3+} has disappeared by EPR spectroscopy confirming the coexistence of Fe^{3+} and conduction band electrons in these unconfined Fe-doped ZnO QDs. With increasing irradiation times, the LSPR blueshifts in agreement with previous photodoping studies of ZnO QDs.⁴

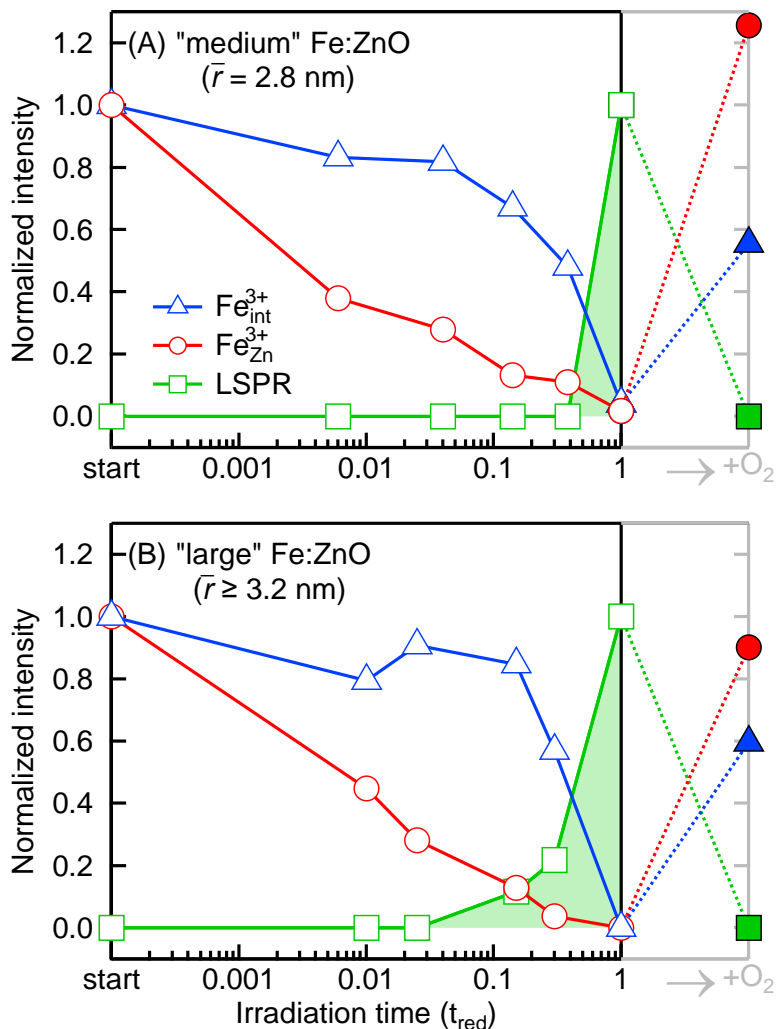


Figure 3.3. Summary of spectroscopic changes of the Fe³⁺ EPR intensities and LSPR intensity of (A) medium ($\bar{r} = 2.8$ nm) and (B) large ($\bar{r} > 3.2$ nm) colloidal 1% Fe-doped ZnO nanocrystals plotted as a function of irradiation time (log scale) and after reoxidation by air (filled symbols on right ordinate). The irradiation time is given on a normalized scale, t_{red} , to account for the difference in lamp power for the two datasets (A = 75 W Xe, B = 1000 W Xe). t_{red} is taken as the time where the EPR intensities of the Fe_{int}³⁺ (triangles) and Fe_{Zn}³⁺ (circles) sites are ~ 0 , which is 1000 min in (a). The intensities given on the y-axes are normalized relative to the EPR intensities of both Fe³⁺ sites at $t = 0$ and the LSPR (squares) at $t = t_{red}$.

The results from Figures 3.1 and Figure 3.2 for the two Fe-doped ZnO samples are summarized in Figure 3.3 where the normalized intensities of the EPR signal of both Fe³⁺

sites and the LSPR intensity from the FTIR spectra are plotted against a normalized irradiation time. The EPR data in Figure 3.3 are normalized against the intensity at $t = 0$, while the LSPR intensity is relative to the intensity at $t = t_{\text{red}}$ where t_{red} is the time where the LSPR is observed and the EPR intensity from all Fe^{3+} sites is 0. Interestingly, we observe a deviation from 100% reversibility after opening the samples to air. The EPR intensity from $\text{Fe}_{\text{Zn}}^{3+}$ dopants increases by $\sim 25\%$ while that of the $\text{Fe}_{\text{int}}^{3+}$ dopants decrease $\sim 45\%$. This difference is accompanied by growth in the particles from $\bar{r} = 2.8$ nm to ≥ 3.2 nm between $t = 0$ and the reoxidation step (see red-shift in absorption after reoxidation in Figure 3.1B). We attribute these changes to the presence of dodecylamine (DDA) ligands on the particle surface, which can facilitate growth via Ostwald ripening. The increase in the EPR signal from $\text{Fe}_{\text{Zn}}^{3+}$ dopants can only occur from conversion of some $\text{Fe}_{\text{int}}^{3+}$ to $\text{Fe}_{\text{Zn}}^{3+}$, while the loss of $\text{Fe}_{\text{int}}^{3+}$ signal can also come from loss due to removal of $\text{Fe}_{\text{int}}^{3+}$ by binding and removal by DDA. Both observations are consistent with our previous model that describes the changes in Fe^{3+} speciation during ZnO nanoparticle growth.¹⁷

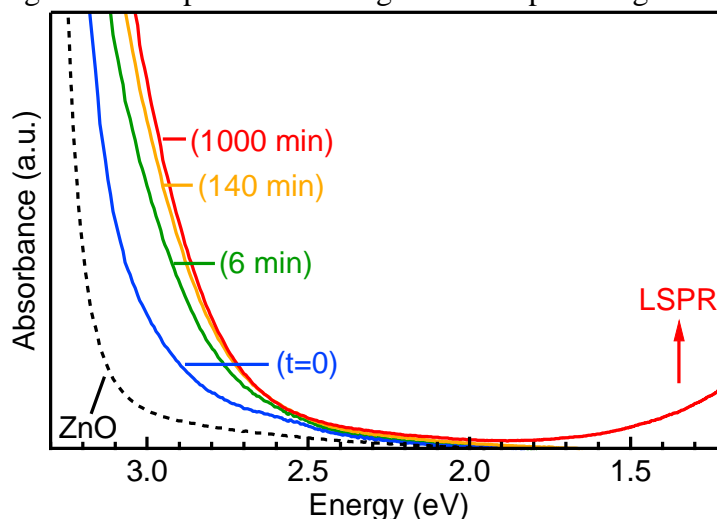


Figure 3.4. Room temperature electronic absorption spectra of the $\bar{r} = 2.8$ nm, 1% Fe-doped ZnO nanocrystals in an air-free 1-cm pathlength cuvette in hexanes as a function of irradiation time.

To reveal possible signatures of Fe^{2+} in the photodoped ZnO, we monitored the intensity and bandshape of the sub-bandgap ligand-to-metal charge transfer transition (LMCT) as shown in Figure 3.4. The spectra shown in Figure 3.4 are the same samples with the same concentration and photodoping as shown in Figure 3.1, but were collected in a 1-cm air-free cuvette to increase the pathlength of the LMCT absorbance by 200 times. We have assigned the sub-bandgap transition at $t = 0$ to ligand-to-metal charge transfer involving all Fe^{3+} dopants in ZnO: substitutional, interstitial and surface. We observe only Fe^{3+} in our as-prepared Fe-doped ZnO QDs by Mössbauer spectroscopy at room temperature with isomer shifts and quadrupole splittings in agreement with the previously reported spectra of Fe^{3+} in bulk ZnO (see Figure 3.5).²⁰ Upon UV-irradiation of the sample, we observe a significant and systematic increase in the LMCT absorption intensity with longer irradiation time. Previous results by Gamelin, et al. demonstrated that the intensity in the region of the band gap transition of undoped ZnO decreases with increased photodoping.^{7,8} We assign the increase in the charge-transfer absorption to ligand-to-metal charge transfer transitions involving Fe^{2+} dopants in photodoped ZnO nanocrystals. Similar intense transitions have been predicted²¹ and observed²² in this same energy range. Attempts to measure the spin-allowed ${}^5\text{E} \rightarrow {}^5\text{T}_2$ transition of substitutional Fe^{2+} in the mid-IR region using concentrated suspensions were unsuccessful due to the strong vibrational overtones of the solvent and surface ligands that dominate the spectra in that energy region.

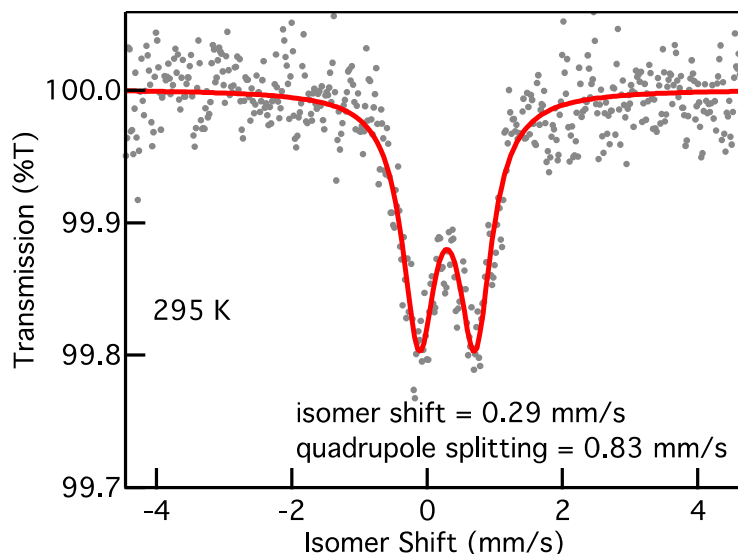


Figure 3.5. Room temperature Mössbauer spectra of 5% Fe-doped ZnO QD powders dispersed in a sugar mixture. The fit to the spectra was performed using a double-Lorentzian lineshape with the widths of the two Lorentzian bands fixed. The experimental isomer shift and quadrupole splitting are in agreement with previously reported room temperature spectra of Fe^{3+} in ZnO .²⁰

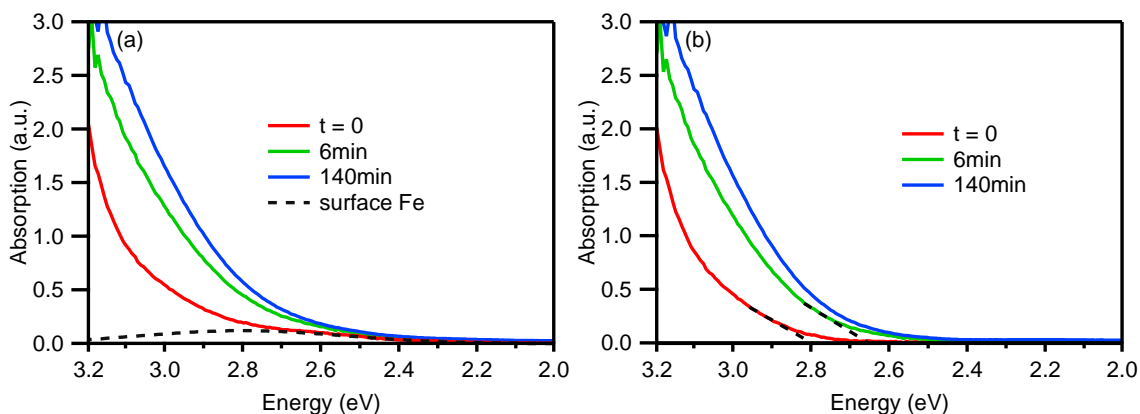


Figure 3.6. (a) Absorption spectra of the LMCT transition of 1% Fe doped ZnO ($\bar{r} = 2.8$ nm) at different photodoping times after subtracting the absorption spectrum of pure ZnO with the same concentration and size. The contribution from surface Fe does not change during photodoping as shown in the EPR spectra in Figure S1. We therefore estimated a broad absorption from this surface Fe^{3+} (shown as a dashed line) and subtracted it from the absorption spectra shown in (a). The resulting corrected absorption spectra is shown in (b). The thresholds of LMCT transitions involving the different Fe species are estimated at $\text{LFe}_{\text{Zn}}^{3+}\text{CT} = 2.8$ eV, $\text{LFe}_{\text{Zn}}^{2+}\text{CT} = 2.65$ eV, respectively.

The intensity of the LMCT transition shown in Figure 3.4 changes significantly at short irradiation times, $t = 6$ min ($t_{\text{red}} = 0.006$), that correlates with the largest decrease in $\text{Fe}_{\text{Zn}}^{3+}$ EPR intensity by $\sim 65\%$ (Figure 3.3A). We tentatively assign this new charge transfer to $\text{Fe}_{\text{Zn}}^{2+}$ LMCT transition with a red-shifted threshold energy compared to Fe^{3+} -doped ZnO ($t = 0$). The threshold energies of the LMCT transitions of $\text{Fe}_{\text{Zn}}^{3+}$ and $\text{Fe}_{\text{Zn}}^{2+}$ in ZnO are estimated at 2.8 eV and 2.65 eV, respectively, based on deconvolution of the CT spectra (see Figure 3.6). The EPR intensities remain relatively unchanged with increased photodoping time until the intensity of $\text{Fe}_{\text{int}}^{3+}$ in EPR started decreasing at $t = 140$ min ($t_{\text{red}} = 0.14$), followed by slightly increased LMCT absorption. At longer photodoping times, the continued increase of the LMCT intensity is difficult to quantify due to the presence of e_{cb}^- , which causes a blue-shift of the ZnO band gap and the appearance of the LSPR at low energies.

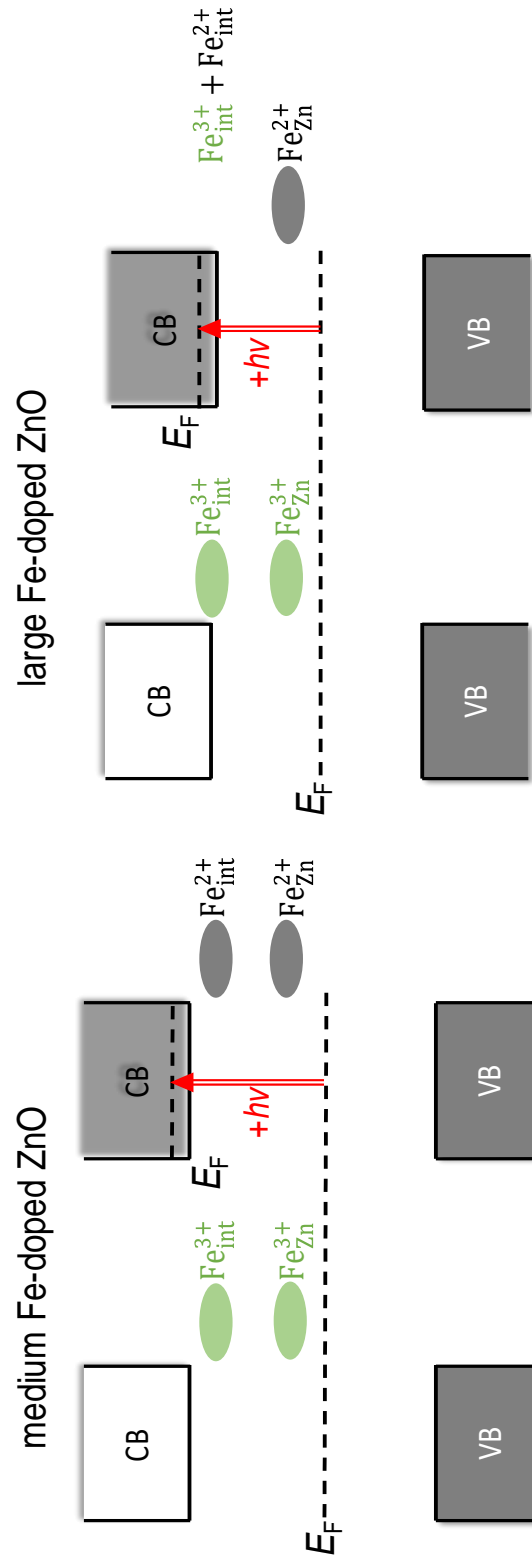


Figure 3.7. Schematic orbital/band diagram for medium and large (no quantum-confinement) Fe-doped ZnO QDs before and after raising the Fermi level by photodoping.

Figure 3.7 shows a schematic band diagram to describe the relevant levels of the ZnO bands and $\text{Fe}^{3+/2+}$ redox potentials. The changes of the EPR spectra and electronic structure of Fe-doped ZnO during photodoping is consistent with Fe^{3+} being reduced to Fe^{2+} , which has a $S = 2$ ground state and is EPR silent. For the $\bar{r} = 2.8$ nm particles, only after all Fe^{3+} in the lattice has been reduced to Fe^{2+} can the photodoped electrons start occupying the conduction band. This scenario therefore places the $\text{Fe}^{3+/2+}$ redox potentials of both substitutional and interstitial sites at energies lower than the weakly quantum-confined ZnO conduction band. However, for the larger particles we observe some LSPR intensity prior to total reduction of the $\text{Fe}_{\text{int}}^{3+}$ EPR intensity. This would place the conduction band potential of the large ZnO and the $\text{Fe}_{\text{int}}^{3+/2+}$ level at similar values.

The EPR spectra of Fe-doped ZnO after photodoping is very different from the behavior of Mn- or Co-doped ZnO after photodoping,^{7,10} which is consistent with Fe^{3+} being reduced to EPR-silent Fe^{2+} . For Mn-doping, the oxidation state of the Mn ion is $2+$ and the EPR spectra broadens and *increases* in integrated area with the introduction of the conduction band electrons.^{10,21} Furthermore, the $\text{Mn}^{2+/+}$ redox level is estimated to lie ~ 1 eV above the bottom of the conduction band.^{21,23} In other words, the $1+$ oxidation state of Mn is inaccessible in Mn^{2+} -doped ZnO by photodoping. The EPR spectra of Co^{2+} -doped ZnO is broadened by fast relaxation at room temperature and therefore typically requires liquid helium temperatures to observe transitions within the $^4\text{A}_2$ ground state. After photodoping, the e_{cb}^- resonance is quenched due to strong $\text{Co}^{2+}-e_{\text{cb}}^-$ exchange. Again, the $\text{Co}^{2+/+}$ redox level is estimated to be above the conduction band of bulk ZnO by only ~ 0.5 eV (potentially accessible in strongly-confined ZnO).²³ The aliovalent nature of Fe^{3+} pulls the $\text{Fe}^{3+/2+}$ level in-between the ZnO band structure. The position of this level must be close

to the conduction band of bulk ZnO and is consistent with previous reports of the coexistence of both Fe²⁺ and Fe³⁺ in *n*-type ZnO materials.^{24,25}

3.4. Conclusions

In summary, we have presented a systematic study of the photodoping of Fe³⁺ doped ZnO colloidal nanocrystals. The introduction of electrons into ZnO via photodoping results in the reduction of both substitutional and interstitial Fe³⁺ dopants prior to observation of the spectral signatures of *n*-type ZnO QDs. This work provides further evidence that photodoping fills trap states first prior to filling conduction band of ZnO and will allow for future studies of these colloidal nanocrystals as model systems to test the theory of charge-transfer ferromagnetism²⁶ in mixed-valent transition metal oxides such as Fe²⁺ and Fe³⁺ in ZnO.

Notes to Chapter 3:

- (1) Haase, M.; Weller, H.; Henglein, A. *J. Phys. Chem.* **1988**, *92*, 482.
- (2) Shim, M.; Guyot-Sionnest, P. *J. Am. Chem. Soc.* **2001**, *123*, 11651.
- (3) Germeau, A.; Roest, A. L.; Vanmaekelbergh, D.; Allan, G.; Delerue, C.; Meulenkamp, E. A. *Phys. Rev. Lett.* **2003**, *90*, 097401.
- (4) Schimpf, A. M.; Gunthardt, C. E.; Rinehart, J. D.; Mayer, J. M.; Gamelin, D. R. *J. Am. Chem. Soc.* **2013**, *135*, 16569.
- (5) Carroll, G. M.; Schimpf, A. M.; Tsui, E. Y.; Gamelin, D. R. *J. Am. Chem. Soc.* **2015**, *137*, 11163.
- (6) Valdez, C. N.; Schimpf, A. M.; Gamelin, D. R.; Mayer, J. M. *J. Am. Chem. Soc.* **2016**, *138*, 1377.
- (7) Liu, W. K.; Whitaker, K. M.; Kittilstved, K. R.; Gamelin, D. R. *J. Am. Chem. Soc.* **2006**, *128*, 3910.
- (8) Liu, W. K.; Whitaker, K. M.; Smith, A. L.; Kittilstved, K. R.; Robinson, B. H.; Gamelin, D. R. *Phys. Rev. Lett.* **2007**, *98*, 186804.
- (9) Cohn, A. W.; Kittilstved, K. R.; Gamelin, D. R. *J. Am. Chem. Soc.* **2012**, *134*, 7937.
- (10) Ochsenein, S. T.; Feng, Y.; Whitaker, K. M.; Badaeva, E.; Liu, W. K.; Li, X. S.; Gamelin, D. R. *Nat. Nanotechnol.* **2009**, *4*, 681.
- (11) Beaulac, R.; Schneider, L.; Archer, P. I.; Bacher, G.; Gamelin, D. R. *Science* **2009**, *325*, 973.
- (12) Buonsanti, R.; Llordes, A.; Aloni, S.; Helms, B. A.; Milliron, D. J. *Nano Lett.* **2011**, *11*, 4706.
- (13) Shanker, G. S.; Tandon, B.; Shibata, T.; Chattopadhyay, S.; Nag, A. *Chem. Mater.* **2015**, *27*, 892.
- (14) Dietl, T.; Ohno, H.; Matsukura, F.; Cibert, J.; Ferrand, D. *Science* **2000**, *287*, 1019.
- (15) Heitz, R.; Hoffmann, A.; Broser, I. *Phys. Rev. B* **1992**, *45*, 8977.
- (16) Tribollet, J.; Behrends, J.; Lips, K. *EPL (Europhysics Letters)* **2008**, *84*, 20009.
- (17) Zhou, D. M.; Kittilstved, K. R. *J. Mater. Chem. C* **2015**, *3*, 4352.
- (18) Meulenkamp, E. A. *J. Phys. Chem. B* **1998**, *102*, 5566.

- (19) Lehuta, K. A.; Kittilstved, K. R. *J. Mat. Chem. A* **2014**, *2*, 6138.
- (20) Ahn, G. Y.; Park, S.-I.; Shim, I.-B.; Kim, C. S. *J. Magn. Magn. Mater.* **2004**, *282*, 166.
- (21) Kittilstved, K. R.; Liu, W. K.; Gamelin, D. R. *Nat. Mater.* **2006**, *5*, 291.
- (22) Bates, C. H.; White, W. B.; Roy, R. *J. Inorg. Nucl. Chem.* **1968**, *28*, 397.
- (23) Blinowski, J.; Kacman, P.; Dietl, T. *Mater. Res. Soc. Symp. Proc.* **2002**, *690*, 109.
- (24) Giuli, G.; Trapananti, A.; Mueller, F.; Bresser, D.; d'Acapito, F.; Passerini, S. *Inorg. Chem.* **2015**, *54*, 9393.
- (25) Samariya, A.; Singhal, R. K.; Kumar, S.; Xing, Y. T.; Alzamora, M.; Dolia, S. N.; Deshpande, U. P.; Shripathi, T.; Saitovitch, E. B. *Mater. Chem. Phys.* **2010**, *123*, 678.
- (26) Coey, J. M. D.; Wongsaprom, K.; Alaria, J.; Venkatesan, M. *J. Phys. D: Appl. Phys.* **2008**, *41*, 134012.

CHAPTER 4

ETCHING AND REGROWTH STRATEGY FOR AL DOPED ZNO NANOCRYSTALS LEADING TO LESS DEFECT AND HIGHER ACTIVATION

4.1. Introduction

Our strategy to make Al³⁺ doped ZnO NCs is modified by a growth-doping approach. Growth-doping strategy has been widely used to synthesize internally doped nanocrystals, such as Cu²⁺:ZnSe,¹ Co²⁺:CdS,² and Al- or In-doped CdSe.³ The typical approach is adding the dopant precursor after NC core has formed. After dopant been absorbed onto the surface of NC core, either isocrystalline or heterocrystalline shell can be grown to encapsulate the dopant.⁴ In this report, instead of making core/shell structure, the initial NC core has been purposely etched by the addition of oleic acid (OA) to a smaller core together with the cationic precursor. Then, the Zn(oleate)₂ precursor and dopant-oleate complex redeposit onto the NC seed. We tentatively call it etching-growth-doping strategy.

4.2. Experimental Section

Materials: All chemicals were used without additional purification. Aluminum chloride (AlCl₃ anhydrous), ferric chloride (FeCl₃ anhydrous), sodium hydroxide (NaOH 98.9%) were purchased from Fisher; zinc chloride (ZnCl₂, 97%), Oleic acid (OA, technical grade, 90%) were purchased from Alfa Aesar; 1-dodecanol (DDOH, 98%), 1-octadecene (ODE, technical grade 90%) were purchased from Acros Organics; and indium(III) acetylacetonate (In(AcAc)₃, 98%) was purchased from Strem Chemicals.

Synthesis of metal oleates. (Zinc oleate and Aluminum oleate): The metal oleates were synthesized following literature methods.⁵ 20 mmol of metal chloride was dissolved in 100 mL of methanol. Then oleic acid (3 equiv for Aluminum, 2 equiv for Zinc) was added. After all the precursor been dissolved, a NaOH solution with 60 mmol (for Aluminum oleate), 40 mmol (for Zinc oleate) in 200 mL of methanol was dropped into metal precursor. The metal oleate precipitated from the solution. The precipitate was washed with methanol 4 to 5 times and dried under vacuum overnight. We also found that anhydrous metal precursor and base were required for making the metal oleates. We tried using metal precursor with bounded water or using tetramethylammonium hydroxide pentahydrate as base,⁶ the Al was failed to doped into ZnO.

Synthesis of AZO and IZO nanocrystals using the etching and regrowth method: In a typical reaction for AZO nanocrystals, Zn(II) oleate (0.63 g, 1 mmol) and 0.2 mol fraction Al(III) oleate (0.17 g, 0.2 mmol) were dissolved in a 50-mL three-necked flask containing 10 mL ODE. The solution was heated at 100 °C under vacuum for 10 min to remove water. The flask was then purged with argon and the solution was heated to 300 °C under an argon flow. A separate solution of 10 mmol DDOH in 2 ml ODE was heated to 150 °C (in air, but we don't need to mention) and rapidly injected into the reaction flask. The reaction temperature dropped to 280 °C and the solution was kept at this temperature for 30 min to allow ZnO precursor nanocrystals to nucleate and grow. For etching and regrowth, a solution of 2 mmol of OA in 2 ml ODE was heated to 150 °C (in air) and rapidly injected into the reaction solution. The temperature was kept at 280 °C for another 30 min.

For IZO nanocrystals synthesis, Zn oleate (1 mmol) and 0.2 mol fraction of $\text{In}(\text{AcAc})_3$ were mixed with 1 mmol Oleic acid in 4 mL ODE. The solution was heated at 100 °C for 30 min for dissolving the In precursor. The rest of reaction followed the etching and regrowth procedure

Alternate syntheses of AZO nanocrystals: For comparison, we also compared the etching and regrowth method against two typical methods using metal oleates to prepare AZO nanocrystals. First, we synthesized AZO nanocrystals in the absence of OA where the initial steps of the etching and regrowth method was followed exactly, however, it was stopped after first 30 min growth step at 280 °C and before the etching step.

For synthesis of AZO with OA present during nucleation, we again followed the etching and regrowth method, but added 2 mmol of OA was to the initial solution of metal oleates in 10 ml ODE before the initial heating steps. This reaction was also stopped after the initial growth step at 280 °C.

4.2. Result and discussion

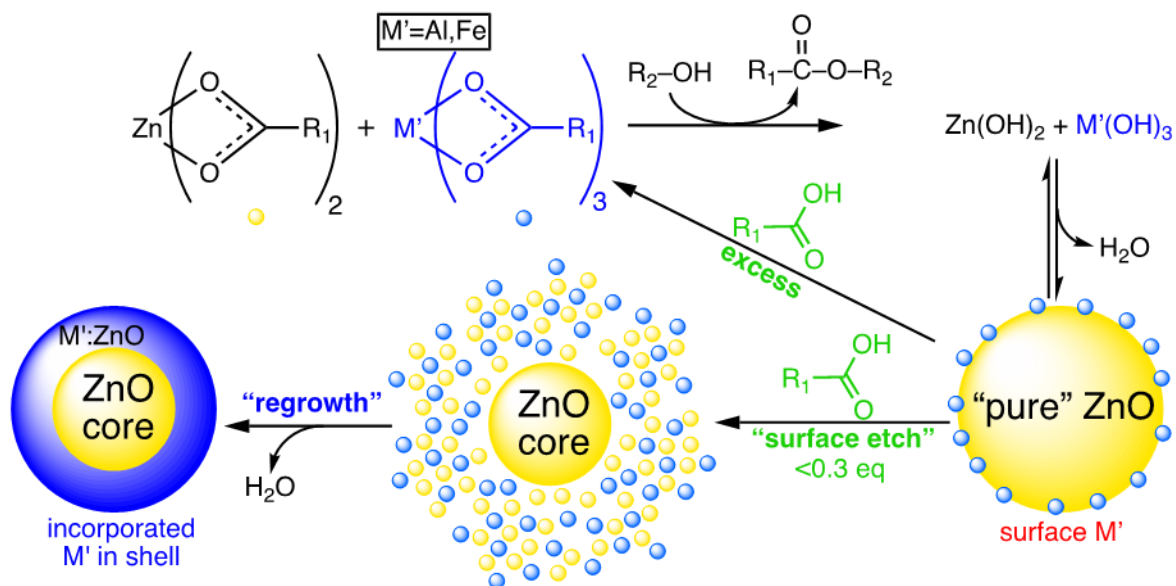


Figure 4.1. Illustration of the molecular mechanism for etching and regrowth strategy.

The proposed mechanism (Figure 4.1) for etching and regrowth method is modified from the irreversible esterification reaction between metal carboxylate and long chain alcohol. ZnO NC forms after the condensation. This alcoholysis reaction has been widely studied for synthesizing a variety of binary and doped oxide nanocrystals including In₂O₃, Fe₂O₃, Mn₃O₄, CoO, and ZnO. Particularly, several groups established successful Al/In/Ga doped ZnO nanocrystals using this method. However, the reaction conditions are extremely important in these synthesis, including hot injection/growth temperature and the chain length of alcohol, the dopant/metal precursor reactivity, the temperature increasing rate. Without separating the nucleation and growth, doping usually requires extra effort on balancing different conditions.

Our etching and regrowth strategy originated from the observation of partial dissolution of the NCs in the present of free acids. During the dissolution, partial ZnO transformed to Zinc carboxylate, and the newly formed metal carboxylate reincorporated into NCs through subsequent esterification and condensation. Dopants carboxylate were

firstly introduced at etching stage together with the oleic acid. This confines the incorporation of the dopants only at regrowth stage, avoiding the high energy of nucleation stage. Further experiments explore that even adding the dopant precursor together with Zinc precursor, the doping still mainly occurs during regrowth stage. Without further noted, in this report, the dopant carboxylate and Zinc carboxylate were introduced together at first step. This could help to simplify the procedure and less consideration of reaction conditions is needed.

For the best solubility of monomers in ODE, the ligand of all the precursor were chosen as oleate. Here, we established a semi-quantitative method to confirm the detailed molecular mechanism. This method combined ZnO band gap absorption with ligand absorption in IR region to monitor the total ZnO NCs formed and cationic precursor left. Figure 4.2. shows the evolution of reaction during each step.

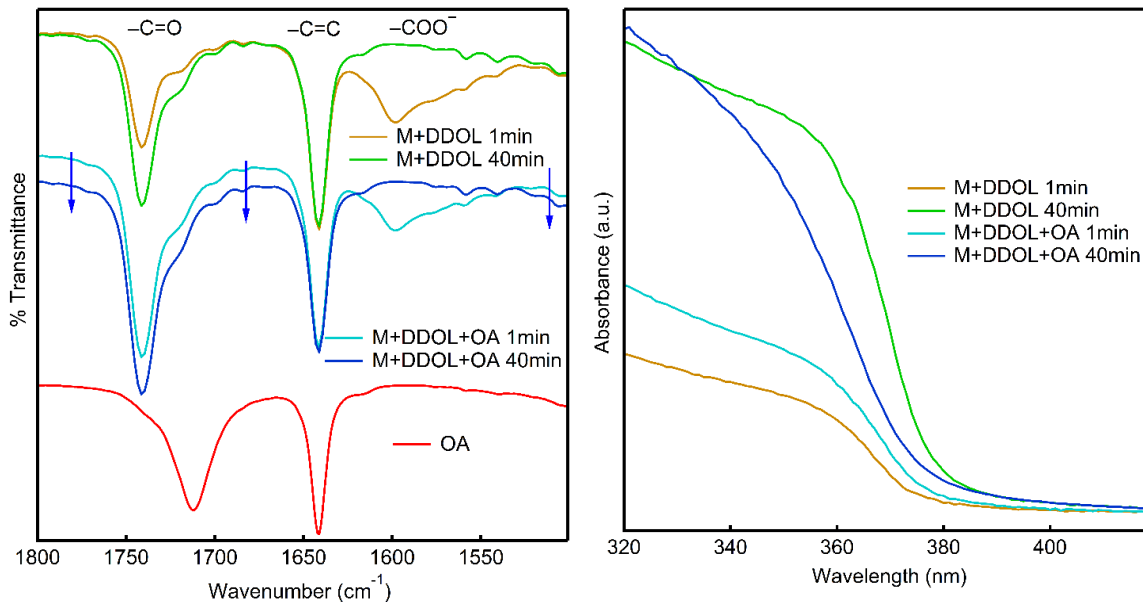


Figure 4.2. Evolution of the FTIR and absorption spectra for Al doped ZnO colloidal solutions at different reaction times.

Aliquots were taken from the reaction mixture during various times and instantly send to monitor the Uv-Vis and FTIR. For FTIR, the original solution was directly injected into 0.05 mm path-length demountable cell with KBr window, while for Uv-vis, the aliquots were diluted 30 times with hexane in 1 cm path-length cuvette. The peak around 1640 cm^{-1} in IR comes from the vibration band of C=C in ODE. Since the path-length for all the FTIR is fixed, and we did observe exact same value for all the sample at 1641 cm^{-1} , so the concentration of organic molecules in the reaction mixture can be read directly based on the peaks intensity. Peak in $1500 - 1620\text{ cm}^{-1}$ correspond to -COO^- asymmetric vibration band from the carboxylate salts. The integration of this band can be referred to the monomers concentration for total Zinc and dopant. Peak centered at 1741 cm^{-1} comes from ester -C=O vibration band, after injected both Zinc and dopant monomers into DDOL solution at 280°C for only 1 min, the ester peak already presented, together with the present of ZnO band gap absorption. After 40 min reaction, all the carboxylate salt disappeared, and the band gap absorption reaches the maximum. The Al(oleate)_3 was added together with Zn(oleate)_2 , but the band gap absorption was close to bulk ZnO (370 nm) after 40 min, indicating almost no Al been doped during the nucleation stage. After adding the double amount of oleic acid (2 mmol) at the same temperature, for only 1 min, the carboxylic acid vibration peak centered at 1712 cm^{-1} already disappeared and the ZnO band gap absorption decreased for more than 60%, together with the replenishment of carboxylate salt and increase of the ester concentration. This indicating that within 1 min, all the oleic acid was consumed to etch the existing ZnO core and the replenishment of monomer already underwent regrowth. This time, still no Al been doped into the lattice. After adding the oleic acid for 40 min, all the monomer consumed to growth, with the increased ester

concentration. The band gap absorption not only reaches the maximum, but also blue shifted, indicating the Al been successfully doped. The presence of the free electrons in the conduction band can also be detected in Figure 4.2. The LSPR transition for electron in conduction band is from 1000 to 5000 cm^{-1} , covers the IR window we used here, so the decreased transmittance background for 40 min is presented.

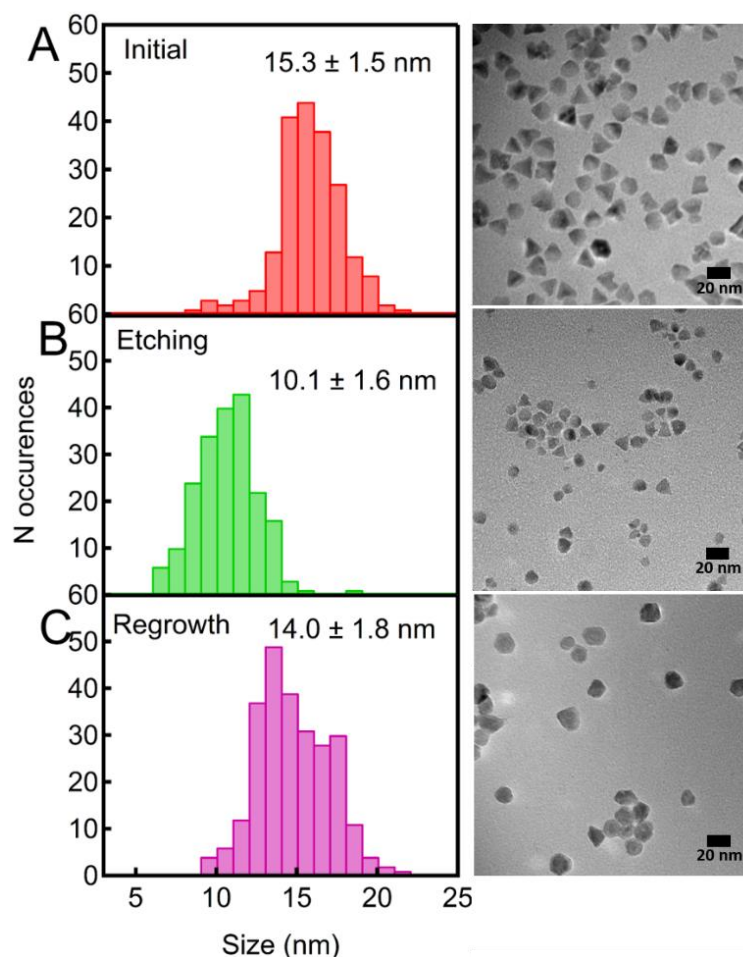


Figure 4.3. TEM image of Al doped ZnO nanocrystals during each step and the size analysis based on the TEM image: (a) Without adding OA and reacted for 40 min. (b) After adding OA to (a) for only 1 min. (c) 40 min reaction after (b).

To further confirm the size and size distribution evolution during the etching and regrowth process, aliquots were taken from the reaction mixture in each step for TEM

collection. The size of initial formed ZnO nanocrystals after 40 min is about 15.3 nm with 1.5 nm size distribution. After adding OA for only 1 min, the ZnO nanocrystals is changed to 10.1 nm with size distribution remain the same. This confirms that all the ZnO nanocrystals are etched by OA at similar speed. After regrowth for 40 min, the size increased to 14.0 nm with comparable size distribution, indicating all the ZnO nanocrystals have grown about 4 nm shell. The Al³⁺ incorporation happened during regrowth, so the distribution of dopant Al³⁺ is across the 4 nm ZnO shell. The shape evolution during the etching and regrowth is similar to pure ZnO nanocrystals when adding free fatty acid.⁷ The shape of initial formed ZnO is pyramids. Depending on the orientation of nanocrystals on the TEM grid, the 2D projection images could appear triangular or hexagonal. The formation of nano-pyramids in the nucleation step are believed due to the dominating growth on high free energy facets under highly kinetic controlled growth condition.⁸ After adding the OA for 1 min, some of the nano-pyramids convert into dots, More dots are forming after regrowth for 40min. The corner and the tip of nano-pyramids are etched by OA, and the regrowth condition become more thermodynamic controlled, so more dot shape is forming.

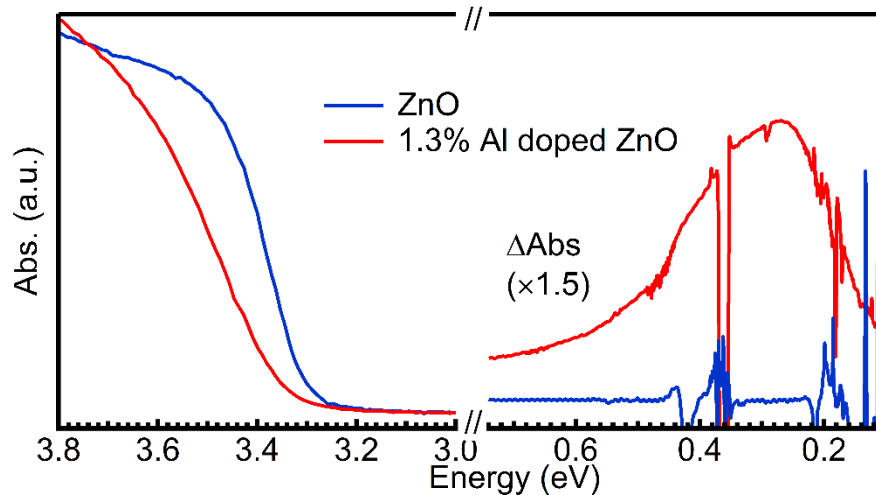


Figure 4.4. Band gap absorption and plasmonic resonance for 1.3% Al doped ZnO nanocrystals

Successful Al doping in ZnO due to the etching and regrowth method has been proved by the blue shift of the band gap and the present of plasmonic absorption, as shown in Fig 4.4. Al^{3+} has been reported as ionized shallow donor. When doped in both bulk and nanocrystal ZnO, Al^{3+} will donate free electrons to conduction band. This causing the blue shift of the band gap and new plasmonic absorption. The energy of the plasmonic absorption peak are related to the electron density in the NCs. In this report, 1.3% Al^{3+} doped ZnO NCs shows plasmonic peak at 0.27 eV. According to the modified Drude Lorentz theory, the free electron density can be estimated as $\sim 9.5 \times 10^{19} \text{ cm}^{-3}$. This is comparable to previous reported 3.5% Al^{3+} doped ZnO and 13.2% Ga doped ZnO NCs. The highly electronic activated dopant (17.9% of Al^{3+}) in this report indicating etching and regrowth method would bring higher activated dopants. Recent report about core/shell approach to dopant incorporation in ZnO nanorod also observed highly electronically active dopants when introduce dopant after the seed forming.⁹

The activation of the dopant is highly dependent on the charge compensation in the nanocrystals. In the n-type extrinsic aliovalent doped metal oxide nanocrystals, the common compensation defects are cation vacancies and oxygen interstitials.¹⁰ The dopant activation or the defect chemistry is dominated by the synthetic procedure. Milliron reported a series of activation with fixed size and doping level for Sn doped In_2O_3 nanocrystals and observed that the surface segregation of tin ions reduces the average activation of the dopant. They suggest that the diffusion of compensating oxygen interstitial atoms increases when tin is situated near the nanocrystal surface.¹¹ In this report, we will present three different synthetic procedures with drastically different activation and use XRD to study the structural differences of the doped nanocrystals in these three different approaches. We are trying to bridge the gap between the synthetic procedure with the structural defect and with the dopant activation. The three different procedures are (A) without adding the OA in the system, (B) adding the OA together with the cationic precursor in nucleation, (C) adding the OA for etching and regrowth.

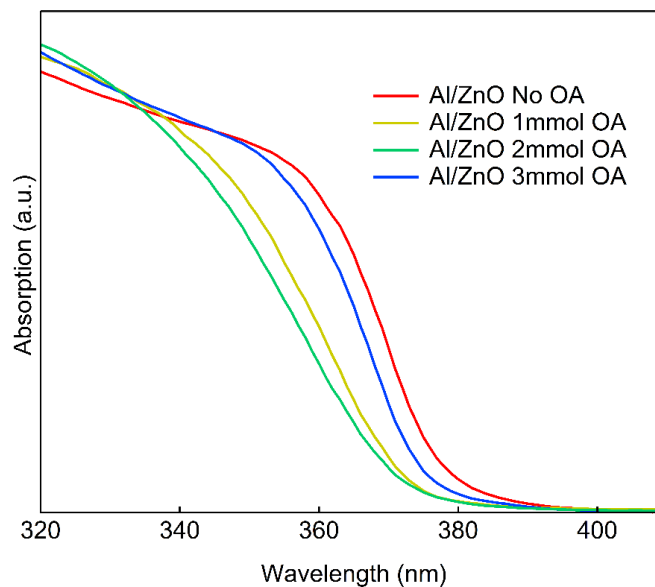


Figure 4.5. The band gap absorption for Al doped ZnO with different amount of OA been added during the synthesis.

OA has been introduced to the synthesis of the Al/In/Ga doped ZnO nanocrystals and Sn doped In₂O₃ nanocrystals.¹²⁻¹⁵ In these reports, OA are introduced together with the metal precursor in the nucleation step to help stabilized the precursor in ODE. Moreover, the ratio of OA/alcohol are also reported to be important during the synthesis.¹³ In fact, we also observed that increasing the amount of OA helps to introduce more conduction band electrons, but when the OA is large enough to dissolve all the ZnO nanocrystal, the regrowth of the ZnO shows the bulk absorption. (see Figure 4.5) Since the metal oxide nanocrystals can be etched by the OA, we believe that in highly kinetic controlled growth condition, the introduction of the dopants and the defect chemistry will be altered by OA.

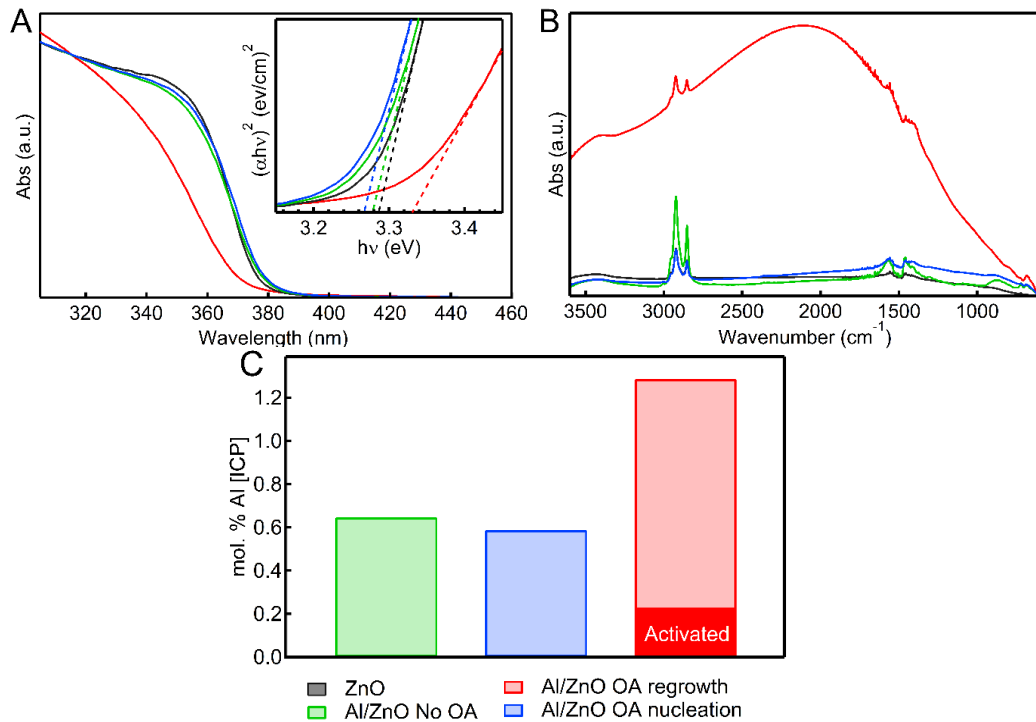


Figure 4.6. (a) Band gap absorption and (b) plasmonic resonance for three different synthetic method of synthesizing Al doped ZnO nanocrystals. The inset shows the respective Tauc plot. (c) Dopant concentration measured by ICP-AES for three different methods. The dark area indicates the amount of activated dopant estimated by the LSPR position.

ICP-AES result shows the total amount of Al^{3+} been doped into ZnO nanocrystals are different. Considering the crystal radius in IV coordination, Al^{3+} (0.53 Å) is much smaller than Zn^{2+} (0.74 Å) in IV coordination compare to other common transition metal dopants, as well as aliovalent dopant such as Ga^{3+} (0.61 Å) and In^{3+} (0.76 Å). Thus doping Al^{3+} is more challenge than doping Ga^{3+} or In^{3+} in ZnO nanocrystals.¹³ Etching and regrowth do introduce more Al^{3+} dopant into the ZnO lattice by avoiding the nucleation, which is highly kinetic controlled condition. On the other hand, without adding OA and introduce OA during nucleation steps show similar band gap absorption (3.27 to 3.29 eV) and no plasmon resonance as bulk ZnO. When adding OA for etching and regrowth, the band gap absorption blue shifted to 3.33 eV and the plasmon resonance centered at 2150 cm^{-1} . This indicate the drastically different carrier concentrations for three different synthetic methods (from 0 to $\sim 9.5 \times 10^{19} \text{ cm}^{-3}$). However, there are still certain amount of Al^{3+} been doped for no OA and OA in nucleation even though no carriers were introduced. And we can calculate that the electronically activated Al^{3+} for no OA and OA in nucleation is 0, while for OA in etching and regrowth is 17.9%.

The dopant activation various due to the different defect chemistry in the ZnO nanocrystals, especially the defects around the dopant. X-ray diffraction (XRD) was applied to explore the structure and defect variation in these different synthetic methods.

As shown in Figure 4.7a, all three methods for Al/ZnO nanocrystals as well as pure ZnO NCs possess the würtzite ZnO phase (JCPDS 36-1451). No other common secondary phases in Al doped ZnO thin film such as such as aluminum oxide (Al_2O_3) or gahnite (ZnAl_2O_4) are observable.^{16,17} The crystallite sizes estimated from Scherrer relationship for all the Al/ZnO and pure ZnO NCs are similar (12 to 15 nm), also close to TEM results.

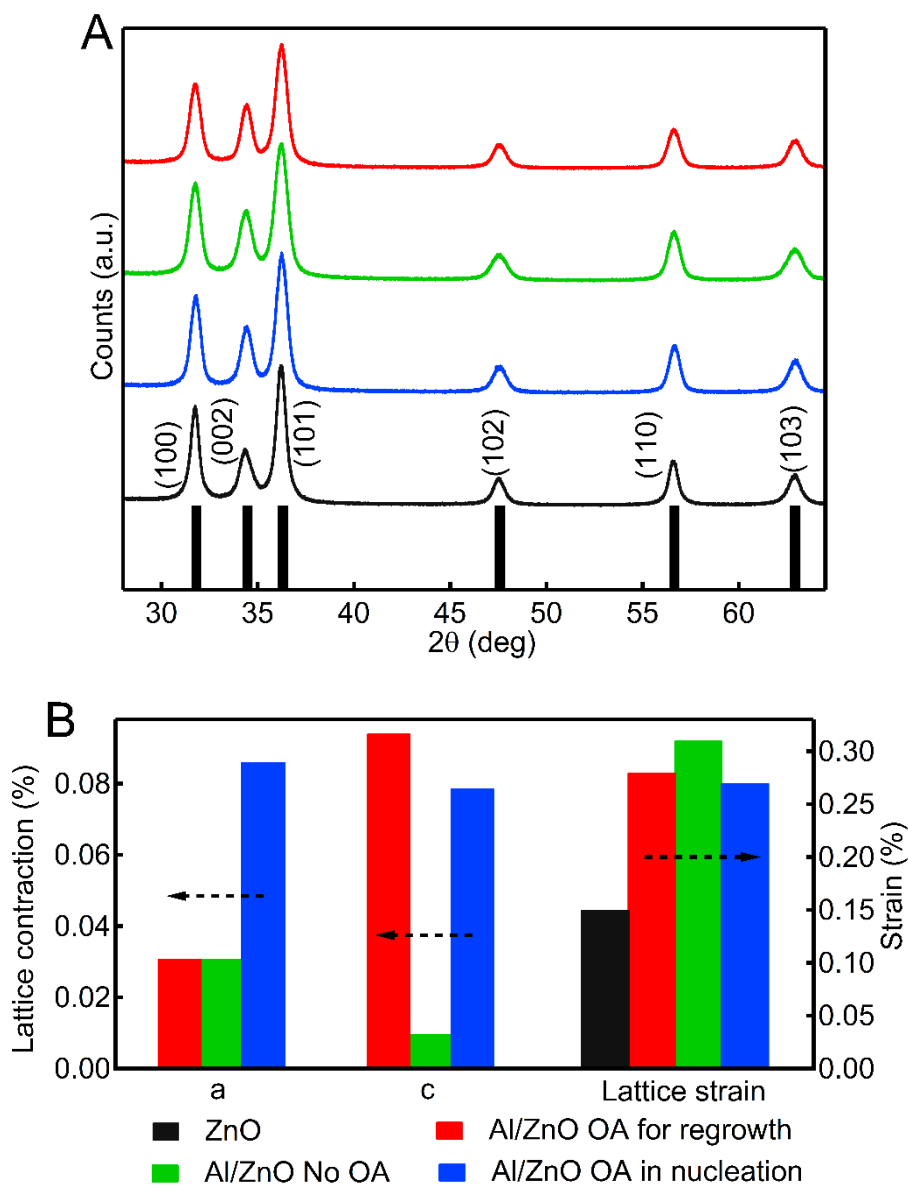


Figure 4.7. (a) XRD patterns of pure ZnO and Al doped ZnO nanocrystals from three different methods. (The reference diffraction pattern of bulk ZnO is listed at the bottom) (b) Lattice contraction for both *a* and *c* axis as well as the lattice strain for pure ZnO and Al doped ZnO nanocrystals. The detailed parameters is predicted from Rietveld analysis using Maud, see Figure 4.8 and Table 4.1.

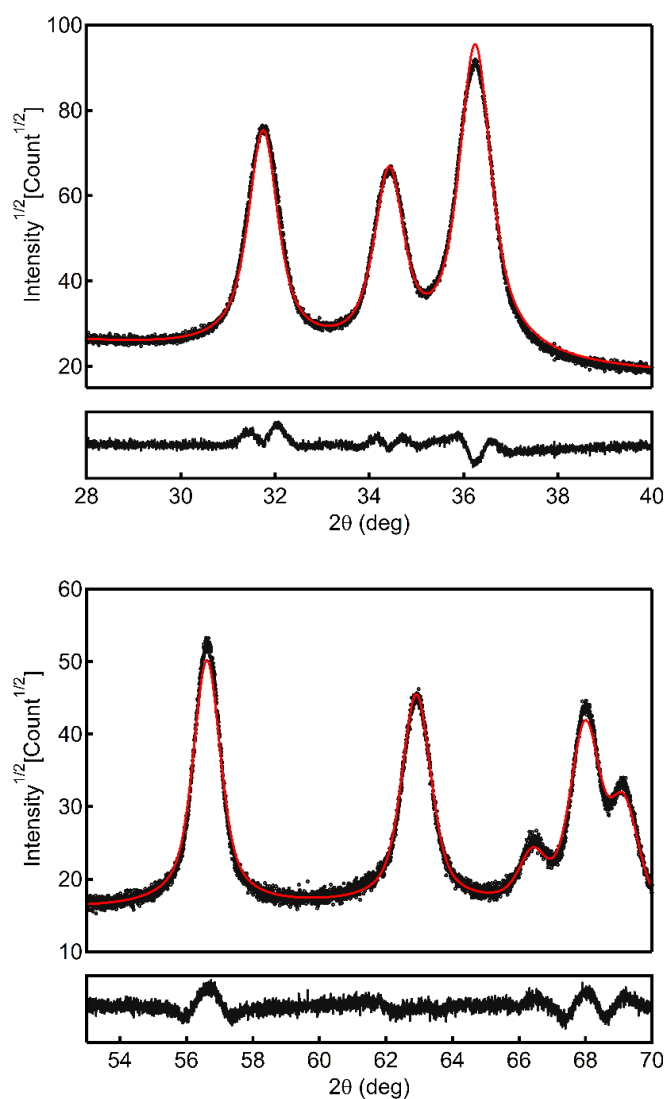


Figure 4.8. Rietveld analysis using Maud. The blank lines refer to the experimental data, the red lines refer to the fitting data. The bottom of each figure shows the difference profile.

sample	$d_{\text{xrd}}(\text{nm})$	$a(\text{\AA})$	$c(\text{\AA})$	lattice strain (%)
pure ZnO	15.1	3.2508	5.2089	0.15
Al/ZnO 2OA in regrowth	13.7	3.2498	5.204	0.28
Al/ZnO no OA	12.2	3.2498	5.2084	0.31
Al/ZnO 2OA in nucleation	14.2	3.248	5.2048	0.27

Table 4-1. The detailed parameters from Rietveld analysis fitting for Al doped ZnO nanocrystals.

Using Rietveld analysis, (see Figure 4.8) we can refine the structural and microstructure parameters (detailed parameters are listed in Table 4.1). Figure 4.7b shows the lattice contraction and lattice strain of three different methods for preparing the Al doped ZnO as well as pure ZnO NCs. Al^{3+} has a smaller ionic radius than Zn^{2+} , once been substituted in ZnO lattice, the lattice parameters will result in contraction. The strain comes from the defects as well as the ionic radius mismatch, so the increased strain for the doped ZnO are also expected. For Al doped ZnO when OA are not introduced, both a and c directions have small lattice contraction. This indicates the Al^{3+} are not successfully substituted in the lattice, while the large lattice strain could come from the surface Al^{3+} or secondary cluster phase which cannot be detected in XRD, since Al^{3+} are still detected by ICP-AES (0.6%). Adding OA during nucleation are typically needed in previous reports.¹²⁻¹⁵ In our study, this do not introduce more Al^{3+} (by ICP) as compared to without adding OA, however, the lattice parameters in both a and c directions show relative large contractions. The contraction of a direction is even larger than the one with highly doped and highly activated Al^{3+} using etching and regrowth method. Adding OA in nucleation shows much higher lattice contraction and lattice strain per Al^{3+} been doped. This indicates the Al^{3+} been successfully substituted in the ZnO lattice using this method. While the larger strain and larger contraction per Al^{3+} also indicates that other defects remain near the dopants, such as Zinc vacancy. Zinc vacancy have been showed in Fe doped ZnO and Al doped ZnO thin film by EXAFS studies.^{18,19} This could also explain the Al^{3+} , even though been successfully substituted, but are not electrical activated using this method. Defects such as interstitial oxygen and Zinc vacancy will compensate the charge introduced by dopant Al^{3+} .¹⁰ As for adding OA as etching and regrowth, the highest amount of Al^{3+} is

been doped, the c direction shows more contraction than a direction, same as previous reports.^{9,12} The relatively low strain per Al^{3+} indicates the smaller amount of defects is been introduced, so the Al^{3+} is highly electronically activated.

The synthetic method is crucial to the conduction band electron density since they will affect the defect chemistry during synthesis due to the difference in kinetic growth conditions. As we discussed previously, without adding the OA, the doping is exposed across the whole nucleation process under a highly kinetic controlled growth condition. This will result in very limited Al^{3+} been substituted. Adding OA during nucleation will alter the nucleation kinetics. As shown in Figure 4.2a, etching ZnO NCs by OA is faster than ZnO NCs formation. With OA remaining in solution, nucleation of ZnO will be blocked since the newly formed nucleate will be dissolved again. the OA works as an inhibitor in the reaction and the growth conditions will be slower compared to without adding OA. Al^{3+} can be successfully substituted but the defect such as Zinc vacancy also been introduced. The etching and regrowth ensure the doping during shell growth, in which the growth kinetic is much slower, thus more Al^{3+} can be substituted without defects present.

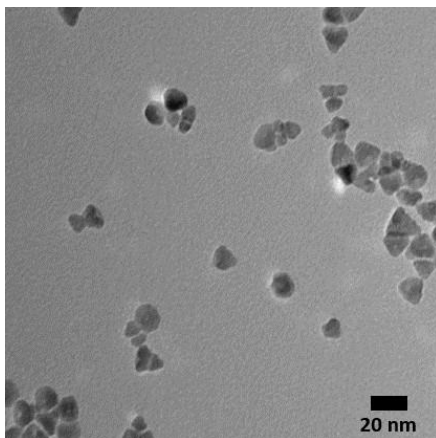
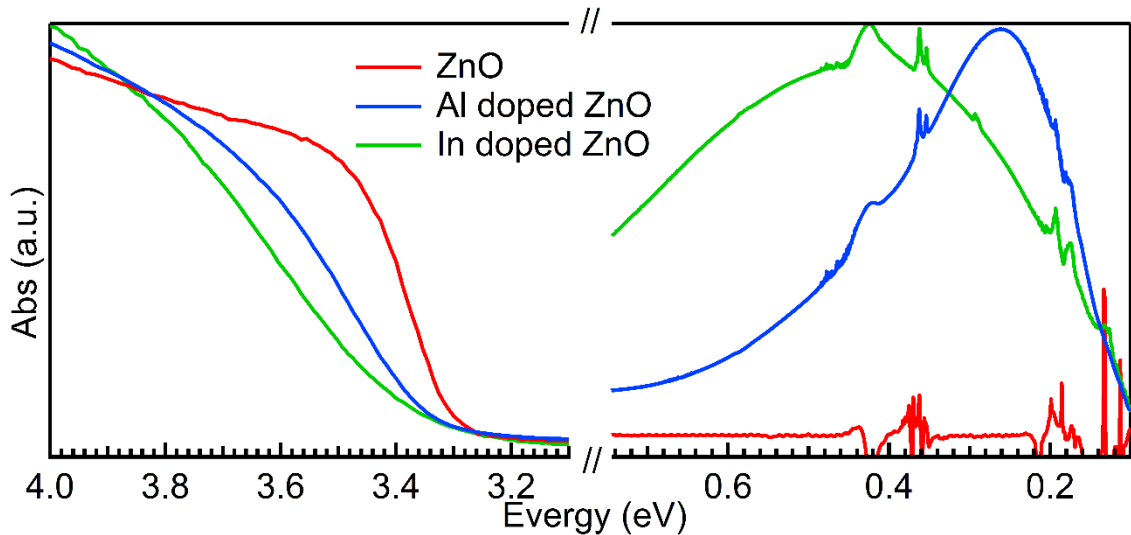


Figure 4.9. TEM for Al doped ZnO nanocrystals with 2 mmol of OA during the nucleation.

The shape of ZnO NCs also supports the difference in growth kinetic conditions for three methods. Nano-pyramid shape are formed under highly kinetic controlled growth condition. Without adding OA, most ZnO NCs shows nano-pyramid shape (Figure 4.3a). Adding OA during nucleation, some of the ZnO NCs shows the dot shape (Figure 4.9). While for etching and regrowth, most of the ZnO NCs shows the dot shape (Figure 4.3c).

In conclusion, we have connected the synthetic procedure to the defect chemistry of Al^{3+} doped ZnO nanocrystals and the free carrier concentrations. Our result shows that adding OA for etching and regrowth is an efficient method to introduce the dopant Al^{3+} in ZnO NCs with minimum amount of the defect due to the slower kinetic growth condition. This lead to a highly electronic activated dopant and large conduction band electron concentration. Similar strategy can also be applied to synthesize the In^{3+} doped ZnO NCs and Sn^{4+} doped In_2O_3 NCs (See Figure 4.10). However, In^{3+} has close crystal radius as Zn^{2+} , as well as Sn^{4+} compared to In^{3+} , doping In^{3+} in ZnO NCs and Sn^{4+} in In_2O_3 NCs are much easier. In fact, OA is not needed for these doping.



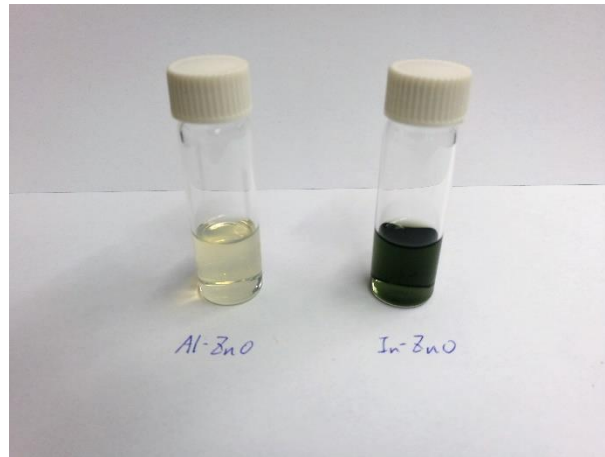


Figure 4.10. Band gap absorption, plasmonic resonance, and picture for Al doped and In doped ZnO nanocrystals.

Note to Chapter 4:

- (1) Pradhan, N.; Goorskey, D.; Thessing, J.; Peng, X. *Journal of the American Chemical Society* **2005**, *127*, 17586.
- (2) Radovanovic, P. V.; Gamelin, D. R. *Journal of the American Chemical Society* **2001**, *123*, 12207.
- (3) Wills, A. W.; Kang, M. S.; Wentz, K. M.; Hayes, S. E.; Sahu, A.; Gladfelter, W. L.; Norris, D. J. *J Mater Chem* **2012**, *22*, 6335.
- (4) Buonsanti, R.; Milliron, D. J. *Chemistry of Materials* **2013**, *25*, 1305.
- (5) Jana, N. R.; Chen, Y. F.; Peng, X. G. *Chemistry of Materials* **2004**, *16*, 3931.
- (6) Liang, X.; Ren, Y.; Bai, S.; Zhang, N.; Dai, X.; Wang, X.; He, H.; Jin, C.; Ye, Z.; Chen, Q.; Chen, L.; Wang, J.; Jin, Y. *Chemistry of Materials* **2014**, *26*, 5169.
- (7) Chen, Y. F.; Kim, M.; Lian, G.; Johnson, M. B.; Peng, X. G. *Journal of the American Chemical Society* **2005**, *127*, 13331.
- (8) Peng, Z. A.; Peng, X. G. *Journal of the American Chemical Society* **2001**, *123*, 1389.
- (9) Mehra, S.; Bergerud, A.; Milliron, D. J.; Chan, E. M.; Salleo, A. *Chemistry of Materials* **2016**, *28*, 3454.
- (10) Lounis, S. D.; Runnerstrom, E. L.; Llordes, A.; Milliron, D. J. *Journal of Physical Chemistry Letters* **2014**, *5*, 1564.
- (11) Lounis, S. D.; Runnerstrom, E. L.; Bergerud, A.; Nordlund, D.; Milliron, D. J. *Journal of the American Chemical Society* **2014**, *136*, 7110.
- (12) Buonsanti, R.; Llordes, A.; Aloni, S.; Helms, B. A.; Milliron, D. J. *Nano Lett* **2011**, *11*, 4706.
- (13) Della Gaspera, E.; Chesman, A. S.; van Embden, J.; Jasieniak, J. J. *ACS nano* **2014**, *8*, 9154.
- (14) Ito, D.; Yokoyama, S.; Zaikova, T.; Masuko, K.; Hutchison, J. E. *ACS nano* **2014**, *8*, 64.
- (15) Jansons, A. W.; Hutchison, J. E. *ACS nano* **2016**, *10*, 6942.
- (16) Bahsi, Z. B.; Aslan, M. H.; Ozer, M.; Oral, A. Y. *Cryst Res Technol* **2009**, *44*, 961.
- (17) Serier, H.; Gaudon, M.; Menetrier, M. *Solid State Sci* **2009**, *11*, 1192.

(18) Park, H. W.; Chung, K. B.; Park, J. S.; Ji, S.; Song, K.; Lim, H.; Jang, M. H. *Ceram Int* **2015**, *41*, 1641.

(19) Yadav, A. K.; Haque, S. M.; Tripathi, S.; Shukla, D.; Ahmed, M. A.; Phase, D. M.; Bandyopadhyay, S.; Jha, S. N.; Bhattacharyya, D. *Rsc Adv* **2016**, *6*, 74982.

CHAPTER 5

CONCLUSION AND OUTLOOK

In this report, we have established a method to study the speciation of the deep donor Fe^{3+} in ZnO NCs. Through photo-charging experiment, we have estimated the relative dopant Fe redox potential, ZnO NCs conduction band potential, and Fermi level. These help to answer the question that why Fe is a deep donor in ZnO NCs and why Fe^{3+} is stable. For shallow donor Al^{3+} in ZnO NCs, we have improved the previous core/shell synthetic doping strategy, and observed that less defect has been introduced (especially the charge compensation defect Zinc vacancy) together with the Al^{3+} doping. Thus, a higher activated Al^{3+} is achieved.

Compared the bulk semiconductor doping with nanocrystal semiconductor doping, the most distinct difference in the band diagram is the Fermi level. As we discussed in Chapter 1, the Fermi level of bulk semiconductor doping can be estimated using Eq 1.1.1. Fermi level increases compared to the intrinsic Fermi level according to the conduction band electron accumulation. However, in the semiconductor nanocrystal, the Fermi level is not determined by the deep donor. In fact, the intrinsic Fermi level varies according to the different synthetic methods, and in return, will determine the dopant oxidation state. This difference can be understood that in bulk semiconductor, the system is isolated. The Fermi level outside the system will not alter the Fermi level inside the semiconductor, thus doping can easily alter the Fermi level. In semiconductor NCs, the surface ratio increases dramatically. When the size of NCs decreases down to few nanometers, more than 50% of the atoms stay on the surface. The nanocrystal is thus fully exposed to the redox reactions happens around the dangling bond at the surface, or in the solution. These redox reactions

are what determine the Fermi level in the semiconductor NCs. Different synthetic methods will result in the different surface defect and composition and further affect the Fermi level.

The Fermi level in semiconductors NCs is affected by the surface redox reactions can also help to understand the band potential difference between the photo-charging and the aliovalent doping. As discussed in Chapter 3, conduction band electrons can be obtained through photo-charging with hole quench present. Schimpf and coworkers have found that the delocalized electrons donating from aliovalent dopant Sn^{4+} in In_2O_3 NCs are much more stable than the conduction band electrons from photo-charging, as seen in Figure 5.1.³ This can be explained that oxygen is not present in the photo-charging experiment, so the system is isolated from the surface redox reaction as bulk semiconductor doping, and the Fermi level will increase as the conduction band electrons increase.¹ In aliovalent doped semiconductor NCs, Fermi level will stay constant for different dopant concentrations.

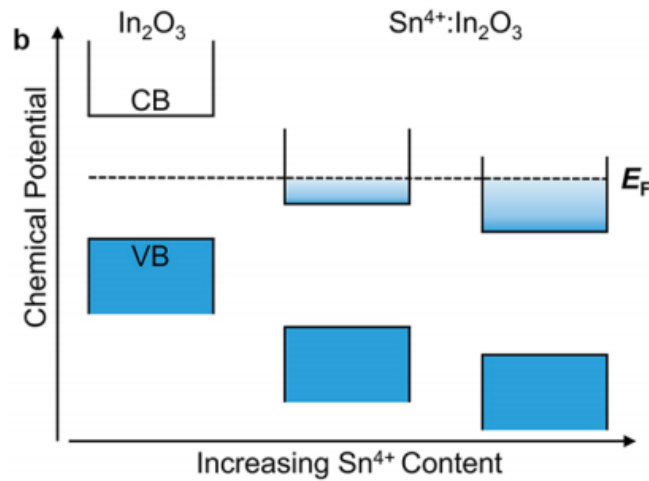


Figure 5.1. Band diagram for the different Sn^{4+} concentration in Sn^{4+} doped In_2O_3 NCs. (Adapted from reference 3)

However, the question remains about the nature of band potential shifting. Another remaining question is that even though the new synthetic doping strategy brings the dopant

activation up to 17%, there are still more than 80% of the aliovalent dopant been charge compensated by other defects. So, where are those defects.

Even though the answer is not resolved, a recent review suggests couple ways to shifting the redox potential of conduction band electron, including adding some positive charges to the surface (H^+ in ZnO NCs or Hg^+ in HgS NCs) or changing the surface dipole. Later, the same group has published a report on using spectroelectrochemical measurement to monitor the redox potentials on CdSe NCs and they observed redox potentials shifting by changing the Cd^{2+} -enriched surface to Se^{2+} -enriched surface. The shift can reach up to 400 meV.²

Inspired by the surface dipole could shifting the band potential, we have provided a hypothesis regarding the nature of stabilized conduction band electrons and the low activated aliovalent dopant.

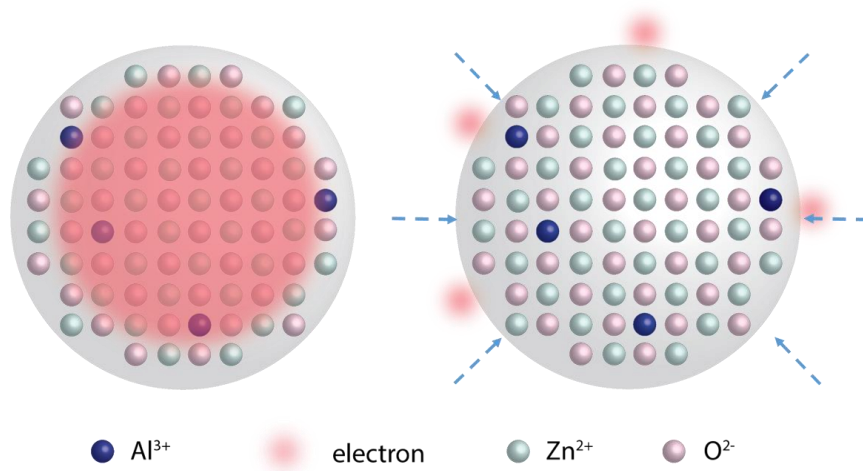


Figure 5.2. Schematic diagram for the aliovalent doping in semiconductor NCs.

As seen in Figure 5.2, the left figure shows the basic picture of aliovalent doping in semiconductor NCs. Due to the relatively higher redox potential of the shallow dopant

compared to the conduction band potential, the electrons will donate to the conduction band, forming delocalized electrons. However, this could not explain the band potential shifting and the low dopant activation. In the right figure, the initial aliovalent dopant does not donate electrons to the conduction band, instead, electrons are donated to the lower energy surface states, including the dangling bond and surface ligand or defect. This will create dipoles towards the core thus lower the band potential. The accumulation of the surface electrons and surface dipoles will finally stabilize the conduction band potential lower than the Fermi level determined by the surface redox reactions. Further aliovalent dopant now can donate electrons to the conduction band.

This hypothesis will not only explain the nature of band potential shifting in aliovalent doping in semiconductor NCs, the model also suggests a unique charge distribution in NCs. The doped NCs are overall charge neutral, however, the ionized dopant is only localized in the core while the NCs also have the surface electrons and delocalized conduction band electrons. Currently, we are investigating the surface charge using electrostatic force microscopy (EFM), and the premier result shows that $\sim 100 e^-$ are estimated on the surface of those aliovalent doped NCs.

Note to Chapter 5:

- (1) Carroll, G. M.; Schimpf, A. M.; Tsui, E. Y.; Gamelin, D. R. *Journal of the American Chemical Society* **2015**, *137*, 11163.
- (2) Carroll, G. M.; Tsui, E. Y.; Brozek, C. K.; Gamelin, D. R. *Chemistry of Materials* **2016**, *28*, 7912.
- (3) Schimpf, A. M.; Knowles, K. E.; Carroll, G. M.; Gamelin, D. R. *Accounts of chemical research* **2015**, *48*, 1929.

BIBLIOGRAPHY

- (1) Peng, X.; Wickham, J.; Alivisatos, A. P. *Journal of the American Chemical Society* **1998**, *120*, 5343.
- (2) Peng, Z. A.; Peng, X. *Journal of the American Chemical Society* **2001**, *123*, 183.
- (3) Peng, X.; Manna, L.; Yang, W.; Wickham, J.; Scher, E.; Kadavanich, A.; Alivisatos, A. P. *Nature* **2000**, *404*, 59.
- (4) Peng, Z. A.; Peng, X. *Journal of the American Chemical Society* **2002**, *124*, 3343.
- (5) Jaramillo, T. F.; Baeck, S. H.; Kleiman-Shwarsstein, A.; Choi, K. S.; Stucky, G. D.; McFarland, E. W. *J Comb Chem* **2005**, *7*, 264.
- (6) Osterloh, F. E. *Chemistry of Materials* **2008**, *20*, 35.
- (7) Santra, P. K.; Kamat, P. V. *Journal of the American Chemical Society* **2012**, *134*, 2508.
- (8) Beaulac, R.; Archer, P. I.; Ochsenein, S. T.; Gamelin, D. R. *Adv Funct Mater* **2008**, *18*, 3873.
- (9) Pradhan, N.; Peng, X. G. *Journal of the American Chemical Society* **2007**, *129*, 3339.
- (10) Norris, D. J.; Efros, A. L.; Erwin, S. C. *Science* **2008**, *319*, 1776.
- (11) Wang, S. Z.; Jarrett, B. R.; Kauzlarich, S. M.; Louie, A. Y. *Journal of the American Chemical Society* **2007**, *129*, 7702.
- (12) Pradhan, N.; Battaglia, D. M.; Liu, Y. C.; Peng, X. G. *Nano Lett* **2007**, *7*, 312.
- (13) Leger, Y.; Besombes, L.; Fernandez-Rossier, J.; Maingault, L.; Mariette, H. *Physical review letters* **2006**, *97*, 107401.
- (14) Fernandez-Rossier, J.; Aguado, R. *Physical review letters* **2007**, *98*, 106805.
- (15) Goryca, M.; Kazimierzuk, T.; Nawrocki, M.; Golnik, A.; Gaj, J. A.; Kossacki, P.; Wojnar, P.; Karczewski, G. *Physical review letters* **2009**, *103*, 087401.
- (16) Baudin, E.; Benjamin, E.; Lemaitre, A.; Krebs, O. *Physical review letters* **2011**, *107*, 197402.
- (17) Wang, F.; Banerjee, D.; Liu, Y.; Chen, X.; Liu, X. *The Analyst* **2010**, *135*, 1839.

- (18) Idris, N. M.; Gnanasammandhan, M. K.; Zhang, J.; Ho, P. C.; Mahendran, R.; Zhang, Y. *Nature medicine* **2012**, *18*, 1580.
- (19) Chen, G.; Qiu, H.; Prasad, P. N.; Chen, X. *Chemical reviews* **2014**, *114*, 5161.
- (20) Yang, Y.; Shao, Q.; Deng, R.; Wang, C.; Teng, X.; Cheng, K.; Cheng, Z.; Huang, L.; Liu, Z.; Liu, X.; Xing, B. *Angewandte Chemie* **2012**, *51*, 3125.
- (21) Anker, J. N.; Hall, W. P.; Lyandres, O.; Shah, N. C.; Zhao, J.; Van Duyne, R. P. *Nat Mater* **2008**, *7*, 442.
- (22) Zhou, Z. G.; Kong, B.; Yu, C.; Shi, X. Y.; Wang, M. W.; Liu, W.; Sun, Y. A.; Zhang, Y. J.; Yang, H.; Yang, S. P. *Sci Rep-Uk* **2014**, *4*.
- (23) Li, W. W.; Chen, X. Y. *Nanomedicine-Uk* **2015**, *10*, 299.
- (24) Abb, M.; Wang, Y. D.; Papasimakis, N.; de Groot, C. H.; Muskens, O. L. *Nano Lett* **2014**, *14*, 346.
- (25) Ghosh, S.; Saha, M.; Ashok, V. D.; Dalal, B.; De, S. K. *J Phys Chem C* **2015**, *119*, 1180.
- (26) Yockell-Lelievre, H.; Lussier, F.; Masson, J. F. *J Phys Chem C* **2015**, *119*, 28577.
- (27) Babicheva, V. E.; Boltasseva, A.; Lavrinenko, A. V. *Nanophotonics-Berlin* **2015**, *4*, 165.
- (28) Liu, M.; Qiu, X.; Miyauchi, M.; Hashimoto, K. *Journal of the American Chemical Society* **2013**, *135*, 10064.
- (29) Dalpian, G. M.; Chelikowsky, J. R. *Physical review letters* **2006**, *96*, 226802.
- (30) Erwin, S. C.; Zu, L.; Haftel, M. I.; Efros, A. L.; Kennedy, T. A.; Norris, D. J. *Nature* **2005**, *436*, 91.
- (31) Kittilstved, K. R.; Liu, W. K.; Gamelin, D. R. *Nat Mater* **2006**, *5*, 291.
- (32) Ochsenein, S. T.; Feng, Y.; Whitaker, K. M.; Badaeva, E.; Liu, W. K.; Li, X.; Gamelin, D. R. *Nature nanotechnology* **2009**, *4*, 681.
- (33) Ochsenein, S. T.; Gamelin, D. R. *Nature nanotechnology* **2011**, *6*, 112.
- (34) Kobak, J.; Smolenski, T.; Goryca, M.; Papaj, M.; Gietka, K.; Bogucki, A.; Koperski, M.; Rousset, J. G.; Suffczynski, J.; Janik, E.; Nawrocki, M.; Golnik, A.; Kossacki, P.; Pacuski, W. *Nature communications* **2014**, *5*, 3191.
- (35) Tribollet, J.; Behrends, J.; Lips, K. *Epl-Europhys Lett* **2008**, *84*.

- (36) Karmakar, D.; Mandal, S. K.; Kadam, R. M.; Paulose, P. L.; Rajarajan, A. K.; Nath, T. K.; Das, A. K.; Dasgupta, I.; Das, G. P. *Phys Rev B* **2007**, *75*.
- (37) Baum, L.; Meyer, M.; Richard, D.; Damonte, L. C.; Mendoza-Zelis, L. *Hyperfine Interact* **2007**, *176*, 87.
- (38) Kataoka, T.; Kobayashi, M.; Sakamoto, Y.; Song, G. S.; Fujimori, A.; Chang, F. H.; Lin, H. J.; Huang, D. J.; Chen, C. T.; Ohkochi, T.; Takeda, Y.; Okane, T.; Saitoh, Y.; Yamagami, H.; Tanaka, A.; Mandal, S. K.; Nath, T. K.; Karmakar, D.; Dasgupta, I. *J Appl Phys* **2010**, *107*.
- (39) McLeod, J. A.; Boukhvalov, D. W.; Zatsopin, D. A.; Green, R. J.; Leedahl, B.; Cui, L.; Kurmaev, E. Z.; Zhidkov, I. S.; Finkelstein, L. D.; Gavrilov, N. V.; Cholakh, S. O.; Moewes, A. *J Phys Chem C* **2014**, *118*, 5336.
- (40) Jorgensen, C. K. *Mol Phys* **1963**, *6*, 43.
- (41) Kelly, K. L.; Coronado, E.; Zhao, L. L.; Schatz, G. C. *J Phys Chem B* **2003**, *107*, 668.
- (42) Link, S.; El-Sayed, M. A. *Annual review of physical chemistry* **2003**, *54*, 331.
- (43) Liu, Q.; Sun, C.; He, Q.; Liu, D.; Khalil, A.; Xiang, T.; Wu, Z.; Wang, J.; Song, L. *Chemical communications* **2015**, *51*, 10054.
- (44) Chen, H.; Kou, X.; Yang, Z.; Ni, W.; Wang, J. *Langmuir : the ACS journal of surfaces and colloids* **2008**, *24*, 5233.
- (45) Nehl, C. L.; Liao, H.; Hafner, J. H. *Nano Lett* **2006**, *6*, 683.
- (46) Wiley, B. J.; Chen, Y.; McLellan, J. M.; Xiong, Y.; Li, Z. Y.; Ginger, D.; Xia, Y. *Nano Lett* **2007**, *7*, 1032.
- (47) Luther, J. M.; Jain, P. K.; Ewers, T.; Alivisatos, A. P. *Nat Mater* **2011**, *10*, 361.
- (48) Agrawal, A. J., R. Milliron, D. *Annu. Rev. Mater. Res* **2017**, *47*.
- (49) Runnerstrom, E. L.; Bergerud, A.; Agrawal, A.; Johns, R. W.; Dahlman, C. J.; Singh, A.; Selbach, S. M.; Milliron, D. J. *Nano Lett* **2016**, *16*, 3390.
- (50) Lounis, S. D.; Runnerstrom, E. L.; Llordes, A.; Milliron, D. J. *The journal of physical chemistry letters* **2014**, *5*, 1564.
- (51) Gordon, T. R.; Paik, T.; Klein, D. R.; Naik, G. V.; Caglayan, H.; Boltasseva, A.; Murray, C. B. *Nano Lett* **2013**, *13*, 2857.
- (52) Greenberg, B. L.; Ganguly, S.; Held, J. T.; Kramer, N. J.; Mkhoyan, K. A.; Aydil, E. S.; Kortshagen, U. R. *Nano Lett* **2015**, *15*, 8162.

- (53) Schimpf, A. M.; Gunthardt, C. E.; Rinehart, J. D.; Mayer, J. M.; Gamelin, D. R. *Journal of the American Chemical Society* **2013**, *135*, 16569.
- (54) Buonsanti, R.; Llodes, A.; Aloni, S.; Helms, B. A.; Milliron, D. J. *Nano Lett* **2011**, *11*, 4706.
- (55) Garcia, G.; Buonsanti, R.; Runnerstrom, E. L.; Mendelsberg, R. J.; Llodes, A.; Anders, A.; Richardson, T. J.; Milliron, D. J. *Nano Lett* **2011**, *11*, 4415.
- (56) Kim, J.; Agrawal, A.; Krieg, F.; Bergerud, A.; Milliron, D. J. *Nano Lett* **2016**, *16*, 3879.
- (57) Runnerstrom, E. L.; Llodes, A.; Lounis, S. D.; Milliron, D. J. *Chemical communications* **2014**, *50*, 10555.
- (58) Llodes, A.; Garcia, G.; Gazquez, J.; Milliron, D. J. *Nature* **2013**, *500*, 323.
- (59) Buonsanti, R.; Milliron, D. J. *Chemistry of Materials* **2013**, *25*, 1305.
- (60) Schimpf, A. M.; Ochsenbein, S. T.; Buonsanti, R.; Milliron, D. J.; Gamelin, D. R. *Chemical communications* **2012**, *48*, 9352.
- (61) Lounis, S. D.; Runnerstrom, E. L.; Bergerud, A.; Nordlund, D.; Milliron, D. J. *Journal of the American Chemical Society* **2014**, *136*, 7110.
- (62) Agoston, P.; Erhart, P.; Klein, A.; Albe, K. *Journal of physics. Condensed matter : an Institute of Physics journal* **2009**, *21*, 455801.
- (63) Hwang, J. *Solid State Ionics* **2000**, *129*, 135.
- (64) Beaulac, R.; Schneider, L.; Archer, P. I.; Bacher, G.; Gamelin, D. R. *Science* **2009**, *325*, 973.
- (65) Ochsenbein, S. T.; Gamelin, D. R. *Nat Nanotechnol* **2011**, *6*, 111.
- (66) Ochsenbein, S. T.; Feng, Y.; Whitaker, K. M.; Badaeva, E.; Liu, W. K.; Li, X. S.; Gamelin, D. R. *Nat Nanotechnol* **2009**, *4*, 681.
- (67) Beaulac, R.; Archer, P. I.; van Rijssel, J.; Meijerink, A.; Gamelin, D. R. *Nano Lett.* **2008**, *8*, 2949.
- (68) Santra, P. K.; Kamat, P. V. *J. Am. Chem. Soc.* **2012**, *134*, 2508.
- (69) Schwartz, D. A.; Norberg, N. S.; Nguyen, Q. P.; Parker, J. M.; Gamelin, D. R. *J. Am. Chem. Soc.* **2003**, *125*, 13205.
- (70) Norberg, N. S.; Kittilstved, K. R.; Amonette, J. E.; Kukkadapu, R. K.; Schwartz, D. A.; Gamelin, D. R. *J. Am. Chem. Soc.* **2004**, *126*, 9387.

- (71) Radovanovic, P. V.; Norberg, N. S.; McNally, K. E.; Gamelin, D. R. *J. Am. Chem. Soc.* **2002**, *124*, 15192.
- (72) Schimpf, A. M.; Ochsenbein, S. T.; Buonsanti, R.; Milliron, D. J.; Gamelin, D. R. *Chemical communications* **2012**, *48*, 9352.
- (73) Schimpf, A. M.; Lounis, S. D.; Runnerstrom, E. L.; Milliron, D. J.; Gamelin, D. R. *J. Am. Chem. Soc.* **2015**, *137*, 518.
- (74) Singhal, A.; Achary, S. N.; Tyagi, A. K.; Manna, P. K.; Yusuf, S. M. *Mater. Sci. Engin. B* **2008**, *153*, 47.
- (75) Acikgoz, M.; Drahus, M. D.; Ozarowski, A.; van Tol, J.; Weber, S.; Erdem, E. *J. Phys. Condens. Matter* **2014**, *26*, 155803.
- (76) Tribollet, J.; Behrends, J.; Lips, K. *EPL (Europhys. Lett.)* **2008**, *84*, 20009.
- (77) Heitz, R.; Hoffmann, A.; Broser, I. *Phys. Rev. B* **1992**, *45*, 8977.
- (78) George, S.; Pokhrel, S.; Xia, T.; Gilbert, B.; Ji, Z.; Schowalter, M.; Rosenauer, A.; Damoiseaux, R.; Bradley, K. A.; Madler, L.; Nel, A. E. *ACS nano* **2010**, *4*, 15.
- (79) Dietl, T.; Ohno, H.; Matsukura, F.; Cibert, J.; Ferrand, D. *Science* **2000**, *287*, 1019.
- (80) Sato, K.; Katayama-Yoshida, H. *Jpn J Appl Phys 2* **2001**, *40*, L334.
- (81) Kittilstved, K. R.; Liu, W. K.; Gamelin, D. R. *Nature Mater.* **2006**, *5*, 291.
- (82) Wei, X. X.; Song, C.; Geng, K. W.; Zeng, F.; He, B.; Pan, F. *J Phys-Condens Mat* **2006**, *18*, 7471.
- (83) Karmakar, D.; Mandal, S. K.; Kadam, R. M.; Paulose, P. L.; Rajarajan, A. K.; Nath, T. K.; Das, A. K.; Dasgupta, I.; Das, G. P. *Phys. Rev. B* **2007**, *75*, 144404.
- (84) Kolesnik, S.; Dabrowski, B.; Mais, J. *J. Appl. Phys.* **2004**, *95*, 2582.
- (85) Yoon, S. W.; Cho, S. B.; We, S. C.; Yoon, S.; Suh, B. J.; Song, H. K.; Shin, Y. J. *J. Appl. Phys.* **2003**, *93*, 7879.
- (86) Baum, L.; Meyer, M.; Richard, D.; Damonte, L. C.; Mendoza-Zélis, L. *Hyperfine Interact.* **2008**, *176*, 87.
- (87) Kataoka, T.; Kobayashi, M.; Sakamoto, Y.; Song, G. S.; Fujimori, A.; Chang, F. H.; Lin, H. J.; Huang, D. J.; Chen, C. T.; Ohkochi, T.; Takeda, Y.; Okane, T.; Saitoh, Y.; Yamagami, H.; Tanaka, A.; Mandal, S. K.; Nath, T. K.; Karmakar, D.; Dasgupta, I. *J. Appl. Phys.* **2010**, *107*, 033718.

- (88) McLeod, J. A.; Boukhvalov, D. W.; Zatsepin, D. A.; Green, R. J.; Leedahl, B.; Cui, L.; Kurmaev, E. Z.; Zhidkov, I. S.; Finkelstein, L. D.; Gavrilov, N. V.; Cholakh, S. O.; Moewes, A. *J. Phys. Chem. C* **2014**, *118*, 5336.
- (89) Radovanovic, P.; Gamelin, D. *Phys. Rev. Lett.* **2003**, *91*, 157202.
- (90) Lorenz, M.; Böttcher, R.; Friedländer, S.; Pöppel, A.; Spemann, D.; Grundmann, M. *J. Mater. Chem. C* **2014**, *2*, 4947.
- (91) Walsh, W. M.; Rupp, L. W. *Phys Rev* **1962**, *126*, 952.
- (92) Stoll, S.; Schweiger, A. *Journal of magnetic resonance* **2006**, *178*, 42.
- (93) Meulenkamp, E. A. *J. Phys. Chem. B* **1998**, *102*, 5566.
- (94) Bates, C. H.; White, W. B.; Roy, R. *J. Inorg. Nucl. Chem.* **1968**, *28*, 397.
- (95) Shannon, R. D. *Acta Cryst.* **1976**, *A32*, 751.
- (96) Norberg, N. S.; Gamelin, D. R. *J. Phys. Chem. B* **2005**, *109*, 20810.
- (97) Aasa, R.; Malmstrom, B. G.; Saltman, P.; Vanngard, T. *Biochim Biophys Acta* **1963**, *75*, 203.
- (98) Bou-Abdallah, F.; Chasteen, N. D. *J. Biol. Inorg. Chem.* **2008**, *13*, 15.
- (99) Aasa, R. *J. Chem. Phys.* **1970**, *52*, 3919.
- (100) Bryan, J. D.; Schwartz, D. A.; Gamelin, D. R. *J. Nanosci. Nanotech.* **2005**, *5*, 1472.
- (101) Dagtepe, P.; Chikan, V.; Jasinski, J.; Leppert, V. J. *J. Phys. Chem. C* **2007**, *111*, 14977.
- (102) Sibera, D.; Narkiewicz, U.; Guskos, N.; Zolnierkiewicz, G. *J Phys Conf Ser* **2009**, *146*, 012014.
- (103) Guskos, N.; Glenis, S.; Zolnierkiewicz, G.; Typek, J.; Berczynski, P.; Guskos, A.; Sibera, D.; Narkiewicz, U. *Appl. Phys. Lett.* **2012**, *100*, 122403.
- (104) Haase, M.; Weller, H.; Henglein, A. *J. Phys. Chem.* **1988**, *92*, 482.
- (105) Shim, M.; Guyot-Sionnest, P. *J. Am. Chem. Soc.* **2001**, *123*, 11651.
- (106) Germeau, A.; Roest, A. L.; Vanmaekelbergh, D.; Allan, G.; Delerue, C.; Meulenkamp, E. A. *Phys. Rev. Lett.* **2003**, *90*, 097401.
- (107) Schimpf, A. M.; Gunthardt, C. E.; Rinehart, J. D.; Mayer, J. M.; Gamelin, D. R. *J. Am. Chem. Soc.* **2013**, *135*, 16569.

- (108) Carroll, G. M.; Schimpf, A. M.; Tsui, E. Y.; Gamelin, D. R. *J. Am. Chem. Soc.* **2015**, *137*, 11163.
- (109) Valdez, C. N.; Schimpf, A. M.; Gamelin, D. R.; Mayer, J. M. *J. Am. Chem. Soc.* **2016**, *138*, 1377.
- (110) Liu, W. K.; Whitaker, K. M.; Kittilstved, K. R.; Gamelin, D. R. *J. Am. Chem. Soc.* **2006**, *128*, 3910.
- (111) Liu, W. K.; Whitaker, K. M.; Smith, A. L.; Kittilstved, K. R.; Robinson, B. H.; Gamelin, D. R. *Phys. Rev. Lett.* **2007**, *98*, 186804.
- (112) Cohn, A. W.; Kittilstved, K. R.; Gamelin, D. R. *J. Am. Chem. Soc.* **2012**, *134*, 7937.
- (113) Ochsenein, S. T.; Feng, Y.; Whitaker, K. M.; Badaeva, E.; Liu, W. K.; Li, X. S.; Gamelin, D. R. *Nat. Nanotechnol.* **2009**, *4*, 681.
- (114) Beaulac, R.; Schneider, L.; Archer, P. I.; Bacher, G.; Gamelin, D. R. *Science* **2009**, *325*, 973.
- (115) Buonsanti, R.; Llordes, A.; Aloni, S.; Helms, B. A.; Milliron, D. J. *Nano Lett.* **2011**, *11*, 4706.
- (116) Shanker, G. S.; Tandon, B.; Shibata, T.; Chattopadhyay, S.; Nag, A. *Chem. Mater.* **2015**, *27*, 892.
- (117) Dietl, T.; Ohno, H.; Matsukura, F.; Cibert, J.; Ferrand, D. *Science* **2000**, *287*, 1019.
- (118) Tribollet, J.; Behrends, J.; Lips, K. *EPL (Europhysics Letters)* **2008**, *84*, 20009.
- (119) Zhou, D. M.; Kittilstved, K. R. *J. Mater. Chem. C* **2015**, *3*, 4352.
- (120) Lehuta, K. A.; Kittilstved, K. R. *J. Mat. Chem. A* **2014**, *2*, 6138.
- (121) Ahn, G. Y.; Park, S.-I.; Shim, I.-B.; Kim, C. S. *J. Magn. Magn. Mater.* **2004**, *282*, 166.
- (122) Kittilstved, K. R.; Liu, W. K.; Gamelin, D. R. *Nat. Mater.* **2006**, *5*, 291.
- (123) Blinowski, J.; Kacman, P.; Dietl, T. *Mater. Res. Soc. Symp. Proc.* **2002**, *690*, 109.
- (124) Giuli, G.; Trapananti, A.; Mueller, F.; Bresser, D.; d'Acapito, F.; Passerini, S. *Inorg. Chem.* **2015**, *54*, 9393.
- (125) Samariya, A.; Singhal, R. K.; Kumar, S.; Xing, Y. T.; Alzamora, M.; Dolia, S. N.; Deshpande, U. P.; Shripathi, T.; Saitovitch, E. B. *Mater. Chem. Phys.* **2010**, *123*, 678.

- (126) Coey, J. M. D.; Wongsaprom, K.; Alaria, J.; Venkatesan, M. *J. Phys. D: Appl. Phys.* **2008**, *41*, 134012.
- (127) Pradhan, N.; Goorskey, D.; Thessing, J.; Peng, X. *Journal of the American Chemical Society* **2005**, *127*, 17586.
- (128) Radovanovic, P. V.; Gamelin, D. R. *Journal of the American Chemical Society* **2001**, *123*, 12207.
- (129) Wills, A. W.; Kang, M. S.; Wentz, K. M.; Hayes, S. E.; Sahu, A.; Gladfelter, W. L.; Norris, D. J. *J Mater Chem* **2012**, *22*, 6335.
- (130) Jana, N. R.; Chen, Y. F.; Peng, X. G. *Chemistry of Materials* **2004**, *16*, 3931.
- (131) Liang, X.; Ren, Y.; Bai, S.; Zhang, N.; Dai, X.; Wang, X.; He, H.; Jin, C.; Ye, Z.; Chen, Q.; Chen, L.; Wang, J.; Jin, Y. *Chemistry of Materials* **2014**, *26*, 5169.
- (132) Chen, Y. F.; Kim, M.; Lian, G.; Johnson, M. B.; Peng, X. G. *Journal of the American Chemical Society* **2005**, *127*, 13331.
- (133) Peng, Z. A.; Peng, X. G. *Journal of the American Chemical Society* **2001**, *123*, 1389.
- (134) Mehra, S.; Bergerud, A.; Milliron, D. J.; Chan, E. M.; Salleo, A. *Chemistry of Materials* **2016**, *28*, 3454.
- (135) Lounis, S. D.; Runnerstrom, E. L.; Llordes, A.; Milliron, D. J. *Journal of Physical Chemistry Letters* **2014**, *5*, 1564.
- (136) Lounis, S. D.; Runnerstrom, E. L.; Bergerud, A.; Nordlund, D.; Milliron, D. J. *Journal of the American Chemical Society* **2014**, *136*, 7110.
- (137) Buonsanti, R.; Llordes, A.; Aloni, S.; Helms, B. A.; Milliron, D. J. *Nano Lett* **2011**, *11*, 4706.
- (138) Della Gaspera, E.; Chesman, A. S.; van Embden, J.; Jasieniak, J. J. *ACS nano* **2014**, *8*, 9154.
- (139) Ito, D.; Yokoyama, S.; Zaikova, T.; Masuko, K.; Hutchison, J. E. *ACS nano* **2014**, *8*, 64.
- (140) Jansons, A. W.; Hutchison, J. E. *ACS nano* **2016**, *10*, 6942.
- (141) Bahsi, Z. B.; Aslan, M. H.; Ozer, M.; Oral, A. Y. *Cryst Res Technol* **2009**, *44*, 961.
- (142) Serier, H.; Gaudon, M.; Menetrier, M. *Solid State Sci* **2009**, *11*, 1192.

- (143) Park, H. W.; Chung, K. B.; Park, J. S.; Ji, S.; Song, K.; Lim, H.; Jang, M. H. *Ceram Int* **2015**, *41*, 1641.
- (144) Yadav, A. K.; Haque, S. M.; Tripathi, S.; Shukla, D.; Ahmed, M. A.; Phase, D. M.; Bandyopadhyay, S.; Jha, S. N.; Bhattacharyya, D. *Rsc Adv* **2016**, *6*, 74982.
- (145) Carroll, G. M.; Schimpf, A. M.; Tsui, E. Y.; Gamelin, D. R. *Journal of the American Chemical Society* **2015**, *137*, 11163.
- (146) Carroll, G. M.; Tsui, E. Y.; Brozek, C. K.; Gamelin, D. R. *Chemistry of Materials* **2016**, *28*, 7912.
- (147) Schimpf, A. M.; Knowles, K. E.; Carroll, G. M.; Gamelin, D. R. *Accounts of chemical research* **2015**, *48*, 1929.